Particle Formation, Growth and Transport on the Molecular and Submicron Scale

A DISSERTATION
SUBMITTED TO THE FACULTY OF
UNIVERSITY OF MINNESOTA
BY

Chenxi Li

IN PARTIAL FULFILLMENT OF THE REQUIREMENTS
FOR THE DEGREE OF
DOCTOR OF PHILOSOPHY

Professor Christopher J Hogan Jr.
Professor Peter H McMurry

November 2018

Acknowledgements

This thesis is the fruit of four years of graduate study at the University of Minnesota. I am deeply grateful to people who have contributed to this work, directly or indirectly. Though all of you cannot be recognized by name here, I thank all of you from my heart.

First, special recognition is due both my advisors, Dr. Chris Hogan and Dr. Peter McMurry. I am sincerely grateful that I am co-advised by two highly intelligent and caring professors who offered me guidance and gentle supervision. Their intellectual support and vision enabled me to gain confidence and mature as a researcher; their passion for work motivated me to pursue my scientific and creative interests; their feedback was most essential to the completion of all the work presented in this thesis. Without their support, this dissertation would not have been possible.

I have been fortunate to have worked with many other researchers during the course of my graduate study. In particular, I would like to thank Dr. Thomas Schwartzentruber, Narendra Singh, Dr. Bernard Olson and Dr. Dylan Millet. Their expertise on aerodynamic drag, impaction and mass spectrometry are reflected in the last two studies of this thesis. Additionally, I would like to thank Dr. Kenjiro Iida and Lauri Ahonen for our collaboration on tandem particle mobility-mass measurements.

I shall always cherish the rapport among my laboratory members and the mechanical engineering department. I thank my co-workers and friends Mark Stolzenburg, Siqin He, Seongho Jeon, Jikku Thomas, David Buckley, Xiaoshuang Chen, Huan Yang, Souvik Gosh, Jihyeon Lee and Yuechen Qiao for the knowledge we shared and the good times we had together.

Finally, I owe special thanks to my parents, Jimei Sun and Jianfang Li, and my girlfriend, Yue Yu. My parents’ faith in me is the foundation for everything that I have accomplished. Yue’s encouragement helped me survive the most difficult times; her emotional and intellectual support has been the most valuable thing to me throughout the past four years.

Abstract

Nanoparticle formation, growth and transport are important topics in several contexts, such as cloud formation, particle synthesis and additive manufacturing. This thesis approaches the subject with a broad perspective from molecular to the micro- scale, utilizing theoretical analysis, computational simulation as well as experiment observations.

First, general dynamic equations are non-dimensionalized and applied to simulate aerosol formation and growth in a constant rate reaction reactor. Dimensionless equations lead to results that are independent of condensing species formation rates. The effect of particle sink processes (e.g. evaporation, wall loss, loss to preexisting particles and dilution) and acid-base reactions are systematically investigated. Errors involved with common methods used for deducing particle growth rates from experimental observations are discussed. The results suggest the maximum overestimation error for true particle growth rates occurs when particle nucleation and growth are collision controlled.

Second, tandem mobility-mass spectrometry is utilized to understand sorption of organic vapors onto cluster ions. It is found that cluster structure, polarity and the molecular structure of the condensing vapors all influence uptake by cluster ions, qualitatively in agreement with previous activation efficiency measurements for condensational particle counters.

Third, nanoparticle transport in an aerosol deposition device is probed with fluid dynamics and particle trajectory simulations. To facilitate particle trajectory simulations, a neural network based drag law is developed that can be applied over a wide range of

Knudsen and Mach numbers. Simulation results reveal both particle impaction speeds and particle focusing effects are size dependent, with optimal particle sizes for maximizing particle impaction speed and focusing. With a newly developed framework, mass, momentum and kinetic energy fluxes from particles to the substrate are calculated. It is shown the kinetic energy flux can be above 10^4 W m^{-2} for modest aerosol concentrations due to particle focusing.

Finally, classification and prediction of different types of lung cell are performed with machine learning algorithms, using the volatile organic compound profiles of different cell populations. These profiles are obtained by a proton transfer reaction mass spectrometer with high resolution. Proper data processing procedures are found to be the key to differentiate cell populations with the measured profiles.

Table of Contents

List of Tables

List of Figures

Chapter 1: Introduction

Particle nucleation and growth in the gas phase play an important role in a variety of systems. In general, nucleation occurs via chemical reaction of gas phase precursors; this produces condensable species with low vapor pressure, which can be homogeneous or, more commonly, heterogeneous in chemical composition. Collisions between condensable species lead to gas-to-particle phase transition (nucleation) and subsequent collisions of condensable species with formed particles leads to particle growth (condensation). For example, in the atmosphere, oxidation of sulfur dioxide and volatile organic compounds produces condensable sulfuric acid and highly oxygenated organic molecules (Kirkby, 2011; Tröstl et al., 2016) that are partially responsible for new particle formation and particle growth in the atmosphere. These particles are a major source of pollution, affecting both climate (through their influence on cloud formation) (Seinfeld & Pandis, 2016) and human health. In hydrocarbon combustion, undesirable soot particles are produced by incomplete oxidation of the hydrocarbon fuel. Soot formation occurs by a very similar process, wherein hydrocarbons react to form condensable species, leading to soot nucleation and growth. Soot (black carbon) is a known carcinogen and with documented deleterious effects on human health (Haynes & Wagner, 1981; Shiraiwa, Selzle, & Pöschl, 2012) . Conversely, vapor phase organometallic precursors can be injected into combustion and high temperature reactors for the synthesis of functional particles, incorporated into catalysts, sensors, biomaterials and electroceramics (Strobel & Pratsinis, 2007). Hereto, the vapor phase precursors react to form condensable species. In all such systems, it is thus important to understand the interplay between the formation of condensable species, nucleation, and subsequent condensational particle growth, as well as with other dynamics affecting particle size distribution functions, namely deposition and coagulation.

This dissertation focuses on the dynamics of particles in the gas phase in a general manner and contains five sub-studies. The first two focus on the development and implementation of discrete-sectional models to better describe the interplay between condensable species formation, nucleation, condensation, coagulation, and particle deposition in experimental systems intended to mimic new particle formation in the atmosphere. The third is devoted the implementation of novel ion mobility-mass spectrometry based methods of probing condensation at the molecular scale, i.e. experimentally detecting vapor molecule binding to nanometer scale clusters. The fourth focuses on the development of new models to describe particle transport in variable Knudsen number, variable Mach number environments, and the application of such models in designing particle based coating process. Finally, the fifth focuses on the use of proton transfer reaction mass spectrometry to detect biologically derived volatile organic carbonaceous material (VOCs). Though each of these works is distinct in its motivation and each is written as a standalone manuscript, they are connected through their focus on the dynamics of particle and vapor laden gas phase systems. The remainder of this introductory chapter is devoted to a description of background material relevant to all chapters, including the modeling equations utilized in the first two studies, the instrumentation in the ion mobility-mass spectrometry focused work, a description of scenarios wherein aerosols are in variable Mach number, variable Knudsen number flows, and a brief overview on the detection of biologically derived VOCs.

The simplest particle nucleation and growth scenario occurs when there is "zero activation energy" (or ‘spinodal decomposition’). In this scenario, molecules/clusters of the condensing species merge into a new particle upon colliding and evaporation from particle surface is negligible compared to particle formation rates. This is the fastest route for particle nucleation (referred to as the ‘collision-controlled limit’ hereafter) and can be accurately modeled provided particle kinetics are correctly described. It has been reported that in multiple systems, e.g. particle formation in a chamber that contains a mixture of sulfuric acid and dimethylamine (Kürten et al., 2018), toluene vapor nucleation in a converging diverging nozzle (Chakrabarty, Ferreiro, Lippe, & Signorell, 2017), particle nucleation does approach the collision-controlled limit. However, a number of physical and chemical processes, e.g. evaporation from particle surface, particle deposition on reactor walls, system dilution, surface/volume chemical reactions, can cause the particle formation and growth processes to deviate significantly from the collision-controlled limit. The general dynamic equations (GDE) is a set of first order differential equations that integrate all these processes. For concentrations of particles with size d_p, the continuous form of the GDE can be written as:

$$\frac{dn(d_p,t)}{dt} = -\frac{\partial}{\partial d_p}\Big(I(d_p,t)n(d_p,t)\Big) + \frac{1}{2}\int_0^{d_p} \beta(d'_p, d_p - d'_p) n(d'_p,t) n(d_p - d'_p) dd_p - \\ \int_0^{\infty} \beta(d'_p, d_p) n(d'_p,t) n(d_p) dd_p - Sink(d_p,t)n(d_p,t) + Source(d_p,t)n(d_p,t) \quad (1.1)$$

where $n(d_p,t)$ is the concentration of particles with diameter d_p at time t, $I(d_p,t) = \frac{dd_p}{dt}$ is the particle growth rate due to net molecular uptake processes (condensation, evaporation, surface or volume chemical reactions). The two integral terms in Equation (1.1) represent particle formation and loss due to particle coagulation, respectively.

$Sink(d_p)$ is a generalized term that accounts for particle loss by wall deposition, dilution or deposition on preexisting aerosols; $Source(d_p)$ describes the production of particles with diameter d_p by other sources. By incorporating different physical/chemical processes into the GDE, the effect of these processes can be quantitatively evaluated. Moreover, the GDE can be transformed into dimensionless formulations (Peter H. McMurry, 1980) that give generalized solutions. To understand the effect of the particle sink processes and acid-base reaction on particle formation and growth, a discrete-section form of the GDE is non-dimensionalized in Chapter 2 for a system wherein a single condensing species is produced at a constant rate, R. The solutions obtained are only dependent on a set of dimensionless parameters that characterize the relative strength of sink processes/acid-base reaction and R.

Provided the physics and chemistry within the system are well understood (i.e. all rate coefficients are known), the GDE provides a bottom-up approach to predict particle formation and growth. In practice, however, the concentration of the condensing species, a key quantity in solving the GDE, is often unknown and can prove difficult to measure. In these circumstances, the concentration of condensing species must be determined indirectly from experimentally measurable quantities, i.e. particle growth rates. Multiple methods have been developed for this purpose (Markku Kulmala et al., 2012), e.g. the maximum concentration method, the log-normal distribution function method. One common feature shared by these methods is that a specific particle size is chosen to represent the experimentally measured particle size distribution (the local concentration maximum of the nucleation mode, for example); the particle growth rate is then calculated by following the evolution of this size as a function of time. Implicitly assumed in this approach is that molecular uptake of the nucleating species is the major contributor to the calculated growth rate, while the effects of coagulation and particle sink terms are not explicitly accounted for. As a result, the growth rate calculated in this manner may deviate from the true particle growth rate due to net molecular uptake processes, from which information regarding the condensing species can be extracted. In Chapter 3, this deviation is systematically examined and the limit of error is calculated for certain nucleation scenarios.

One special case of particle growth, which is of particular interest for particle detection, is particle growth in a condensational particle counter (CPC). In a CPC, particles are exposed to a supersaturated vapor (e.g. butanol, water). The vapor condenses heterogeneously on the particle surface and further condensation leads the particles to grow to an optically detectable size (M. R. Stolzenburg & McMurry, 1991). For particles with mobility diameters greater than 3 nm, the activation efficiency (defined as the fraction of grown particles to the total number of particles admitted into the growth tube in the CPC) of commercially available CPCs can reach ~100%. However, for sub-3 nm particles, it has been found that the CPC detection efficiency is highly dependent on particle size, polarity and composition (Iida, Stolzenburg, & McMurry, 2009; Chongai Kuang, Chen, McMurry, & Wang, 2012). Understanding the origin of these dependencies would provide insights into the heterogeneous nucleation process as well as assist novel CPC design.

Condensational growth of particles in a CPC starts with vapor sorption on the particle surface. At the University of Minnesota, it has been demonstrated that a differential mobility analyzer (DMA) coupled with a mass spectrometer (MS) is particularly useful to study this process (D. Oberreit et al., 2015; Thomas et al., 2016). An illustration of this setup is shown in Figure 1.1. Briefly, a DMA spatially separates particles of different electrical mobilities; as a result, only particles of a specific mobility exit the DMA and enter the MS at a given DMA voltage. To study vapor sorption, a condensing vapor is injected into the DMA, in which sorption of the vapor molecules onto the particle surface causes a shift of particle mobility. The shift in mobility is quantified by recording the change of applied voltage at which specific ions exit the DMA. By analyzing the mobility shift of the particles with the appropriate vapor sorption framework, the number of molecules adsorbed on the particle surface can be determined. Sodium chloride nanoparticles are one of the most commonly used materials for testing a CPC; therefore, in Chapter 4, organic vapor sorption by sodium chloride nanocluster ions is examined via a differential mobility analyzer-time of flight mass spectrometer system. A Langmuir type model is used to quantitatively describe the extent of vapor sorption.

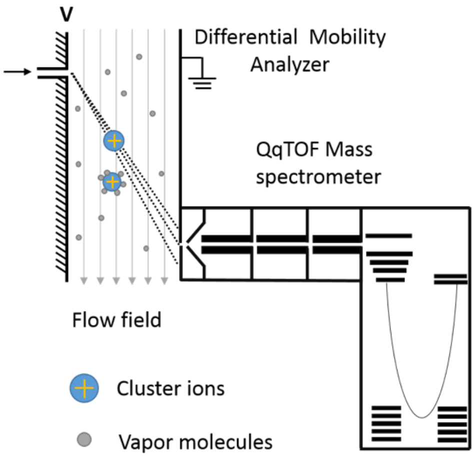

Figure 1.1. Schematic of the DMA-MS setup.

Nucleated particles, either formed in the liquid or gas phase, can be collected for manufacturing purposes. In Chapter 5, this dissertation discusses one method that has been increasingly adopted for surface coating and thin film production via impacting particles on a substrate, i.e. the aerosol deposition technique (AD) (Akedo, 2006; Jun & Maxim, 2002). In AD, micron or submicron scale particles are accelerated to exceed the speed of sound to impact on a substrate, facilitating formation of compact films. To achieve high particle impaction speed, converging-diverging nozzles are often utilized to generate a supersonic flow field. Figure 1.2 shows an illustrative schematic of an AD setup.

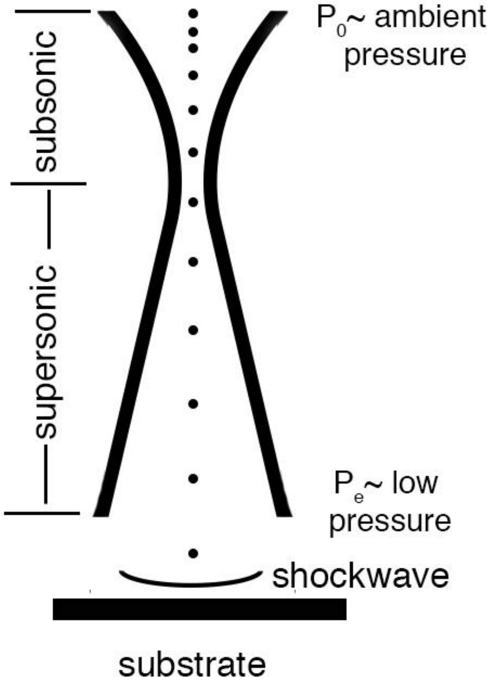

Figure 1.2. A simplified aerosol deposition (AD) setup. The upstream working pressure for AD is close to ambient pressure and the downstream pressure is typically several torr. A shockwave forms close to the substrate since the incoming flow to the substrate is supersonic.

The properties of the film produced by AD is closely related to the particle impaction speed (Hanft et al., 2015). However, as particles to be impacted are often in the submicron range travelling at supersonic speed, direct observation of particle velocity is difficult; consequently, particle impaction speed is often determined by simulation of the fluid flow profile and particle trajectories. Compared to traditional, subsonic particle impaction apparatus (Marple & Willeke, 1976), the supersonic nature of the flow exiting the nozzle leads to the formation of a shockwave close to the substrate, as illustrated in Figure 1.2. The structure of the shockwave affects particle trajectories; therefore, the setup of fluid dynamics simulations should allow resolution of shockwave structure.

In addition to accurate simulation of the flow profile, calculation of particle trajectories within the nozzle requires accurate description of the drag force exerted on the particles by the carrier gas. As the particles traverse through the nozzle and to the substrate, the particle Knudsen number, Kn_p (the ratio of local mean free path of the carrier gas molecules to the particle diameter), can vary by as much as 2 orders of magnitude. Also, due to insufficient acceleration of the particle and the abrupt change of carrier gas speed across the shockwave, the particle Mach number, Ma_p (based on relative velocity of the particle and the surrounding carrier gas), can exceed unity. The widely used drag coefficient for airborne particles, based on Stokes law and the Cunningham correction factor, can be used for to the whole range of Kn_p, but is only valid when particle Mach number is close to zero ($Ma_p \rightarrow 0$). Therefore, a drag law that works for a wide range of Knudsen and Mach numbers needs to be developed. In Chapter 5, flow profile simulation of an AD setup is discussed, along with the development of a neural network based drag law assisted by direct simulation of Monte Carlo. Particle trajectory simulation results and subsequent calculation of mass, momentum and heat transfer rates from particles to the substrate are also presented in Chapter 5.

In Chapter 6, a molecular perspective is taken to explore the possibility of disease diagnosis based on volatile organic compound (VOC) detection and quantification (referred as ‘VOC profiling’ hereafter), using techniques more commonly used in monitoring gas species concentrations in atmospheric systems. Biological samples, *in vitro* and *in vivo*, can emit a rich body of volatile organic compounds that serve as the samples’ biological signature. Therefore, in principle, the biological samples can be classified and sample types be predicted through VOC profiling. Due to the non-intrusive nature of VOC sampling processes, the potential of VOC profiling as a transformative diagnostic technique has long been recognized by researchers (Haick, Broza, Mochalski, Ruzsanyi, & Amann, 2014; Hakim et al., 2012). Common techniques of VOC profiling include gas chromatography-mass spectrometry (GC-MS) (Ligor et al., 2008; Wojciech et al., 2014), proton transfer reaction-mass spectrometry (PTR-MS) (Brunner et al., 2010; Tali et al., 2016) and a wide variety of nanosensors (Di Natale et al., 2003; Machado et al., 2005; G. Peng et al., 2010).

VOC profiling results need to be coupled with proper data processing techniques to enable robust, and even automated disease diagnosis. Machine learning algorithms are designed to learn from existing data and make predictions with incoming data. As a result, learning algorithms such as principle component analysis, discriminant analysis, decision trees are often utilized to analyze biological datasets. In Chapter 6, a PTR-MS is utilized to profile VOCs emitted by *in vitro* lung cancer cells as well as normal lung cells.

Selected machine learning algorithms are then applied to process the PTR-MS measurement data to classify and predict cell types.

In total, my dissertation mainly discusses particle formation, growth and transport on the molecular and nano- scales. As a summary of this introduction, my dissertation is structured as follows:

- Chapter 2 focuses on the effect of different particle sink processes and acid-base reactions on particle size distribution for a constant reaction rate system. A dimensionless framework is formulated and the GDE is numerically solved with a discrete sectional model.
- Chapter 3 discusses the errors associated with methods commonly employed for the calculation of particle growth rates using experimental data.
- Chapter 4 examines organic vapor sorption by sodium chloride cluster ions by a tandem differential mobility analyzer-mass spectrometer (DMA-MS) setup. Quantitative analysis is performed with a Langmuir type model to determine the extent of vapor uptake.
- Chapter 5 presents simulation results for an aerosol deposition process with a slit type converging diverging nozzle. A neural network based drag law that facilitates particle trajectory calculations is developed. Size and density dependent particle transport process is described. A framework that can be used for mass, momentum and heat transfer from the particles to the substrate is formulated.
- Chapter 6 discusses lung cancer cell classification and prediction facilitated by PTR-MS based VOC profiling and machine learning data analysis techniques.

Chapter 2: The Dynamic Behavior of Nucleating Aerosols in Constant Reaction Rate Systems: Dimensional Analysis and Generic Numerical Solutions

Abstract: Aerosol particles are formed by chemical transformations in diverse systems including the atmosphere, fossil fuel combustors, aerosol synthesis reactors, and semiconductor processing equipment. This study discusses solutions to the aerosol population balance equations that account for nucleation, coagulation, wall deposition, scavenging by preexisting particles, and dilution with particle-free air in spatially homogeneous systems when a condensing species is produced by gas phase reactions at a constant rate. Two nucleation mechanisms are considered: classical nucleation due to competing rates of condensation and evaporation, and chemical nucleation due to acid-base reactions. The equations, which apply to a single component system (two components, the acid and base, are included for acid-base nucleation), are cast in a dimensionless form. This leads to dimensionless parameters (dimensionless rate constants) that characterize the importance of each process. When these parameters are sufficiently small, the corresponding process (scavenging by pre-existing particles, wall deposition, dilution, and cluster evaporation) has an insignificant effect and nucleation approaches the collision-controlled limit. Because the dimensionless parameters vary inversely with the square root of the reaction rate, the collision-controlled limit is reached for any chemical system provided the reaction rate is high enough. The numerical solutions quantify the effects of each process for low rates of gas-to-particle conversion where

the dimensionless parameters become sufficiently large. They also illustrate how data for sub 10 nm number distributions can provide insights into the nucleation process.

2.1 Introduction

Certain gases react to produce nonvolatile particulate products. For example, in the atmosphere, sulfur dioxide (SO_2) reacts with hydroxyl to form sulfates, and complex reaction pathways involving many organic precursors can also lead to particle formation (Kirkby et al., 2016; Seinfeld & Pandis, 2016; Tröstl et al., 2016). Silane and other gases react to form contaminant particles in semiconductor processing equipment (Swihart & Girshick, 1999), and titanium tetrachloride is used to produce catalytic particles in flame synthesis reactors (Koirala, Pratsinis, & Baiker, 2016). In such systems, particles can nucleate from trace gas phase constituents formed by chemical reaction and can subsequently grow by condensation and coagulation. Other processes, such as loss to preexisting particles, deposition on reactor walls, entrainment of particle free air, cluster evaporation, etc. can also affect the number distributions of the nucleated aerosol. This study discusses solutions to the aerosol population balance equations pertinent to such processes.

There is a rich and growing body of work aimed at understanding the detailed chemical processes responsible for aerosol formation in reacting systems. This work shows that multiple species often contribute, and that particle mass can be formed by reactions that occur in the gas phase and on or within particles. Rather than attempting to describe the behavior of a particular system in all its complexity, the objective of this study is to obtain general solutions constrained by well-defined simplifying assumptions. In particular, we assume that only a single chemical species contributes to particle formation (two species, sulfuric acid and a basic gas, are considered for acid-base nucleation), and that this species is formed at a constant rate R [molecules $\mathrm{cm}^{-3}\ \mathrm{s}^{-1}$] . These may be good assumptions for aerosol formation in some chemical systems, such as the nucleation of sulfuric acid with a strong basic gas. For chemically more complex systems, such as atmospheric secondary organic aerosols, deviations between observations and our theoretical predictions may provide some insight into types of processes that are important.

This study builds on early work by Peter H. McMurry, beginning with McMurry (1980). That work focused on interpreting the pioneering measurements done by William Clark (W. E. Clark, 1972; W. E. Clark & Whitby, 1975), a doctoral student of the late Prof. Kenneth T. Whitby. Using the Whitby Aerosol Analyzer (WAA) (Whitby & Clark 1966), Clark measured time-dependent size distributions of 4 – 400 nm aerosol particles formed photochemically from SO_2 in a 17.7 m^3 Teflon film reactor. Although the air used in these experiments almost certainly contained unmeasured organic contaminants that contributed to aerosol formation, sulfates probably dominated since the concentrations of SO_2 were very high (49-2,880 ppb). It probably also contained significant concentrations of stabilizing compounds, such as ammonia or amines. McMurry's analysis assumed that a single chemical species was responsible for nucleation and particle growth. While McMurry (1980) accounted for all possible cluster and particle coagulation interactions, he assumed that evaporation rates were negligible relative to condensation rates (i.e., that nucleation was "collision-controlled").

Furthermore, he showed that if a single condensing species is formed at a constant rate R, the population balance equations can be cast in a nondimensional form that is independent of R. With these simplifications McMurry was able to predict observed number distributions and concentrations with to within about 50%. This "zero activation energy" approach (referred to as "spinodal decomposition" by the nucleation community) greatly simplifies nucleation modeling, since the primary uncertainties in nucleation theory involve modeling cluster stability (evaporation rates). Recent work from the CLOUD consortium involving the photooxidation of SO_2 in the presence of dimethyl amine (DMA) showed that "neutral clusters containing up to 14 SA [sulfuric acid] and 16 DMA molecules form at or close to the kinetic limit, limited only by the collision rate of SA molecules" (Kürten et al., 2014), confirming McMurry's 1980 hypothesis. Atmospheric observations also show that particle formation rates often vary in proportion to $[H_2SO_4]^2$ (C. Kuang, McMurry, McCormick, & Eisele, 2008; Weber et al., 1996), a result consistent with collision-controlled nucleation. Sihto (2006) and Riipinen (2007) found that particle formation rates vary as $[H_2SO_4]^p$ ($1<p<2$), which led to their conclusion that nucleation may either be limited by collisions of sulfuric acid with itself ($p=2$) or with an organic compound ($p=1$). Our analysis in this study does not address the latter possibility.

Rao and McMurry(1989) incorporated wall losses of sulfuric acid "monomer" and nanometer-sized particles in the nondimensional framework described above. Diffusion-limited wall deposition rates of these small particles were determined using the theory developed by Crump and Seinfeld (1981) and widely used by others including Kürten et al. (2014). They also accounted for cluster evaporation, assuming that evaporation rates could be predicted with the Kelvin equation (e.g., Friedlander (2000)). This allowed them to study the transition from collision-controlled to condensation/evaporation-controlled nucleation. In this study, our treatment of wall losses and classical condensation/evaporation-controlled nucleation is identical to that introduced by Rao and McMurry (1989), although our analysis is expanded to include other processes that might occur simultaneously. Independently, Lushnikov and Kulmala (1995) described a nondimensional solution for "source-enhanced" classical nucleation that accounted for the chemical production of condensing vapor. Their analysis was formulated to account for time-dependent vapor formation rates, so it follows that their analytical solutions are also applicable to constant rate systems. Their analysis also assumes constant condensation coefficients, which is not applicable to atmospheric nucleation, and does not account for cluster coagulation or other cluster removal processes.

Since about 1990, we and others have focused on developing new instruments for measuring clusters and particles in the 1 nm range together with their gas phase precursors (especially sulfuric acid vapor). These instruments have been used for atmospheric observations and laboratory experiments. This work has shown that acid-base nucleation is one process that contributes to nucleation in the atmosphere. Also, in some studies (e.g., CLOUD) experiments are done using constant volume reactors with sampled air continuously replenished with particle-free flow. This study incorporates these processes into the dimensionless framework from the 1980s and systematically compares the effects of each process on the dynamic behavior of the nucleated aerosols. This work complements the detailed understanding of cluster chemistry that has been the focus of much recent work, as it provides a means to confirm closure between predicted and observed number distributions of larger particles. It is those larger particles that determine the properties or effects of the nucleated aerosol.

2.2 Theory

We assume that a single condensing species is produced by gas phase chemical reactions at a constant rate R [molecules $\mathrm{cm^{-3}\ s^{-1}}$], and we consider two nucleation scenarios: (i) single component nucleation accounting for cluster evaporation using the classical liquid droplet model, and (ii) chemical nucleation by reactions of sulfuric acid vapor with a basic gas (e.g., ammonia or an amine). For both scenarios, species concentrations are assumed to be spatially uniform, all possible coagulation interactions are included, particles are assumed spherical, and time-dependent (rather than steady-state) solutions are obtained. We begin with the dimensional equations for both nucleation scenarios followed by their dimensionless analogs. The reader is referred to the nomenclature for definitions and some important relationships.

(i) Classical condensation-evaporation nucleation: the dimensional equations

Monomer (N_1):

$$\frac{dN_1}{dt} = \underbrace{R}_{\text{g} \rightarrow \text{p}} - \underbrace{N_1 \sum_{j=1}^{\infty} \beta_{1j} N_j}_{\text{coagulation}} - \underbrace{\frac{1}{4}\left(\frac{8k_bT}{\pi m_1}\right)^{1/2} A_{Fuchs} N_1}_{\substack{\text{loss to preexisting} \\ \text{particles}}} + \underbrace{\sum_{j=2}^{\infty} (1+\delta_{2j}) E_j N_j}_{\text{evaporation}} \tag{2.1}$$

$$- \underbrace{C_w (D_1)^{1/2} N_1}_{\text{wall losses}} - \underbrace{\frac{Q_{dil}}{V_{chamber}} N_1}_{\text{dilution}}$$

Clusters $(N_k, k > 2)$:

$$\frac{dN_k}{dt} = \underset{\text{coagulation}}{\frac{1}{2}\sum_{i+j=k}\beta_{ij}N_iN_j \quad - \quad N_k\sum_{j=1}^{\infty}\beta_{kj}N_j} \quad - \quad \underset{\text{loss to preexisting particles}}{\frac{1}{4}\left(\frac{8k_bT}{\pi k m_1}\right)^{1/2} A_{Fuchs}N_k} \qquad (2.2)$$

$$\underset{\text{evaporation}}{-E_kN_k \quad + \quad E_{k+1}N_{k+1}} \quad - \quad \underset{\text{wall losses}}{C_w\left(D_k\right)^{1/2}N_k} \quad - \quad \underset{\text{dilution}}{\frac{Q_{dil}}{V_{chamber}}N_k}$$

In Equation (2.2), k corresponds to the number of vapor molecules (monomer) in a cluster, and is used both as a subscript and a variable (third term on r.h.s.). This formulation implicitly assumes two populations of particles: those formed by nucleation, which are included in the coagulation terms, and those present initially (A_{Fuchs}). The coagulation terms in these equations are discussed in textbooks (e.g., (Friedlander, 2000; Seinfeld & Pandis, 2016). The evaporation rate constants, E_j , are derived using assumptions of the classical liquid droplet model, and are expressed in a discretized form that accounts for the evaporation of one molecule from a size j cluster to form a size j-1 cluster as well as the relative motion of the monomer and evaporating clusters (see nomenclature). In the limit of large j, $\frac{3}{2}\left(j^{2/3} - (j-1)^{2/3}\right) \rightarrow j^{-1/3}$ and the cluster size dependence in our expression for E_j (see nomenclature) collapses to the usual Kelvin equation expression. The Kelvin equation is derived assuming that the Gibbs free energy change for droplet formation is a continuous function of droplet radius, an approximation that becomes increasingly inaccurate as j decreased below 10. Our discrete formulation does nothing to ensure the validity of the underlying physical assumptions that lead to the liquid droplet model and has only a small effect on calculated results. The wall loss term is of the form used by Kürten et al. (2014). The relationship between this and earlier notation is shown in the footnote to Table 2.1. The empirical constant, C_w, is independent of particle size, but depends on the reactor dimensions and operating conditions (i.e., convection, temperature, etc.). The dilution term accounts for the entrainment of particle-free air, and assumes that mixing is instantaneous so that concentrations remain spatially uniform. The terms that describe loss to pre-existing particles account for transport to particles in the transition regime; the Fuchs surface area concentration, A_{Fuchs}, is assumed constant and is based on the approximate expression given by Fuchs and Sutugin (1971) and discussed by Davis et al. (1981). The relationship between A_{Fuchs} and the condensation sink (CS) used by (Kerminen & Kulmala, 2002) to describe cluster scavenging by pre-existing particles is (C. Kuang, Riipinen, Sihto, et al., 2010; P. H. McMurry et al., 2005):

$$CS = \left(\frac{8k_bT}{\pi m_1}\right)^{1/2} \frac{A_{Fuchs}}{4} \tag{2.3}$$

so these approaches are equivalent. This approach for scavenging by preexisting particles was first discussed by McMurry and Friedlander (P.H. McMurry & Friedlander, 1979); McMurry (1983) obtained accurate numerical solutions to quantify its effects. Rao and McMurry (1989) studied evaporation and wall losses using the mathematical framework discussed above.

(ii) Acid-base nucleation: the dimensional equations

The analysis uses the acid-base nucleation model proposed by Jen et al. (2014) (scheme 2 with $E_3 = 0$). This model involves simplifying assumptions about the multitude of acid-base reactions that contribute to cluster formation, as exemplified by the ACDC model proposed by McGrath et al. (2012), and is consistent with laboratory measurements reported by Jen and coworkers. The reader is referred to Jen's paper for details. The model for acid-base reactions does not explicitly account for temperature or for the role of water. Instead, the model assumes that dependencies on those variables would be reflected primarily in the monomer ($N_1 = AB$) evaporation rate constant (E_{AB}). Furthermore, this analysis assumes that the base concentration, [B], remains constant during nucleation. With these assumptions, Jen's scheme 2 leads to the following conservation equations for free acid, monomer, and clusters:

Free Acid (A)

$$\frac{d[A]}{dt} = \underset{\mathrm{g} \to \mathrm{p}}{R} - \underset{\substack{\text{reaction with}\\ \text{all clusters } (j \geq 1)}}{[A]\sum_{j=1}^{\infty}\beta_{Aj}N_j} - \underset{\substack{\text{loss to preexisting}\\ \text{particles}}}{\frac{1}{4}\left(\frac{8k_bT}{\pi m_A}\right)^{1/2} A_{Fuchs}[\mathrm{A}]} + \underset{\substack{\text{evaporation}\\ \text{of } N_1 = AB}}{E_{AB}N_1} \qquad (2.4)$$

$$- \underset{\text{reaction with B}}{k_{A+B}[A][B]} - \underset{\text{wall losses}}{C_w\left(D_A\right)^{1/2}[\mathrm{A}]} - \underset{\text{dilution}}{\frac{Q_{dil}}{V_{chamber}}[\mathrm{A}]}$$

Monomer ($N_1 = AB$)

$$\frac{dN_1}{dt} = \underset{\text{coagulation}}{-N_1\sum_{j=1}^{\infty}\beta_{1j}N_j} \quad - \quad \underset{\substack{\text{loss to preexisting}\\ \text{particles}}}{\frac{1}{4}\left(\frac{8k_bT}{\pi m_1}\right)^{1/2} A_{Fuchs}N_1} \quad + \quad \underset{\substack{\text{A + B reaction}\\ \text{forms } A\text{B} = N_1}}{k_{A+B}[\text{A}][\text{B}]} \tag{2.5}$$

$$- \underset{\substack{\text{reaction with A}\\ \text{forms N}_2}}{\beta_{1A}N_1[\text{A}]} \quad - \quad \underset{\substack{\text{AB evaporation}\\ \text{forms A + B}}}{E_{AB}N_1} \quad - \quad \underset{\text{wall losses}}{C_w\left(D_1\right)^{1/2}N_1} \quad - \quad \underset{\text{dilution}}{\frac{Q_{dil}}{V_{chamber}}N_1}$$

Clusters ($N_k, k > 2$)

$$\frac{dN_k}{dt} = \underset{\text{coagulation}}{\frac{1}{2}\sum_{i+j=k}\beta_{ij}N_iN_j \quad - \quad N_k\sum_{j=1}^{\infty}\beta_{kj}N_j} \quad - \quad \underset{\substack{\text{loss to preexisting}\\ \text{particles}}}{\frac{1}{4}\left(\frac{8k_bT}{\pi k m_1}\right)^{1/2} A_{Fuchs}N_k} \tag{2.6}$$

$$+\underset{\text{reactions with A}}{\left(\beta_{k-1A}N_{k-1} - \beta_{kA}N_k\right)[\text{A}]} \quad - \quad \underset{\text{wall losses}}{C_w\left(D_k\right)^{1/2}N_k} \quad - \quad \underset{\text{dilution}}{\frac{Q_{dil}}{V_{chamber}}N_k}$$

For a constant rate system (R=constant), the above conservation equations for both nucleation scenarios collapse to a dimensionless form that is independent of R and of the condensing species' properties (molecular volume, surface tension, mass, etc.) provided that the collision frequency function is a homogeneous function of those properties. Particles formed in chambers can easily grow into the transition regime, and the transition regime collision frequency function is not a homogeneous function of condensing species properties. However, the free molecular collision frequency function is homogeneous. Therefore, prior to nondimensionalizing the equations, β_{ij} is replaced with $\beta_{ij\,fm}$, thereby ensuring that solutions to the dimensionless equations are independent of species properties. One might guess that this would significantly limit the applicability of our results. However, as is shown in Figure 2.1, simulations performed using free molecular and transition regime collision frequency functions are nearly indistinguishable at t =0.5h and have only a minor difference at t = 2h. Two approaches were used for calculating transition-regime coagulation rates: the widely-used expression developed by Sutugin and Fuchs and described by Fuchs (1964), and the approach developed by Gopalakrishnan and Hogan (2011). Results obtained using the free molecular and transition regime collision frequency functions probably agree so well because most coagulation involves the smallest particles, which are present in much higher concentrations than particles in the transition regime. The results in Figure 2.1 were obtained assuming a monomer formation rate $R = 4 \times 10^6\ \mathrm{cm^{-3}s^{-1}}$ and a monomer volume of $1.62 \times 10^{-22}\ \mathrm{cm^3}$. This reaction rate is high enough to ensure that aerosol grows into the transition regime during the course of an hour or two; the monomer volume corresponds to a monomer containing one dimethylamine and one sulfuric acid molecule with an assumed density of $1.47\ \mathrm{g/cm^3}$ We conclude therefore, that for the chemical nucleation problems addressed in this study, sufficiently accurate results are obtained with the free molecular expression.

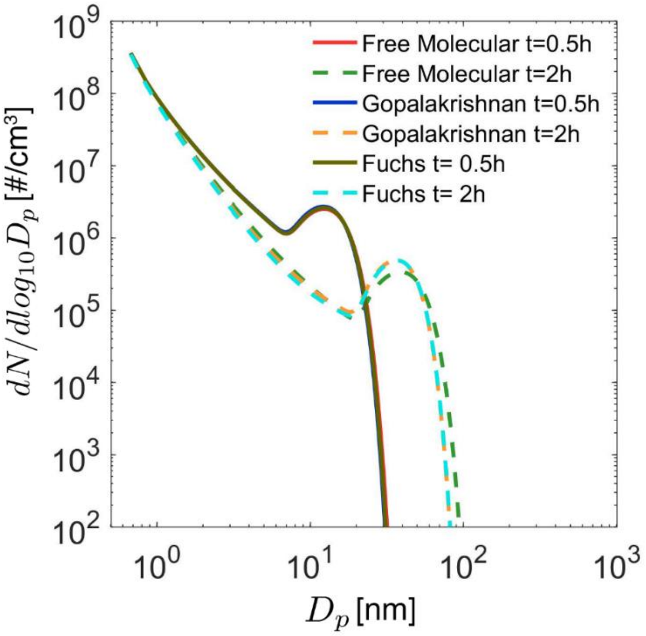

Figure 2.1. Transition regime vs free molecular regime solutions to the dimensional equations for collision-controlled nucleation ($\sqrt{L}$, E, W, and M all set equal to zero) with the initial condition $\widetilde{N}_j(\tau = 0) = 0$ for all j. Note that results obtained using the free molecular and transition regime collision frequency functions are nearly indistinguishable at 0.5h and differ by only a small degree at 2h.

The following expressions transform species concentrations, time, and collision frequency functions, to their dimensionless analogs:

$$N_j = \left(\frac{R}{\beta_{11\,fm}}\right)^{1/2} \widetilde{N}_j;\ [A] = \left(\frac{R}{\beta_{11\,fm}}\right)^{1/2} [\tilde{A}];\ [B] = \left(\frac{R}{\beta_{11\,fm}}\right)^{1/2} [\tilde{B}];$$

$$t = \frac{1}{(R\beta_{11\,fm})^{1/2}}\tau;\ \beta_{ij\,fm} = \beta_{11\,fm}c_{ij} \tag{2.7}$$

Furthermore, for free molecular transport, species diffusivities have the following dependence on mass:

$$\frac{D_i}{D_j} = \left(\frac{m_j}{m_i}\right)^{2/3} \tag{2.8}$$

With these transformations the above population balance equations assume the dimensionless forms given below. Values of the dimensionless parameters $\sqrt{L}\,, W, M$ and E & Ω or $\tilde{E}_{AB}$ & $\tilde{k}_A$ enable one to easily determine whether or not a given process (scavenging by preexisting particles, wall deposition, dilution, cluster evaporation) plays a significant role. (See Table 2.1 for the mathematical definitions of these parameters.) Transforming the dimensionless solutions back to dimensional form is done simply using Equations (2.7), which requires knowing the applicable value of R together with thermodynamic or condensing species material properties needed to calculate $\beta_{11\,fm}$.

(iii) Classical condensation-evaporation nucleation: the dimensionless equations

Monomer ($\tilde{N}_1$)

$$\frac{d\tilde{N}_1}{d\tau} = \underbrace{1}_{\text{g} \rightarrow \text{p}} - \underbrace{\tilde{N}_1 \sum_{j=1}^{\infty} c_{1j} \tilde{N}_j}_{\text{coagulation}} - \underbrace{(L)^{1/2}\,\tilde{N}_1}_{\substack{\text{loss to preexisting} \\ \text{particles}}} \tag{2.9}$$

$$+ \underbrace{E \sum_{j=2}^{\infty} (1+\delta_{2j})\, c_{1j} \exp\left\{\tfrac{3}{2}\Omega\left(j^{2/3}-(j-1)^{2/3}\right)\right\} \tilde{N}_j}_{\text{evaporation}} - \underbrace{W\tilde{N}_1}_{\text{wall losses}} - \underbrace{M\tilde{N}_1}_{\text{dilution}}$$

Table 2.1. Dimensionless Parameters

Parameter	Definition	Physical Significance
$\sqrt{L}$	$\dfrac{\frac{1}{4}\left(\frac{8k_bT}{\pi\rho v_1}\right)^{1/2} A_{Fuchs}}{\sqrt{R\beta_{11\,fm}}}$	$\dfrac{\text{Fractional Loss Rate of Monomers to Preexisting Particles}}{\sim\text{Net Monomer Formation Rate by Reaction and Self} - \text{Collisions}}$
W	$\dfrac{C_w(D_1)^{1/2}}{\sqrt{R\beta_{11\,fm}}}$	$\dfrac{\text{Fractional Loss Rate of Monomers to Walls}}{\sim\text{Net Monomer Formation Rate by Reaction and Self} - \text{Collisions}}$
E	$\dfrac{N_{sat}\beta_{11\,fm}}{\sqrt{R\beta_{11\,fm}}}$	$\dfrac{\text{Fractional Cluster Evaporation Rate}}{\sim\text{Net Monomer Formation Rate by Reaction and Self} - \text{Collisions}}$
Ω	$4\left(\dfrac{\pi}{6}\right)^{1/3}\dfrac{v_1^{2/3}\sigma}{k_bT} = \dfrac{\pi d_1^2\sigma}{\frac{3}{2}k_bt}$	$\dfrac{\text{Monomer Surface Energy}}{\text{Mean Thermal Energy}}$
$\tilde{E}_{AB}$	$\dfrac{k_{A+B}/K_{AB}}{\sqrt{R\beta_{11\,fm}}} = \dfrac{E_{AB}}{\sqrt{R\beta_{11\,fm}}}$	$\dfrac{\text{Monomer (AB) Evaporation Rate Constant}}{\sim\text{Net Monomer Formation Rate by Reaction and Self} - \text{Collisions}}$
$\tilde{k}_A$	$\left(\dfrac{k_{A+B}}{\beta_{11\,fm}}\right)[\tilde{B}] \cong [\tilde{B}]$	$\dfrac{\text{Monomer Formation Rate from }[\tilde{A}]}{\sim\text{Net Monomer Formation Rate by Reaction and Self} - \text{Collisions}}$
M	$\dfrac{Q_{dil}/V_{chamber}}{\sqrt{R\beta_{11\,fm}}} = \dfrac{k_{dil}}{\sqrt{R\beta_{11\,fm}}}$	$\dfrac{\text{Fractional Loss Rate of Monomers by Dilution}}{\sim\text{Net Monomer Formation Rate by Reaction and Self} - \text{Collisions}}$

‡ In terms of parameters used by (Crump & Seinfeld, 1981) and (P. H. McMurry & Rader, 1985),

$$W = \frac{2}{\pi}\cdot\frac{A_{chamber}}{V_{chamber}}\cdot\frac{\sqrt{k_eD_1}}{\sqrt{R\beta_{11\,fm}}} \Rightarrow C_w = \frac{2}{\pi}\cdot\frac{A_{chamber}}{V_{chamber}}\cdot\sqrt{k_e}$$

Clusters ($N_k, k > 2$)

$$\frac{d\tilde{N}_k}{d\tau} = \underbrace{\frac{1}{2}\sum_{i+j=k} c_{ij}\tilde{N}_i\tilde{N}_j \quad - \quad \tilde{N}_k\sum_{j=1}^{\infty} c_{kj}\tilde{N}_j}_{\text{coagulation}} \quad - \quad \underbrace{(L)^{1/2}\frac{1}{k^{1/2}}\tilde{N}_k}_{\substack{\text{loss to preexisting}\\ \text{particles}}} \tag{2.10}$$

$$\underbrace{-E\left\{c_{1k}\exp\left[\tfrac{3}{2}\Omega\left(k^{2/3}-(k-1)^{2/3}\right)\right]\tilde{N}_k - c_{1k+1}\exp\left[\tfrac{3}{2}\Omega\left((k+1)^{2/3}-k^{2/3}\right)\right]\tilde{N}_{k+1}\right\}}_{\text{Evaporation}}$$

$$- \quad \underbrace{W\frac{1}{k^{1/3}}\tilde{N}_k}_{\text{wall losses}} \quad - \quad \underbrace{M\tilde{N}_k}_{\text{dilution}}$$

(iv) Acid-base Nucleation: the dimensionless equations

Free acid ($\tilde{A}$)

$$\frac{d[\tilde{\mathrm{A}}]}{d\tau} = \underbrace{1}_{\mathrm{g}\rightarrow\mathrm{p}} \quad - \quad \underbrace{[\tilde{\mathrm{A}}]\sum_{j=1}^{\infty} c_{Aj}\tilde{N}_j}_{\substack{\text{reaction with}\\ \text{all clusters }(j\geq 1)}} \quad - \quad \underbrace{(L)^{1/2}\left(\frac{m_1}{m_A}\right)^{1/2}[\tilde{\mathrm{A}}]}_{\substack{\text{loss to preexisting}\\ \text{particles}}} \quad + \quad \underbrace{\tilde{E}_{AB}\tilde{N}_1}_{\substack{\text{evaporation}\\ \text{of } N_1 = AB}} \tag{2.11}$$

$$- \quad \underbrace{\tilde{k}_A[\tilde{\mathrm{A}}]}_{\text{reaction with B}} \quad - \quad \underbrace{W\left(\frac{m_1}{m_A}\right)^{1/3}[\tilde{\mathrm{A}}]}_{\text{wall losses}} \quad - \quad \underbrace{M[\tilde{\mathrm{A}}]}_{\text{dilution}}$$

Monomer ($\tilde{N}_1$)

$$\frac{d\tilde{N}_1}{d\tau} = \underbrace{-\tilde{N}_1 \sum_{j=1}^{\infty} c_{1j}\tilde{N}_j}_{\text{coagulation}} - \underbrace{L^{1/2}\tilde{N}_1}_{\text{loss to preexisting particles}} + \underbrace{\tilde{k}_A[\tilde{\mathrm{A}}]}_{\text{A + B reaction}} \tag{2.12}$$

$$- \underbrace{c_{1A}[\tilde{\mathrm{A}}]\tilde{N}_1}_{\text{reaction with A}} - \underbrace{\tilde{E}_{AB}\tilde{N}_1}_{\text{AB evaporation}} - \underbrace{W\tilde{N}_1}_{\text{wall losses}} - \underbrace{M\tilde{N}_1}_{\text{dilution}}$$

Clusters ($\tilde{N}_k, k > 2$)

$$\frac{d\tilde{N}_k}{d\tau} = \underbrace{\frac{1}{2}\sum_{i+j=k} c_{ij}\tilde{N}_i\tilde{N}_j - \tilde{N}_k \sum_{j=1}^{\infty} c_{kj}\tilde{N}_j}_{\text{coagulation}} - \underbrace{(L)^{1/2}\frac{1}{k^{1/2}}\tilde{N}_k}_{\text{loss to preexisting particles}} \tag{2.13}$$

$$+ \underbrace{\left(c_{k-1A}\tilde{N}_{k-1} - c_{kA}\tilde{N}_k\right)[\tilde{\mathrm{A}}]}_{\text{reactions with A}} - \underbrace{W\frac{1}{k^{1/3}}\tilde{N}_k}_{\text{wall losses}} - \underbrace{M\tilde{N}_k}_{\text{dilution}}$$

Note that for both classical and acid-base nucleation, the dimensionless parameters $\sqrt{L}, W, M, E$ and $\tilde{E}_{AB}$ determine the importance of processes that compete with coagulation. They can be interpreted as dimensionless first-order rate constants. In addition, classical nucleation depends on the dimensionless surface energy Ω. As is shown in Table 2.1, this term is mathematically equal to the "free energy of a monomer surface" divided by the mean translational energy ($\frac{3}{2}k_BT$). It is more physically valid to interpret Ω as the proportionality constant for the change in the normalized surface energy upon the evaporation of one molecule from a cluster. The dimensionless quasifirst-order rate constant for the A+B reaction, $\tilde{k}_A$, incorporates the constant concentration of the basic gas and is equal to $\tilde{k}_A = \left(k_{A+B}/\beta_{11\,fm}\right)[\tilde{B}]$. Because $k_{A+B} \cong \beta_{11\,fm}$, it follows that $\tilde{k}_A = [\tilde{B}]$. In the following discussion $\tilde{B}$ will be used in place of $\tilde{k}_A$ for simplicity. The dimensionless rate constants are all ratios of the corresponding dimensional rate constant to $\sqrt{R\beta_{11\,fm}}$, which also has dimensions of inverse time. The significance of $\sqrt{R\beta_{11\,fm}}$ can be understood by considering the equation for monomer formation and monomer-monomer collisions alone:

$$\frac{dN_1}{dt} = R - \beta_{11\,fm}N_1^2 \qquad (2.14)$$

which leads to:

$$\frac{N_1(t)}{N_1(\infty)} = \frac{1-\exp(-2t\sqrt{R\beta_{11\,fm}})}{1+\exp(-2t\sqrt{R\beta_{11\,fm}})} \qquad (2.15)$$

For a characteristic time equal to $1/\sqrt{R\beta_{11\,fm}}$, $\frac{N_1}{N_1(\infty)} = 0.76$. Thus, $\sqrt{R\beta_{11\,fm}}$ is a measure of the rate at which monomer would reach its steady state concentration if monomer concentrations were affected only by chemical formation and monomer-monomer collisions. A given process (scavenging by preexisting particles, wall deposition, dilution, or evaporation) will be insignificant when its effect on monomer concentrations significantly exceeds that due to monomer collisions alone. The numerical solutions discussed below confirm this expectation. As $\sqrt{L}$, W, and M approach unity, the corresponding process becomes significant. For the nucleation processes, monomer concentrations are affected by two parameters (E and Ω or $\tilde{E}_{AB}$ and $\tilde{k}_A \cong [\tilde{B}]$), both of which influence whether or not evaporation has a significant effect. Significantly, all of the dimensionless rate constants vary in proportion to $1/\sqrt{R}$. Thus, at a sufficiently high reaction rate, all of these processes become insignificant.

For classical nucleation, the solution to Equations (2.9-2.10) depends values of Ω and E, with larger values of Ω leading to a higher surface energy barrier for nucleation. Assuming the weight fraction of sulfuric acid in an aqueous droplet is the same as that in equilibrated aqueous solutions at the RH and temperature in Clark's chamber experiments, the surface tension of sulfuric acid aqueous droplets is estimated to be 0.075 $\mathrm{J\ m^{-2}}$, corresponding to an Ω value of 18.35. As an approximation, we choose to use $\Omega = 16$ for consistency with results discussed by Rao and McMurry (1989). Similarly, for acid-base nucleation the solutions to Equations (2.11-2.13) depend on both $\tilde{E}_{AB}$ and $[\tilde{B}]$.

2.3 Discussion of Numerical Solutions

The dimensionless population balance equations were solved numerically to compare the effects of the different cluster sink processes. Calculations were done by varying a single dimensionless parameter, assuming that other processes can be neglected. Thus, to study the impact of wall deposition, the dimensionless parameter, W, was varied from zero to a value much larger than unity, while the other dimensionless rate constants ($\sqrt{L}, M$ and E or $\tilde{E}_{AB}$), were set equal to zero. In an actual system, of course, more than one process could play a significant role, and the equations would need to be solved to account for their combined effects. The discrete-sectional algorithm applied in this study is similar to that described by Rao and McMurry (1989), though finer sections are utilized to improve simulation accuracy. In total, 100 discrete sizes and

250 sections are used, with a geometric volume amplification factor of 1.0718 for neighboring sections.

2.3.1 *Effect of Different Sink Processes on Distribution*

First we examine the influence of each of the processes on particle number distribution, using the collision-controlled limit as a baseline. Figure 2.2 displays the sensitivity of dimensionless number distributions to W, $\sqrt{L}$, M, E and $\tilde{E}_{AB}$ at $\tau = 100$. To allow concentrations of discrete sizes and distribution functions to be shown on the same plot, discrete concentrations were converted to distribution functions using the following transformation:

$$\left.\frac{d\tilde{N}}{d log_{10}\tilde{D}_p}\right|_{\text{discrete size } i} = \frac{\tilde{N}}{log_{10}\left(i+\frac{1}{2}\right)^{1/3} - log_{10}\left(i-\frac{1}{2}\right)^{1/3}} \tag{2.16}$$

The minimum size plotted ($\tilde{D}_p$ =1.24)) corresponds to the monomer. Wall deposition (W), scavenging by pre-existing particles ($\sqrt{L}$) and dilution (M) (Figures 2.2a-2.2c) have qualitatively similar effects on the distribution: as the rate constants increase, particle concentrations decrease for all particle sizes with the second peak in the distribution eliminated. However, for the same value of a rate constant (i.e., dimensionless parameter), dilution has a bigger effect than scavenging by preexisting particles or wall deposition since the impacts of the latter processes decrease with increasing particle size, while dilution affects all sizes equally. The influence of evaporation (Figures 2.2d-2.2f) is different in that total particle volume concentrations are redistributed rather than lost. For both nucleation scenarios, concentrations of $1 < \tilde{D}_p < 10$ particles decrease sharply as the evaporation rate constants increase.

Solutions for two base concentrations ($\tilde{B} = 0.1 \text{ and } 10$) are shown in Figure 2.2e and Figure 2.2f, respectively. $\tilde{B} = 0.1$ corresponds, for example, to $R = 7 \times 10^4$ molecules cm^{-3} s^{-1} and a base concentration of 0.05 pptv. This value of R would occur if 1 ppb SO_2 were oxidized at a rate of 1 % hr-1, a characteristic midday value for the continental atmosphere. While there remains uncertainty about concentrations of basic gases such as amines, mixing ratios would likely exceed 0.05 pptv in the terrestrial boundary layer but might be below this in other regions of the atmosphere. Figure 2.3e shows that for $\tilde{B} = 0.1$, the distribution does not converge to the collision-controlled limit even if the A + B reaction is collision-controlled (i.e, $\tilde{E}_{AB} = 0$). This is because the amount of available base is insufficient to react with all of the chemically-produced acid to form monomers (AB). For $\tilde{B} = 10$, however, the base is high enough to ensure that nucleation reaches the collision-controlled limit when $\tilde{E}_{AB} = 0$. Acid-base nucleation leads to less pronounced valleys than those presented in Figure 2.2d since only monomers evaporate in this model while all particles undergo evaporation in the classical nucleation model.

Figure 2.2 also illustrates how measurements of sub 10 nm number distributions (corresponds to a dimensionless diameter of about 18 when $v_1 = 1.7 \times 10^{-22}\ cm^{-3}$) could provide insights into processes that occur during nucleation. For both classical and acid-base nucleation, the number distributions of the smallest particles are significantly suppressed relative to distributions that would occur if clusters do not evaporate. Information on sub 10 nm number distributions would also allow one to distinguish between these nucleation processes. While significant progress on such measurements has been made over the past decade, measurement uncertainties need to be reduced to allow such measurements to reach their full potential.

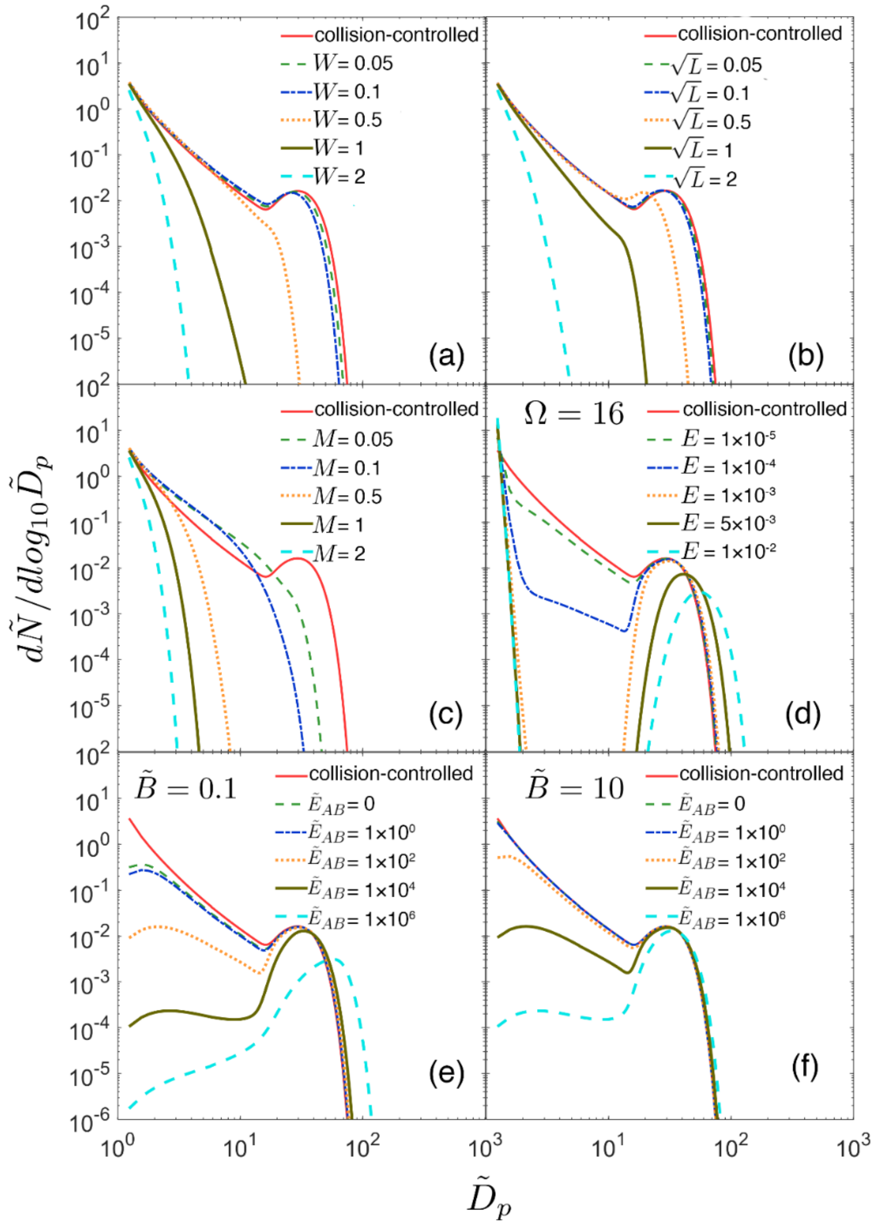

Figure 2.2. Effects of W, $\sqrt{L}$, M, E and $\tilde{E}_{AB}$ on dimensionless number distributions at $t = 100$. Note that results approach the collision-controlled limit for the smallest values of W, $\sqrt{L}$, M, E and $\tilde{E}_{AB}$ except when $\tilde{B}$ = 0.1.

2.3.2 Particles Larger Than Cut-off Sizes

Aerosol instruments such as CPCs often have cut-off sizes below which detection efficiencies drop sharply. Therefore, it is sometimes useful to compare the predicted and observed number concentrations of particles greater than a specified size, k. Figure 2.3a shows the impact of $W, E,$ or $\tilde{E}_{AB}$ on the time-dependent number concentration of particles larger than k=10 and 3000. For a monomer volume of $1.7 \times 10^{-22}\mathrm{cm}^3$, these correspond to diameters of 1.5 and 10 nm, respectively. $\widetilde{N}_{k\,tot}(\tau)$is defined by:

$$\widetilde{N}_{k\,tot}(\tau) = \sum_{n=k}^{\infty} \widetilde{N}_n(\tau) \tag{2.17}$$

In each case, one rate constant ($W, E,$ or $\tilde{E}_{AB}$) is varied to show its effect on $\widetilde{N}_{k\,tot}(\tau)$ with the other rate constants all set to zero. The effects of $\sqrt{L}$ and M are not shown here as they are qualitatively similar to that of W. In each case, $\widetilde{N}_{k\,tot}$ increases from zero to a maximum value, $\widetilde{N}_{max\,k}$, before decreasing due to coagulation and other removal processes. The maxima are indicated by circles (k=10) and triangles (k=3000). Note that wall deposition leads to $\widetilde{N}_{3000\,tot}(\tau) \ll \widetilde{N}_{10\,tot}(\tau)$, while significantly smaller decreases in $\widetilde{N}_{3000\,tot}(\tau)$ are observed for both nucleation scenarios. This is because wall deposition causes a significant fraction of nucleated particles to be lost before they reach size 3000, while in the absence of wall deposition particles tend to survive once they pass size 10 for both nucleation scenarios.

Figure 2.3b displays $\widetilde{N}_{max\,k}$ as a function of the rate constants (W, E, and $\tilde{E}_{AB}$) for six values of k ranging from 10 to 3000. Again, there's an obvious distinction between wall deposition and both nucleation scenarios. For wall deposition, lines for different k values do not converge as W increases, while values converge towards a single asymptotic limit as E (classical) and $\tilde{E}_{AB}$ (acid-base) increase. These asymptotic limits occur because (i) fewer particles are formed as the evaporation parameters increase, decreasing the effects of coagulation, and (ii) particles that do form tend to survive. $\tilde{N}_{k\,tot}(\tau)$ drops rapidly with W and E, but less rapidly with $\tilde{E}_{AB}$. The more gradual decrease with $\tilde{E}_{AB}$ is due, in part, to the constant base concentration assumed in the model and the stability of clusters larger than monomer. The model implies that classical nucleation tends to produce particles in a single burst, while nucleation resulting from chemical processes (such as acid-base reactions) tends to be more sustained.

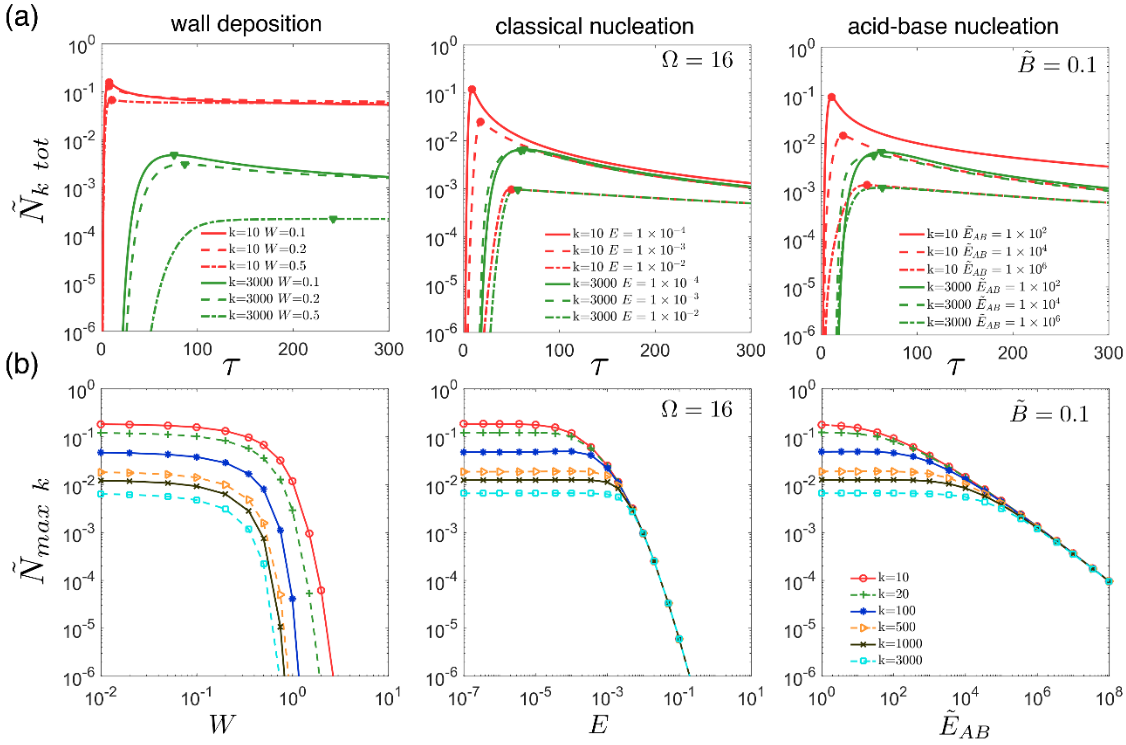

Figure 2.3. (a) Effects of W, E and $\tilde{E}_{AB}$ on and time-dependent total concentrations $\tilde{N}_{k\,tot}(\tau)$ for k =10 and 3000, and (b) $\tilde{N}_{max\,k}$ versus W, E and $\tilde{E}_{AB}$ for several values of k. Results for $\sqrt{L}$ and M are qualitatively similar to those for W and are therefore not included.

2.3.3 Evolution of Particle Size Distribution

Contour plots can be utilized to conveniently visualize the development of particle distributions for the entire time span of simulation. Figure 2.4 displays contour plots of time-dependent number distributions for the collision-controlled limit and for selected values of $W,\ \sqrt{L},\ M, E$ & Ω and $\tilde{E}_{AB}$ & B. The particle number distributions are represented by a logarithmic color scale with red representing the highest concentration and blue the lowest. Due to the wide range of particle concentration, dimensionless concentrations lower than 1×10^{-10} are artificially set to 1×10^{-10}. Values of the rate constants are chosen such that $\widetilde{N}_{max\,100}$ would be half of its value reached in the collision-controlled limit. The horizontal line at $\widetilde{D}_p = 5.76$ corresponding to k=100 is shown for reference.

The contour plots for W and $\sqrt{\mathrm{L}}$ are similar to that of the collision-controlled limit although particle concentrations are somewhat lower for all sizes and the average particle size is somewhat smaller. In contrast, dilution (M) leads to distributions that reach a steady state at approximately $\tau = 80$. W, $\sqrt{L}$ and M all lead to permanent removal of particulate mass from the nucleated aerosol, but with different size dependencies. Losses by wall deposition and scavenging by preexisting particles decrease with increasing size W and $\sqrt{L}$, while M affects all particle sizes equally and at steady state newly generated particle volume compensates for sampling losses.

For both nucleation scenarios, new particles are formed in the early stage of the simulation. These particles serve as condensation sinks and continue to grow and become more polydisperse as time progresses. Such widening of the distribution for these particles is due partly to coagulation and partly to numerical diffusion, as discussed by Warren and Seinfeld (1985).

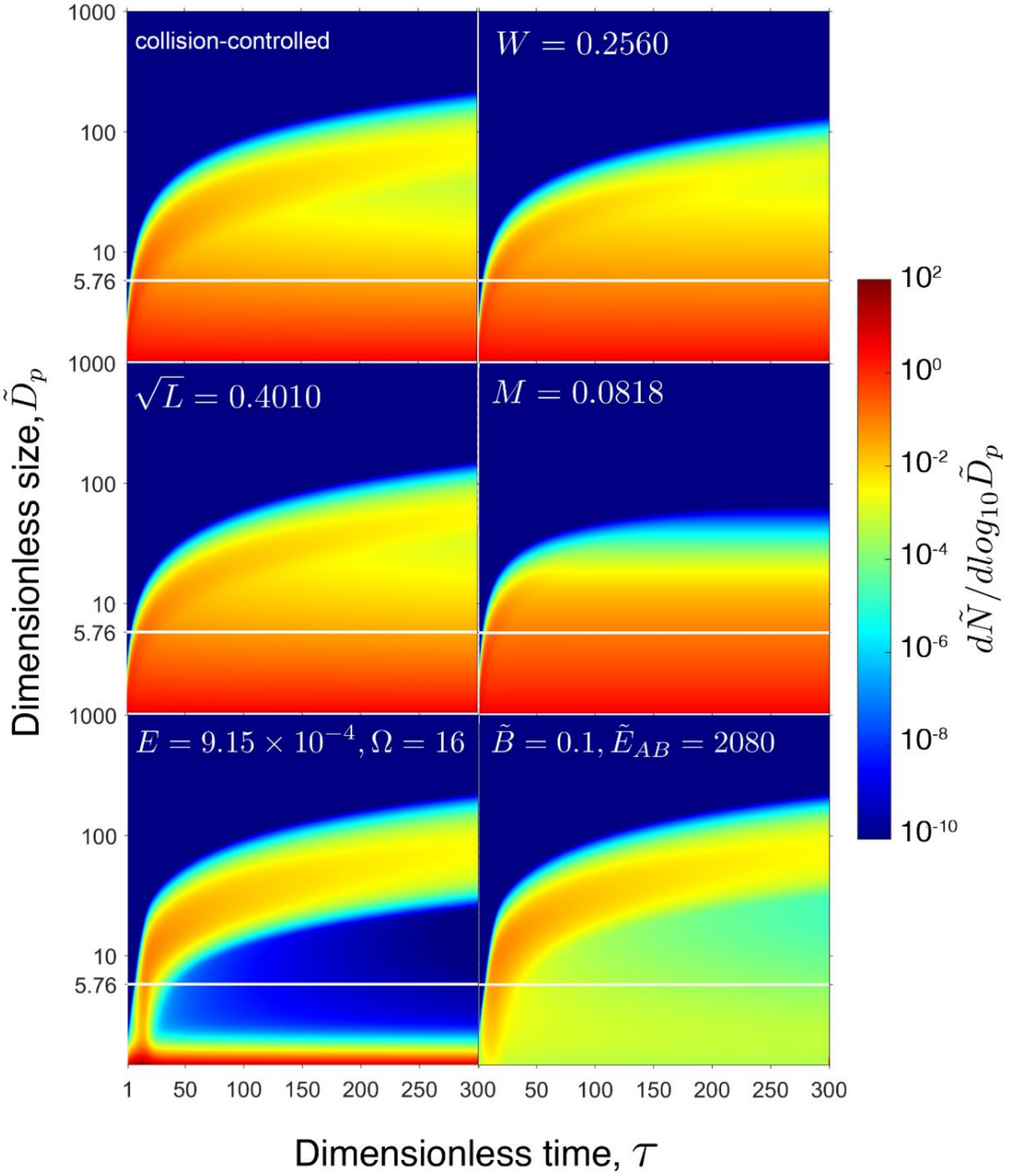

Figure 2.4. Contour plots showing the effects of $W, \sqrt{L}, M, E$ and $\tilde{E}_{AB}$ on time-dependent size distributions. Values of the rate constants are chosen so that $\tilde{N}_{\max 100}$ is half of its value in the collision-controlled limit. The dimensionless particle concentration is indicated by a logarithmic color scale.

2.4 Conclusions

We used a discrete-sectional model to simulate the dynamic behavior of aerosols in chemically reacting systems. The population balance equations were cast in a nondimensional form that reveals the dimensionless parameters that quantify the effects of various sink processes. Based on our simulations, we draw the following conclusions:

1. The use of the free molecular collision frequency function, rather than the transition regime expression, is justified for simulations described in this study. This is because most coagulation occurs among the smallest particles.
2. For every sink process except acid-base nucleation, the collision-controlled limit is reached provided the corresponding dimensionless rate constant approaches zero. For acid-base nucleation, the collision-controlled limit is reached only when the base concentration is sufficiently high.
3. Different sink processes target particles of different sizes. Specifically, dilution has the same effect on all particle sizes. Evaporation, either in the classical nucleation model or acid-base nucleation model, preferentially affects the smallest sizes. Wall deposition and loss to preexisting particles affect particles of all sizes, although at rates that decrease with increasing size. These size-dependencies impact the time dependent size distributions that would be observed in a chamber experiment or the atmosphere.
4. Dimensionless rate constants embody the dependence of sink processes on material properties and experimental conditions, and are straightforward to calculate. Care must be taken to avoid errors due to dilution or wall deposition when calculating monomer formation rates, R.

Our analysis leads to dimensionless parameters (Table 2.1) that determine whether or not a given process significantly affects size distributions of nucleated particles. When the parameters are sufficiently large, effects become significant. We have formulated the theory to include all of the processes that were considered, but for simplicity we have shown numerical results that consider the effects of only an individual process. In practice, multiple processes are likely to occur simultaneously, and in that case the equations must be solved to account for their simultaneous effects. For example, wall deposition and dilution always occur in chamber experiments reported by CLOUD, and cluster evaporation occurs for some chemical systems. Collectively, these processes will have a greater effect than any individual process, so deviations from the collision-controlled limit will occur at smaller values of the dimensionless parameters than are reported here for individual processes.

2.5 Nomenclature

Roman:

A_{Fuchs}	aerosol surface area concentration, corrected to account for transition regime condensation $= \int_{d_{p\,min}}^{\infty} \frac{\frac{4}{3}(Kn+Kn^2)}{1+1.71Kn+\frac{4}{3}Kn^2} \pi d_p^2 n\left(d_p\right) dd_p$ where $d_{p\,min}$ is the smallest size of pre-existing particles
$[A]$	concentration of free acid
$[\tilde{A}]$	dimensionless concentration of free acid
$[B]$	concentration of free base
$[\tilde{B}]$	dimensionless concentration of free base
β_{ij}	collision frequency function for clusters that contain *i* and *j* monomer
$\beta_{ij\,fm}$	free molecular expression for *i*-*j* collisions $= \left(\frac{3}{4\pi}\right)^{1/6} \left(\frac{6k_bT}{\rho}\right)^{1/2} v_1^{1/6} \left(\frac{1}{i}+\frac{1}{j}\right)^{1/2} \left(i^{1/3}+j^{1/3}\right)^2$
c_{ij}	dimensionless free molecular collision function for *i*-*j* clusters $= \frac{\beta_{ij\,fm}}{\beta_{11\,fm}} = \frac{1}{4(2)^{1/2}} \left(\frac{1}{i}+\frac{1}{j}\right)^{1/2} \left(i^{1/3}+j^{1/3}\right)^2$
c_{iA}	$= \frac{\beta_{iA\,fm}}{\beta_{11\,fm}} = \frac{1}{4(2)^{1/2}} \left(\frac{1}{i}+\frac{v_1}{m_A/\rho_A}\right)^{1/2} \left(i^{1/3}+\left(\frac{m_A/\rho_A}{v_1}\right)^{1/3}\right)^2$
C_w	Chamber wall loss constant as defined by Kürten et al. (2014)
d_p	particle diameter
$\tilde{d}_p$	dimensionless particle diameter $= d_p/v_1^{1/3} = (6k/\pi)^{1/3} = (6v/(\pi v_1))^{1/3}$

D_s	diffusion coefficient for species s
E_j	Monomer evaporation rate constant from size *j* clusters $= \beta_{11\,fm} N_{sat} \exp\left[\frac{3}{2}\Omega\left(j^{2/3} - (j-1)^{2/3}\right)\right]$
k_{A+B}	forward rate constant for the reaction A+B→AB, assumed equal to the A + B collision rate
E_{AB}	evaporation rate constant for the reaction AB→A+B
K_{AB}	equilibrium constant for A+B⇔AB, $= \frac{k_{A+B}}{E_{AB}}$
k_b	Boltzmann's constant
Kn	Knudsen Number , $= 2\lambda/d_p$
m_s	mass of species s
$n(d_p)$	number distribution function of preexisting aerosol $= \frac{dN}{dd_p}$, where *N* is total number concentration
N_j	concentration of clusters that contain *j* monomer
$\widetilde{N}_j$	dimensionless concentration of clusters that contain j monomer
N_{sat}	saturation vapor concentration of condensing monomer
R	rate of monomer formation by gas phase reaction
Q_{dil}	volumetric flow rate of particle free air entering a rigid reactor
t	time
T	absolute temperature
v_1	monomer volume $= m_1/\rho$
$V_{chamber}$	volume of rigid chamber

Greek:

δ_{2j}	Kronecker delta function (=1 for j=2, and =0 for $j\neq$2)
λ	mean free path
ρ	particle density
σ	surface tension
τ	dimensionless time

Chapter 3: Errors in Nanoparticle Growth Rates Inferred from Measurements in Chemically Reacting Aerosol Systems

Abstract: In systems where aerosols are being formed by chemical transformations, individual particles grow due to the addition of molecular species. Efforts to improve our understanding of particle growth often focus on attempts to reconcile observed growth rates with values calculated from models. However, because it is typically not possible to measure the growth rates of individual particles in chemically reacting systems, they must be inferred from measurements of aerosol properties such as size distributions, particle number concentrations, etc. This work discusses errors in growth rates obtained using methods that are commonly employed for analyzing atmospheric data. We analyze "data" obtained by simulating the formation of aerosols in a system where a single chemical species is formed at a constant rate, R. We show that the maximum overestimation error in measured growth rates occurs for collision-controlled nucleation in a single-component system in the absence of a pre-existing aerosol, wall losses, evaporation or dilution, as this leads to the highest concentrations of nucleated particles. Those high concentrations lead to high coagulation rates that cause the nucleation mode to grow faster than would be caused by vapor condensation alone. We also show that preexisting particles, when coupled with evaporation, can significantly decrease the concentration of nucleated particles. This can lead to decreased discrepancies between measured growth rate and true growth rate by reducing coagulation between nucleated particles. However, as particle sink processes get stronger,

measured growth rates can potentially be lower than true particle growth rates. We briefly discuss nucleation scenarios where the observed growth rate approaches zero while the true growth rate does not.

3.1 Introduction

Aerosol systems undergo transformations by processes that include coagulation, convection, deposition on surfaces, source emissions, nucleation, growth, etc. The aerosol general dynamic equation (GDE) (Friedlander, 2000; Gelbard & Seinfeld, 1979, 1980) describes the time rate of change of size-dependent particle concentration and composition by such processes. Recent work has focused on understanding processes that affect growth rates of freshly nucleated atmospheric nanoparticles (Hodshire et al., 2016; Kontkanen et al., 2016; Ilona Riipinen et al., 2012; J. Smith et al., 2008; J. N. Smith et al., 2010; Tröstl et al., 2016).This is important because a particle's survival probability increases with growth rates (Kerminen & Kulmala, 2002; C. Kuang, Riipinen, Yli-Juuti, et al., 2010; P.H. McMurry & Friedlander, 1979; Weber et al., 1997). Nucleated particles are more likely to form cloud condensation nuclei and affect climate when survival probabilities are high.

Following established conventions long used in modeling aerosol dynamics (Friedlander, 2000; Gelbard & Seinfeld, 1979, 1980), we define the particle "growth rate" as the net rate of change in diameter of individual particles due to the addition or removal of molecular species. (If evaporation exceeds addition, the growth rate would be negative.) While most work to date has focused on condensation and evaporation, chemical processes such as acid-base reactions, organic salt formation, liquid phase reactions, and the accretion of two or more organic molecules to form a larger compound having lower volatility may also contribute to growth (Barsanti, McMurry, & Smith, 2009; Lehtipalo 2014; P. H. McMurry & Wilson, 1982; Ilona Riipinen et al., 2012). In a chemically reacting system, the total diameter growth rate, GR, is given by the sum of all such processes:

$$\frac{dd_p}{dt} = GR = GR_{\frac{condensation}{evaporation}} + GR_{acid-base\ reactions} + GR_{accretion} + GR_{other} \tag{3.1}$$

The effect of growth on the aerosol distribution function is given by (Heisler & Friedlander, 1977):

$$\left.\frac{\partial n}{\partial t}\right|_{Growth} = -\frac{\partial}{\partial d_p}\left[n\left(d_p, t\right)\frac{dd_p}{dt}\right] \tag{3.2}$$

where the aerosol number distribution, $n(d_p, t)$ is defined such that the number concentration of particles between d_p and $d_p + dd_p$ is equal to $n(d_p, t)dd_p$. Coagulation, including the coagulation of a molecular cluster with a larger particle, can also lead to particle growth. It is worthwhile, however, to treat coagulation and growth separately. The extent to which the coagulation of freshly nucleated molecular clusters contributes to measured growth rates can be accurately determined only if the entire number distribution down to clusters of size 2 is accurately measured. In the absence of such data, the contributions of cluster coagulation to growth could erroneously be attributed to vapor uptake. Coagulation is accounted for with the coagulation integrals in the GDE and is a relatively well understood process that can be described with reasonable confidence in models (Chan & Mozurkewich, 2001; Kürten et al., 2018). Growth involves processes that are not well understood for chemically complex aerosol systems, such as the atmosphere (Barsanti et al., 2009; Hodshire et al., 2016; Ilona Riipinen et al., 2012).

Progress towards understanding growth can be achieved through efforts to reconcile GRs that are observed experimentally with values predicted by models. Such work requires that size- and time-dependent GRs be accurately determined from observations. The literature includes many reports of observed GRs (Riccobono, 2012; Mark R. Stolzenburg et al., 2005; Tröstl et al., 2016; J. Wang, McGraw, & Kuang, 2013), but uncertainties in reported values are typically not well understood. Because it is usually not possible to measure the growth of individual particles as they undergo chemical transformations, GRs are calculated indirectly using time-dependent observations of aerosol properties such as number distributions or number concentrations larger than a given size. Those properties are typically affected by many processes, some poorly understood, that can affect reported GRs to an unknown extent.

A variety of approaches have been used to extract GRs from observations. We refer to these values as GR_m, where the subscript 'm' designates 'measured'. Methods that we discuss include:

1. Maximum Concentration Method (Markku Kulmala et al., 2012). During a nucleation event, particle concentrations in a given size bin increase from their initial values, passing through a peak before they eventually decrease. This technique involves noting the times that this maximum occurred in different size bins. The growth rate is obtained by first fitting a linear function of particle diameter (corresponding to the size bins) vs. time, and then calculating the slope of the fitted function.

2. Appearance Time Method (Lehtipalo 2014). This approach has been used to analyze data from condensation particle counter (CPC) batteries (Riccobono, 2014), particle size magnifier (PSM) (Lehtipalo 2014), etc.. In brief, GR_m is determined by the differences in concentration rise times (typically, either 5% or 50% of the maximum) measured by the instruments with differing minimum detection sizes. A variation of this approach was reported by Weber et al. (1997), who estimated growth rates from the observed time delay in measurements of sulfuric acid vapor and particles measured with a condensation particle counter having a minimum detectable size of about 3 nm.

3. Log-normal Distribution Function Method (Markku Kulmala et al., 2012). Lognormal distributions are fit to the growing mode of nucleated particles. GR_m is defined as the growth rate of the geometric mean size of these distributions.

While these methods do not account for the effects of coagulation on measured changes in particle size, the literature includes approaches that explicitly account for such effects (C. Kuang et al., 2012; Lehtinen, Rannik, Petaja, Kulmala, & Hari, 2004; Pichelstorfer et al., 2017; Verheggen & Mozurkewich, 2006). Other work has applied the above techniques after confirming that coagulation has an insignificant effect for the analyzed data (Markku Kulmala et al., 2012) or explicitly accounting for the effects of coagulation on GR_m (Lehtipalo et al., 2016; Mark R. Stolzenburg et al., 2005).

This chapter assesses errors of using GR_m calculated using techniques commonly employed in the literature to infer particle growth rates. Our results are especially germane to GR of freshly nucleated particles ranging in size from molecular clusters to about 40 nm. We use time-dependent distribution functions calculated numerically by McMurry and Li (2017) as “data”. The only process contributing to the addition or removal of molecular species in that work (i.e., to particle “growth rates” as is defined above) are condensation and evaporation. Because we understand this model system perfectly, GR_{true} (i.e., the net growth rate due molecular exchange through condensation and evaporation) can be calculated exactly. Errors in GR_m due to coagulation, wall deposition, scavenging by preexisting particles, or dilution, are given by the difference between GR_{true} and GR_m. We do not examine errors associated with convection, source emission, etc.

We are not the first to examine factors that cause GR_m to differ from GR_{true}. For example, Kontkanen (2016) used simulations to show that discrepancies between measured growth rate based on appearance time (AGR) and growth rate based on irreversible vapor condensation (CGR) can be significant. (Note GR_{true} used in this chapter differs from CGR in that GR_{true} also incorporates evaporation.) Our approach, which uses the non-dimensional formulation described by McMurry and Li (2017), provides results that are generally applicable to nucleation and growth of a single chemical species, so long as it is being produced by chemical transformations at a constant rate, R. We show that the upper limit for overestimation of GR_{true} by GR_m occurs when nucleation takes place in the absence of pre-existing aerosols and is collision-controlled (i.e., when evaporation rates from even the smallest clusters occur at rates that are negligible relative to vapor condensation rates). Collision-controlled nucleation is an important limiting case because there is growing evidence that atmospheric nucleation of sulfuric acid with stabilizing species is well-described as a collision-controlled process (Almeida et al., 2013; Kürten et al., 2018; Peter H. McMurry, 1980). Because cluster evaporation, scavenging by preexisting aerosol, etc., all diminish the number of particles formed by nucleation, overestimation of GR_{true} due to coagulation decreases as these processes gain in prominence. We do not explicitly study the effect of growth by processes other than condensation or evaporation, such as heterogeneous growth pathways that take place on or within existing particles. If such processes were to contribute significantly to growth, they would lead to higher growth rates and therefore smaller relative errors in GR_m due to coagulation. Additionally, we point out when particle sink processes consume nucleated particles at a fast rate (e.g. strong effects of dilution or scavenging by preexisting particles), GR_m may not be used to estimate GR_{true}. Our results help to inform estimates of uncertainties for systems with a single condensing species, or systems that can be modeled in a similar way to a single species system (Kürten et al., 2018).

3.2 Methods

3.2.1 Discrete-sectional Model

We utilize the dimensionless discrete-sectional model described by McMurry and Li (2017) to simulate evolution of particle size distribution for a system with a single condensing species. We assume that the condensing species is produced at a constant rate by gas phase reaction. Our code uses two hundred discrete bins and 250 sectional bins, with a geometric volume amplification factor of 1.0718 for neighboring sections.

Physical processes that affect particle growth, including wall deposition, loss to pre-existing particles, cluster evaporation and dilution, can be characterized by dimensionless parameters in this model. In the present study, however, not all aforementioned processes are discussed. Our previous work shows that wall losses, scavenging by preexisting particles and dilution have qualitatively similar effects on aerosol dynamics. Therefore, in this work we focus on preexisting aerosols and dilution to illustrate factors that contribute to errors in measured growth rates, and do not explicitly discuss wall deposition. A single dimensionless parameter, $\sqrt{L}$, is used to indicate the abundance of preexisting particles, with larger $\sqrt{L}$ representing higher concentration of preexisting particles (or, equivalently, a slower rate at which the nucleating species is produced by chemical reaction). $\sqrt{L}$ is calculated with the equation

$$\sqrt{L} = \frac{\frac{1}{4}\left(\frac{8k_bT}{\pi m_1}\right)^{1/2} A_{Fuchs}}{\sqrt{R\beta_{fm\,11}}} \tag{3.3}$$

where A_{Fuchs} is the Fuchs surface area concentration (N. A. Fuchs & A. G. Sutugin, 1971), k_b is the Boltzmann constant, m_1 is the mass of the monomer, R is the condensing species production rate, $\beta_{11\,fm}$ is the monomer collision frequency function. The loss rate for particles containing k monomers is $\sqrt{L}/k^{1/2}$. This size dependence is included when solving the coupled differential equations for time-dependent cluster concentrations. Similarly, the dimensionless quantity M that characterizes dilution is given by the expression

$$M = \frac{Q_{dil}/V}{\sqrt{R\beta_{fm\,11}}} \tag{3.4}$$

where Q_{dil} is the dilution flow rate and V is the volume of the system. Note the fractional dilution loss is independent of particle size. In addition to loss to pre-existing particles and dilution, we consider the effect of cluster evaporation on particle growth with the assumption that evaporation follows the classical liquid droplet model. Two dimensionless parameters, E and Ω, are needed to fully describe the evaporation process.

The dimensionless evaporation parameter, E , is proportional to the saturation vapor concentration of the nucleating species, while Ω is the dimensionless surface tension (Peter H. McMurry & Li, 2017; Rao & McMurry, 1989). The evaporation rate for particles containing k monomers, E_k , is calculated with a discretized equation of the form:

$$E_k = Ec_{1k} \exp\left[\frac{3}{2}\Omega\left(k^{\frac{2}{3}} - (k-1)^{\frac{2}{3}}\right)\right] \tag{3.5}$$

where $c(i,k)$ is the dimensionless collision frequency between a monomer and a particle containing k monomers. To simplify our discussion, Ω is fixed to be 16 throughout this work (a representative value for the surface tension of sulfuric acid aqueous solutions), while the value of E is varied.

The solution to the GDE for a constant rate system (R=constant) depends on dimensionless time, cluster size and the dimensionless variables $\sqrt{L}$, M, E, Ω, etc., but is independent of the rate at which condensing vapor is produced by chemical reaction. That rate is required to transform the computed nondimensional solutions to dimensional results using simple multiplicative expressions given by McMurry and Li (2017):

$$N_k = \left(\frac{R}{\beta_{11\,fm}}\right)^{1/2} \widetilde{N}_k\,;\ t = \left(\frac{1}{R\beta_{11\,fm}}\right)^{1/2} \tau\,;\ d_p = \left(v_1^{1/3}\right)\tilde{d}_p \tag{3.6}$$

In the above equations, $\widetilde{N}_k$ is the dimensionless concentration of particle containing k monomers, τ is the dimensionless time, $\tilde{d}_p$ is the dimensionless particle size and v_1 is the monomer volume. Assuming a monomer volume of 1.62×10^{-22} cm^3 (volume of one sulfuric acid plus one dimethylamine molecule with a density of 1.47 $\mathrm{g/cm^3}$), $\tilde{d}_p =$ 30 would be equivalent to a dimensional particle size of 16.4 nm.

3.2.2 *Evaluation of Measured Growth Rate (GR_m)*

At time t_1 and t_2, if two particle sizes $d_{p,t1}$ and $d_{p,t2}$ are used to represent the particle size distribution, the 'measured' growth rate can be calculated using the following equation as a first order approximation

$$GR_m(\frac{d_{p,t_1}+d_{p,t_2}}{2},\frac{t_2+t_1}{2}) = \frac{d_{p,t_2}-d_{p,t_1}}{t_2-t_1} \quad (3.7)$$

If d_{p,t_i} is available for a time series $\{t_i\}_{i=1,2,...}$, growth rate can also be obtained by derivatizing a fitting function $d_p = d_p(t)$ to obtain growth rate at any time t_a:

$$GR_m(d_p, t_a) = \frac{dd_p(t)}{dt}\Big|_{t=t_a} \quad (3.8)$$

To implement Equation (3.7) or (3.8), it is necessary to choose a particle size that is representative of the particle size distribution at a given time. The choice of this representative size varies among publications and can depend on the types of available data. Based on previous studies (Markku Kulmala et al., 2012; Lehtipalo 2014; Mark R. Stolzenburg et al., 2005; Yli-Juuti, 2011), we have selected four representative sizes for discussion: $\tilde{d}_{p,mode}$, $\tilde{d}_{p,sr100}$, $\tilde{d}_{p,sr50}$ and $\tilde{d}_{p,tot50}$. At a given time τ, $\tilde{d}_{p,mode}$ is the particle size at which $d\tilde{N}(\tau)/dlog_{10}\tilde{d}_p$ reaches its local maximum. If the shape of the mode is log-normal, $\tilde{d}_{p,mode}$ is equal to the geometric mean of the distribution. As suggested by Kulmala et al. (Markku Kulmala et al., 2012), the 'log-normal distribution method' involves calculating growth rates from observed time-dependent trends of $\tilde{d}_{p,mode}$. The 'maximum concentration method' is based on the time when particles in a given size bin, $\tilde{d}_{p,sr100}$, pass through their maximum (100%) concentration (Lehtinen &

Kulmala, 2003). The ‘appearance time’ method is based on the time when particle concentrations in a bin, $\tilde{d}_{p,sr50}$, pass through a specified percentage of its maximum (we have used 50%). Growth rates are sometimes based on total concentrations of particles larger than a specified size. We refer to the particle size above which the total number concentration of particles reaches 50% of its maximum value as $\tilde{d}_{p,tot50}$. This approach is especially useful when measurements are carried out with a battery of CPCs having differing cutoff sizes. For simplicity, in this chapter we assume that CPC detection efficiencies increase from 0% to 100% at a given cutoff size. In practice, measured size-dependent detection efficiencies are typically used when analyzing CPC battery data. Figure 3.1 shows the location of these representative sizes at $\tau = 20, 60, 100$ for two nucleation scenarios in the absence of preexisting particles. $\tilde{d}_{p,mode}$, $\tilde{d}_{p,sr100}$, $\tilde{d}_{p,sr50}$ and $\tilde{d}_{p,tot50}$ are marked as points, with their y-coordinates representing particle concentrations at corresponding sizes.

As will be shown later, values of GR_m obtained with $\tilde{d}_{p,mode}$, $\tilde{d}_{p,sr100}$, $\tilde{d}_{p,sr50}$ or $\tilde{d}_{p,tot50}$ are not equal. To differentiate these cases, GR_m are notated as $GR_{m,mode}$, $GR_{m,sr100}$, $GR_{m,sr50}$ and $GR_{m,tot50}$ accordingly.

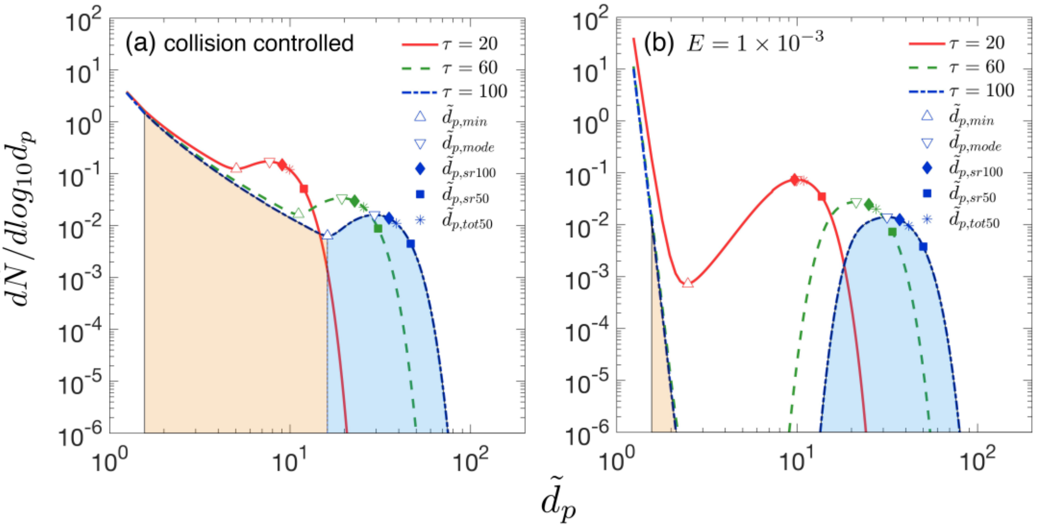

Figure 3.1. Particle size distributions at dimensionless times $\tau = 20, 60, 100$ (a) for collision-controlled nucleation and (b) when evaporation is included with $E = 1 \times 10^{-3}$. Division of the distribution into monomer, cluster and nucleation mode is displayed for $\tau = 100$, with beige and light blue indicating the range of clusters and nucleation mode. Clusters and nucleation mode are separated by $\tilde{d}_{p,min}$, where $d\tilde{N}/dlog_{10}\tilde{d}_p$ is at a local minimum. Characteristic sizes $\tilde{d}_{p,mode}$, $\tilde{d}_{p,sr100}$, $\tilde{d}_{p,sr50}$ and $\tilde{d}_{p,tot50}$ are marked for each time. The relationship between symbols and characteristic sizes is shown only for τ=100.

3.2.3 Evaluation of True Growth Rate (GR_{true})

The true growth rate (GR_{true}) defined in this work follows the Lagrangian approach (Olenius, Riipinen, Lehtipalo, & Vehkamäki, 2014), i.e. tracking the volume change of individual particles, and only includes molecular species exchange by condensation and evaporation. It is calculated with the following expression:

$$GR_{true} = \frac{d\tilde{d}_p}{d\tau} = \frac{2}{\pi\tilde{d}_p^2}\frac{d\tilde{V}}{d\tau} = \frac{2}{\pi\tilde{d}_p^2} \cdot \frac{\tilde{V} + c(i,k)\tilde{N}_1 \cdot d\tau - E_k \cdot d\tau - \tilde{V}}{d\tau} = \frac{2(c(i,k)\tilde{N}_1 - E_k)}{\pi\tilde{d}_p^2} \qquad (3.9)$$

where $\tilde{d}_p$ is the representative size, $\tilde{N}_1$ is the concentration of monomers, and E_k is the particle evaporation rate given by Equation (3.5).

If evaporation is negligible ($E = 0$) and $\widetilde{N}_1$ is constant, Equation (3.9) leads to a higher growth rate for smaller particles, mainly because of the increased monomer collision frequency relative to particle size (Tröstl et al., 2016). Throughout this work Equation (3.9) is used to evaluate true particle growth rate. Note GR_{true} is calculated from dimensionless size and time, and is therefore dimensionless. Since we focus on relative values of true and measured growth rates, our conclusions are unaffected by the dimensionality of GR. However, dimensionless growth rates can be converted to dimensional values with Equation (3.6).

3.3 Results and Discussion

3.3.1 Error of Using $GR_{m,mode}$ as GR_{true}

As mode diameter ($\tilde{d}_{p,mode}$) is often employed to derive particle growth rate, in this section we discuss the error of using $GR_{m,mode}$ as a substitute for GR_{true} in the absence of preexisting particles. The effect of preexisting particles is discussed in Sect. 3.3.

Both condensation and coagulation lead to growth of $\tilde{d}_{p,mode}$. To understand their relative importance, we attribute $GR_{m,mode}$ to three processes: monomer condensation minus evaporation (GR_{true}), coagulation of the mode with clusters ($GR_{m,cluster}$) and self-coagulation of the mode ($GR_{m,self}$). The latter two processes are the main causes of the discrepancy between $GR_{m,mode}$ and GR_{true}. To evaluate $GR_{m,cluster}$ and $GR_{m,self}$, the range of 'clusters' and 'mode' are defined as illustrated in Figure 3.1 by the two shaded regions at $\tau = 100$: clusters (beige) and nucleation mode (light blue). Clusters and nucleation mode are separated by $\tilde{d}_{p,min}$, where $d\tilde{N}/dlog_{10}\tilde{d}_p$ is at a local minimum. Stolzenburg et al.(2005) assumed the nucleation mode is lognormal and calculated GR_{true} and $GR_{m,self}$ with the method of moments. In this work, since the mode for collision-controlled nucleation deviates significantly from log-normal (see Figure 3.1a), no assumption regarding the shape of the nucleation mode is made. Instead, $GR_{m,cluster}$, $GR_{m,self}$ are calculated with the first order numerical approximation method outlined in Appendix A.

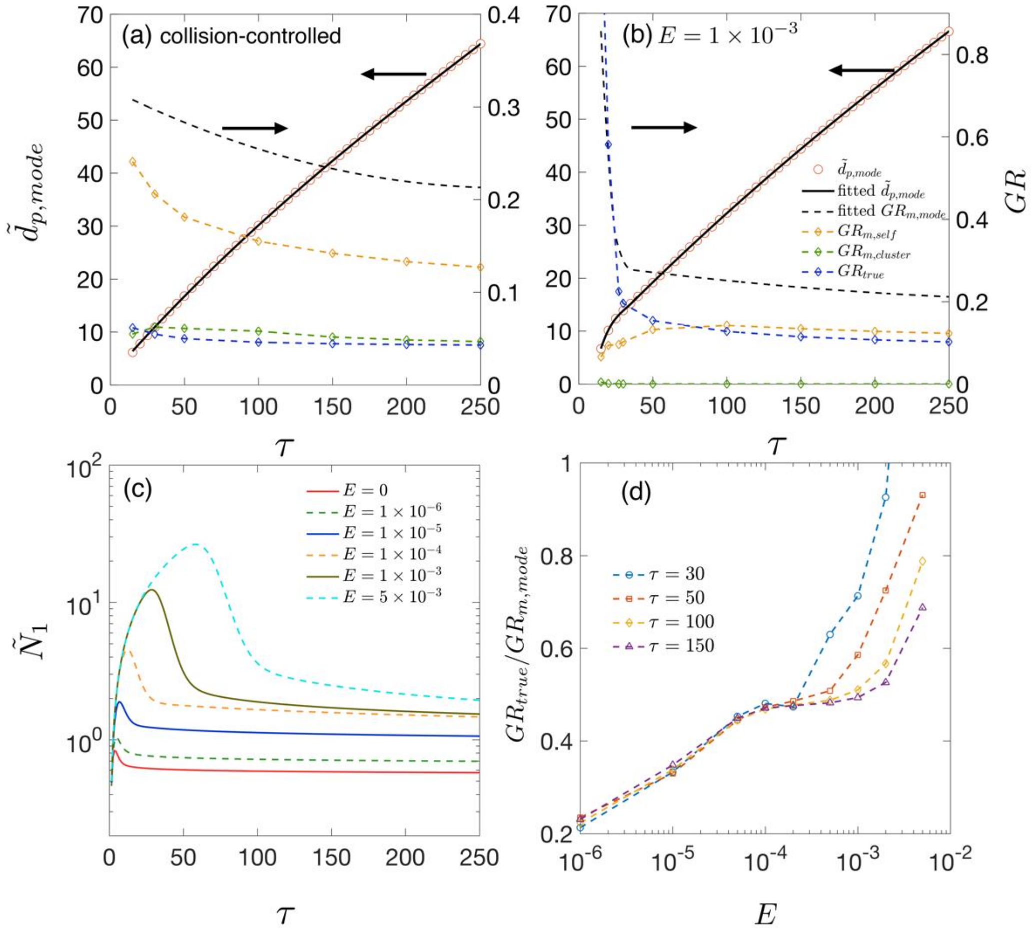

Figure 3.2. (a) $\tilde{d}_{p,mode}$ and various growth rates as functions of time for collision-controlled nucleation. Dashed black lines show the value of $GR_{m,mode}$. Yellow, green and blue dashed lines represent $GR_{m,slef}$, $GR_{m,cluster}$ and GR_{true} respectively. **(b)** The

same quantities as are shown in (a) but with the evaporation constant set to $E = 1 \times 10^{-3}$. For both Figure 3.2a and 3.2b, the left axis shows value for the solid lines and the right axis shows values for the dashed lines. **(c)** Monomer concentration as functions of time for different values of E. (d) $GR_{true}/GR_{m,mode}$ for different values of E at $\tau = 30, 50, 100, 150$.

The calculation results are summarized by Figure 3.2. We first consider collision-controlled nucleation (*E*=0). For this nucleation scenario, Figure 3.2a shows $\tilde{d}_{p,mode}$ on the left y axis and growth rate values on the right. A third order polynomial is used for fitting $\tilde{d}_{p,mode} = \tilde{d}_{p,mode}(\tau)$ and is plotted as a solid black line. Differentiating the fitted polynomial with respect to time gives the value of $GR_{m,mode}$. It is clear that GR_{true} only accounts for a small fraction (17%-20%) of GR_m and is on par with contribution of $GR_{m,cluster}$ (15%-22%). Self-coagulation is the major contributor (62%-78%) to GR_m. Thus, using $GR_{m,mode}$ as a substitute for GR_{true} leads to an overestimation by as much as a factor about 6. We believe collision-controlled nucleation (*E*=0) in the absence of other particle loss mechanisms such as wall deposition (*W*=0) and scavenging by pre-existing particles ($\sqrt{L}$=0) provides an upper limit for overestimation of GR_{true} for a constant rate system (*R*=constant). This is because these conditions lead to the maximum number of particles that can be produced by nucleation. High concentrations lead to high coagulation rates, and it is coagulation that is primarily responsible for errors in GR_m. Furthermore, as is discussed below, the absence of evaporation and scavenging by nucleated particles keeps monomer concentrations low relative to values achieved when *E*≠0 (see Figure 3.2a). Low monomer concentrations reduce the value of GR_{true}, thereby increasing relative errors in GR_m.

Distinctive features of particle growth emerge when cluster evaporation is included by setting $E = 1 \times 10^{-3}$. Figure 3.2b shows results for this nucleation scenario. Most noticeably, particles grow considerably faster at early stages of simulation. This occurs because evaporation depletes clusters and correspondingly increases monomer concentration. In the absence of pre-existing particles, monomer concentration accumulates until the supersaturation is high enough for nucleation to take place (see Figure 3.2c). The accumulated monomers then rapidly condense on the nucleated particles, leading to the rapid particle growth shown in Figure 3.2b. To capture this rapid growth, two third-order polynomials are used to fit $\tilde{d}_{p,mode}$ values for $\tau < 40$ and $\tau > 35$ respectively, with an overlapping region for $35 < \tau < 40$. Furthermore, in comparison to collision-controlled nucleation, contribution of $GR_{m,cluster}$ to $GR_{m,mode}$ becomes negligible, due to decreased cluster concentration by evaporation. For $\tau > 30$, GR_{true} accounts for about 40%-55% of $GR_{m,mode}$, larger than that of collision-controlled nucleation; for $\tau < 25$, GR_{true} almost entirely accounts for $GR_{m,mode}$ and even exceeds $GR_{m,mode}$ at the very beginning of the nucleation. $GR_{true} / GR_{m,mode}$ >1 indicates a rapidly forming nucleation mode, where freshly nucleated particles enter the mode and skew the mode distribution toward smaller sizes, slowing down the shift of the mode peak towards larger values.

Increase of $GR_{true} / GR_{m,mode}$ by evaporation is explained by the elevated monomer concentration due to particle volatility and the smaller number of particles formed by nucleation: the former increases GR_{true}, and the latter decreases $GR_{m,self}$ and $GR_{m,cluster}$. Figure 3.2c plots monomer concentration $\widetilde{N}_1$ as a function of time for several values of E. Noticeably, monomer concentration elevates with E since higher cluster evaporation rates require higher monomer concentrations (i.e., higher supersaturation) to overcome the energy barrier of nucleation. Once nucleation takes place, high monomer concentration leads to rapid nanoparticle growth rates.

Figure 3.2d shows $GR_{true}\ /GR_{m,mode}$ at $\tau = 30, 50, 100, 150$ for several E values. At a given time, $GR_{true}/GR_{m,mode}$ clearly increases with E: when evaporation rates are not negligible (i.e., $E \neq 0$), $GR_{m,mode}$ is closer to GR_{true} than occurs when E=0. Again, this is because the elevated monomer concentrations increase GR_{true} and the lowered concentrations of clusters and nucleated particles decrease $GR_{m,cluster}$ and $GR_{m,self}$. As E approaches 0, the value of $GR_{true}/GR_{m,mode}$ converges to that of the collision-controlled nucleation (~0.2). One data point, corresponding to $E = 5 \times 10^{-3}$ and $\tau = 30$, with a value of 1.8, is not shown in Figure 3.2d. It has a value significantly greater than unity because of the large quantities of nucleated particles entering the mode, skewing the mode peak toward smaller sizes.

3.3.2 Comparison of Representative Sizes

In this section we examine how observed growth rate depends on the choice of a representative size. The application of $GR_{m,mode}$ to deduce GR_{true}, though convenient in practice, depends on the existence of a nucleation mode. However, the nucleation mode is usually not well defined in the early stage of nucleation. In contrast, growth rate based on other representative sizes ($\tilde{d}_{p,sr50}$, $\tilde{d}_{p,sr100}$ and $\tilde{d}_{p,tot50}$) are not dependent on mode formation and are available for all particle sizes. In light of this, $GR_{m,sr100}$,

$GR_{m,sr50}$, $GR_{m,tot50}$ have often been employed to describe the growth rate of small particles (<5nm). The effects of pre-existing particles are neglected in this section (i.e., $\sqrt{L} = 0$) but are discussed in Sect. 3.3.

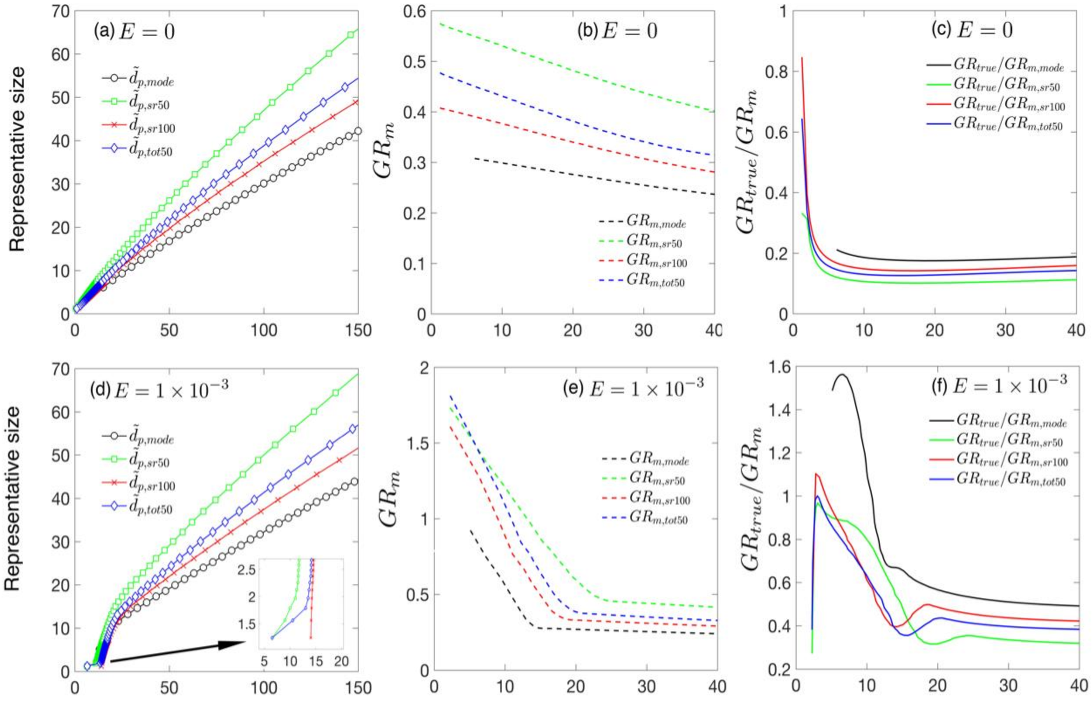

Figure 3.3. (a) $\tilde{d}_{p,mode}$, $\tilde{d}_{p,sr100}$, $\tilde{d}_{p,tot50}$, $\tilde{d}_{p,bin50}$ as functions of time. (b) Measured growth rates $GR_{m,mode}$, $GR_{m,sr100}$, $GR_{m,sr50}$, $GR_{m,tot50}$ as functions of representative sizes. (c) Ratio of true growth rate to measured growth rate, GR_{true}/GR_m. Figures 3.3a-3.3c are for collision-controlled nucleation with E=0. Figures 3.3d-3.3f show the same quantities as are shown in Figure 3.3a-3.3c but with $E = 1 \times 10^{-3}$.

For collision-controlled nucleation, $\tilde{d}_{p,mode}$, $\tilde{d}_{p,sr50}$, $\tilde{d}_{p,sr100}$, $\tilde{d}_{p,tot50}$ are plotted as functions of time in Figure 3.3a. The magnitude of the representative sizes follow $\tilde{d}_{p,mode} < \tilde{d}_{p,bin100} < \tilde{d}_{p,tot50} < \tilde{d}_{p,bin50}$, as was previously illustrated in Figure 3.1a. $\tilde{d}_{p,mode} < \tilde{d}_{p,bin100}$ indicates that a certain measurement bin first reaches its maximum concentration and becomes a local maximum at a later time. This is true for collision-controlled nucleation with a decreasing peak concentration but is not necessarily true for other nucleation scenarios. The observed growth rate (i.e. slope of curves in Figure 3.3a) are shown in Figure 3.3b as a function of representative size, with a clear relationship $GR_{m,mode} < GR_{m,sr100} < GR_{m,tot50} < GR_{m,sr50}$. Note that $GR_{m,mode}$ is not available for small sizes, indicating the nucleation mode is yet to form at the early stage of nucleation. Figure 3.3c shows GR_{true} / GR_m as a function of representative size, with GR_{true} calculated with Equation (3.9). Clearly GR_{true} accounts for the highest percentage of GR_m at the start of nucleation. This is partly due to higher monomer concentrations (see red solid curve in Figure 3.2c) and partly due to Equation (3.9) that leads to higher true growth rate for smaller particles: the addition of a monomer leads to a bigger absolute as well as fractional diameter growth for small particles.

Figures 3.3d-3.3f are counterparts of Figures 3.3a-3.3c, but with evaporation constant E set to 1×10^{-3}. Figure 3.3d show that $\tilde{d}_{p,sr50}$ and $\tilde{d}_{p,tot50}$ increase relatively slowly at the start of the simulation (see the amplified figure at the lower right corner of Figure 3.3d; for reference, the dimensionless sizes of monomer, dimer and trimer are 1.24, 1.56 and 1.79 respectively). Subsequently, a marked change slope of the $\tilde{d}_p = \tilde{d}_p(\tau)$ curve is observed, indicating accelerated particle growth. This reflects that nucleation occurs with a burst of particle formation following a process of monomer and cluster accumulation. The slow growth of the smallest clusters is an indication that the accumulation process is slow due to the strength of the Kelvin effect.

Figure 3.3e shows GR_m obtained by curve fitting after the nucleation burst and Figure 3.3f shows the corresponding GR_{true} / GR_m values. Different from collision-controlled nucleation, there is a sharp rise of GR_{true}/GR_m value at the start of nucleation.

This is due to the sharp decrease of the evaporation term in Equation (3.9), causing the value of GR_{true} to increase sharply. As nucleation progresses, the ratio of GR_{true} to $GR_{m,sr100}$, $GR_{m,tot50}$ and $GR_{m,sr50}$ comes close to 1, with $GR_{m,mode}$ not yet available. Eventually, GR_{true}/GR_m for all representative sizes decreases and fall into the range of 30%-50%, with $GR_{m,mode}$ giving the best estimate of GR_{true}. Note the value of $GR_{true}/GR_{m,mode}$ significantly exceeds unity for $\tilde{d}_p \in [5,11]$ due to the distortion of the mode toward smaller sizes by high flux of freshly nucleated particles into the mode.

3.3.3 Effect of Pre-existing Particles

Pre-existing particles act as particle sinks to decrease the intensity of nucleation. Similarly, in chamber experiments, though loss to pre-existing particles is often eliminated by using air that is initially particle-free, loss of particles to chamber walls is inevitable. Since wall loss and loss to preexisting particles have qualitatively similar effects on nucleation (Peter H. McMurry & Li, 2017), we selectively examine the effect of preexisting particles on growth rate measurements to qualitatively illustrate the effects of all of these processes. To probe the initial stage of nucleation, we use $\tilde{d}_{p,bin50}$ as the basis for our analysis, with a comparison of representative sizes presented at the end of this section. As to the magnitude of $\sqrt{L}$, we choose $\sqrt{L} \in [0,0.3]$ based on previous work. It was shown in Figure 3.2b in McMurry and Li (2017) that as $\sqrt{L}$ exceeds 0.1, particle size distributions begin to deviate discernably from the collision-controlled case. In addition, $\sqrt{L} \approx 0.2$ was observed in the ANARChE field campaign carried out in Atlanta for nucleation events with sulfuric acid as the major nucleating species (C. Kuang, Riipinen, Yli-Juuti, et al., 2010).

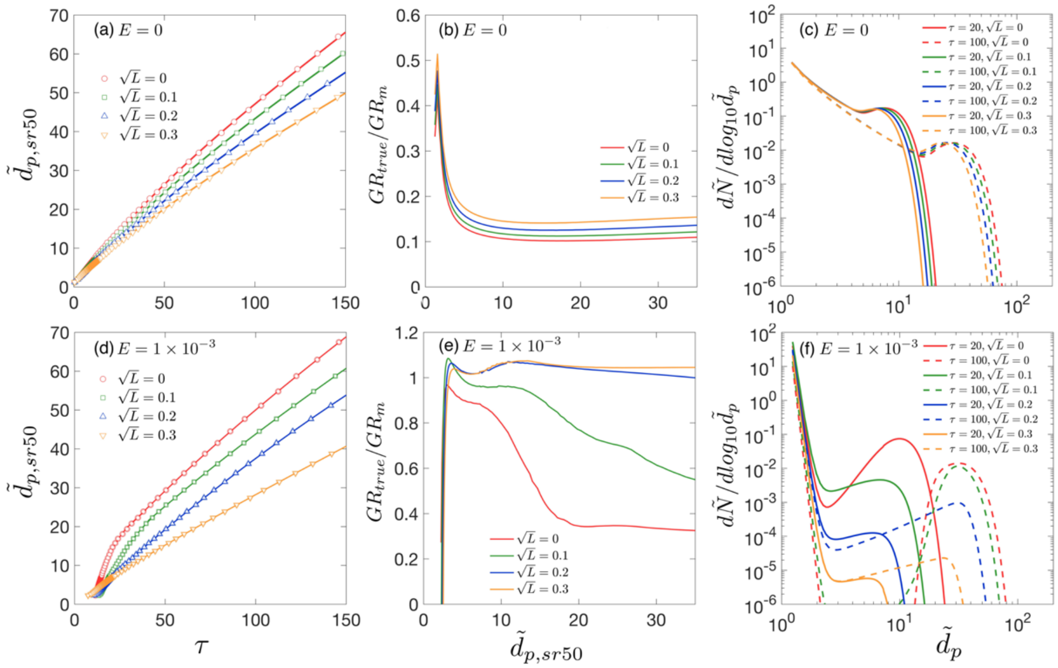

Figure 3.4. Effect of preexisting particles on particle growth rate. **(a)** $\tilde{d}_{p,sr50}$ as a function of time. **(b)** Ratio of true growth rate to measured growth rate, $GR_{true}/GR_{m,sr50}$. **(c)** Particle size distributions at $\tau = 20$ and $\tau = 100$. Figures 3.4a-3.4c are for collision-controlled nucleation with $E = 0$ and $\sqrt{L} = 0, 0.1, 0.2, 0.3$. Figures 3.4d-3.4f show the same quantities as are shown in Figures 3.4a-3.4c but with $E = 1 \times 10^{-3}$.

The influence of preexisting particles on the discrepancy between true and measured growth rate (GR_{true}/GR_m) is twofold. On one hand, preexisting particles can decrease monomer concentration which leads to a smaller GR_{true}. On the other hand, preexisting particles reduce coagulation by scavenging nucleated particles, which could result in a narrower gap between GR_{true} and GR_m. Therefore, the response of GR_{true}/GR_m to $\sqrt{L}$ depends on the relative magnitude of these two competing effects. Figure 3.4a shows $\tilde{d}_{p,sr50}$ as a function of time for several $\sqrt{L}$ values and Figure 3.4b displays the corresponding GR_{true} / GR_m values. It can be seen that GR_{true} / GR_m positively correlates with $\sqrt{L}$, indicating preexisting particles are more effective in removing nucleated particles than reducing monomer concentrations. In fact, as further demonstrated by Figure 3.4c, monomer concentrations (leftmost point of all the curves) are barely affected: scavenging of monomers by preexisting particles are offset by less condensation of monomers onto nucleated particles. Note that for the range of $\sqrt{L}$ values examined, the presence of preexisting particles alter GR_{true}/GR_m values by no more than 50% for collision-controlled nucleation.

Figures 3.4d-3.4f show the same quantities as are shown in Figure 3.4a-3.4c, but with E set to 1×10^{-3} instead of zero. In contrast to collision-controlled nucleation, pre-existing particles significantly affect the nucleation process when cluster evaporation is taken into account. As $\sqrt{L}$ increases, Figure 3.4e shows GR_{true}/GR_m converges to a value slightly larger than unity. This indicates that the contribution of coagulation to measured growth rate approaches zero as $\sqrt{L}$ becomes large; or equivalently, the concentration of nucleated particles is severely decreased by pre-existing particles. Values of $GR_{true}/GR_{m,sr50}$ slightly exceed unity for large sizes (Figure 3.4f) due to the slightly higher condensational growth rates of smaller particles in the nucleation mode. This shifts values of $\tilde{d}_{p,sr50}$ towards smaller sizes than would occur if all particles were to grow at the same rate, causing $GR_{m,sr50}$ to be smaller than GR_{true}.

The decrease of nucleated particle concentration is further demonstrated in Figure 3.4f. From $\sqrt{L} = 0$ to $\sqrt{L} = 0.3$, the peak concentration of nucleated particles dropped by about three orders of magnitude. Such a decrease in concentration of nucleated particles results from the limiting effect of $\sqrt{L}$ on monomer concentration. If pre-existing particles are absent, then no major loss mechanisms for monomers exist prior to the nucleation burst. Monomer would accumulate until the nucleation energy barrier can be overcome: the higher the energy barrier, the higher the monomer concentration prior to nucleation, as shown in Figure 3.2c. The elevated monomer concentration then leads to rapid growth of freshly nucleated particles immediately following the nucleation burst. However, in the presence of pre-existing particles (i.e., $\sqrt{L} \neq 0$), monomer concentration can only increase to the point where its production and consumption by preexisting particles reach balance, prohibiting its concentration from reaching a high value even prior to the nucleation burst. To facilitate comparison with experimental results, in Appendix B we provide an example of conversion from dimensionless distributions and growth rates to dimensional ones.

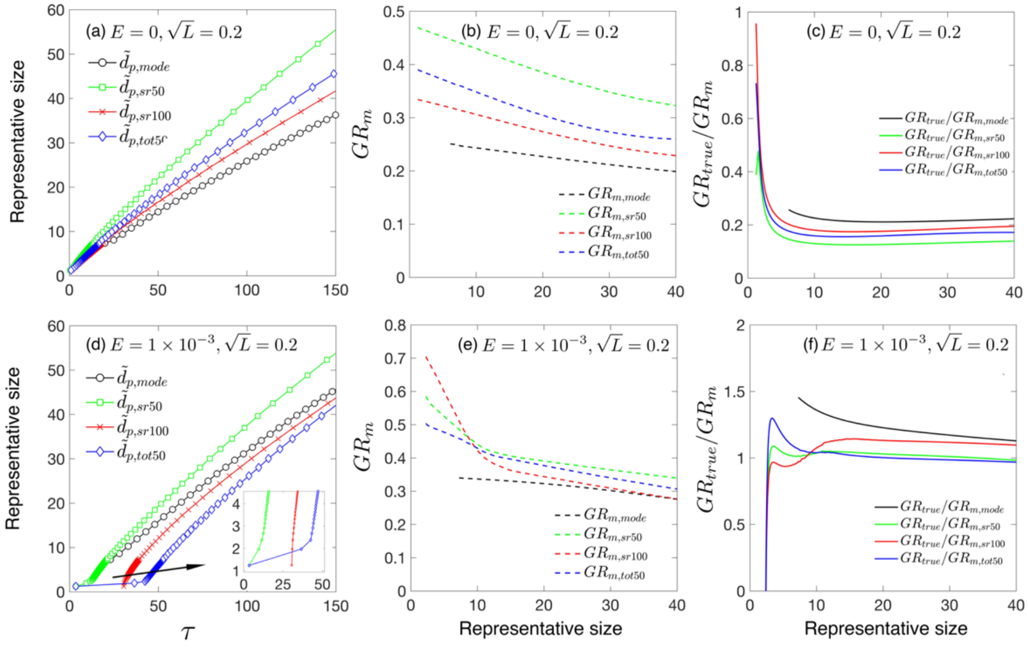

Figure 3.5. (a) $\tilde{d}_{p,mode}$, $\tilde{d}_{p,sr100}$, $\tilde{d}_{p,tot50}$, $\tilde{d}_{p,bin50}$ as functions of time. (b) Measured growth rate $GR_{m,mode}$, $GR_{m,sr100}$, $GR_{m,sr50}$, $GR_{m,tot50}$ as functions of representative sizes. (c) Ratio of true growth rate to measured growth rate, GR_{true}/GR_m. Figures 3.5a-3.5c are for collision-controlled nucleation with $E = 0$ and $\sqrt{L} = 0.2$. Figures 3.5d-3.5f show the same quantities as are shown in Figure 3.5a-3.5c but with $E = 1 \times 10^{-3}$.

Finally, Figure 3.5 examines the difference between representative sizes used to calculate GR_m when loss to preexisting particles is accounted for. Two cases are presented: (1) collision-controlled nucleation (E=0) with $\sqrt{L} = 0.2$ (Figure 3.5a-3.5c) and (2) nucleation accounting for both cluster evaporation and scavenging by preexisting particles ($E = 1 \times 10^{-3}$ and $\sqrt{L} = 0.2$; Figures 3.5d-3.5f). For collision-controlled nucleation with $\sqrt{L} = 0.2$, the preexisting particles changes nucleation only slightly, although GR_m decreases and GR_{true}/GR_m increases both to a minor extent compared to collision-controlled nucleation in the absence of a preexisting aerosol (compare Figures 3.5a-3.5c to Figures 3.3a-3.3c). The analysis made in the discussion of Figures 3.3a-3.3c still stands for Figures 3.5a-3.5c. For nucleation with evaporation and preexisting particles coupled together (Figures 3.5d-3.5f), three features are worthy of attention. Firstly, compared to evaporation-only nucleation, GR_m is significantly decreased for small particle sizes. For $\tilde{d}_p < 10$, GR_m is no larger than 0.7 with preexisting particles but can be greater than 1.5 without (refer to Figure 3.3e). Secondly, as shown in Figure 3.5f, $GR_{true}/GR_{m,sr50}$ and $GR_{true}/GR_{m,tot50}$ come close to unity due to negligible coagulation effects. Third, $GR_{true}/GR_{m,mode}$ is between 1.2 and 1.5 and $GR_{true}/GR_{m,sr100}$ is between

1.1 and 1.2 for $\tilde{d}_p > 10$, indicating the true growth will be slightly underestimated if $\tilde{d}_{p,mode}$ or $\tilde{d}_{p,sr100}$ is used to infer GR_{true}.

3.4 Underestimation of GR_{true}

In previous sections, mainly overestimation of the GR_{true} by measured growth rate, GR_m, has been discussed. Though we do not quantitatively study underestimation of GR_{true} by GR_m, in this section we show that in a constant rate system where particle sink processes (i.e. dilution and loss to pre-existing particles) strongly decrease the concentration of nucleated particles, GR_m can approach zero and cannot be utilized to estimate GR_{true}. Figure 3.6 shows such nucleation scenarios for (a) collision-controlled nucleation with M = 0.1 and (b) collision-controlled nucleation with $\sqrt{L} = 1.5$. In both cases other sink processes were set equal to zero. As shown in both Figure 3.6a and 3.6b, particle size distributions approach steady state after $\tau = 100$. As a result, the measured growth rate GR_m approaches zero beyond $\tau = 100$. At the same time, true growth rate remains finite since monomer concentration remains at steady state after $\tau = 20$. Therefore, other methods have to be utilized to infer GR_{true} in such situations.

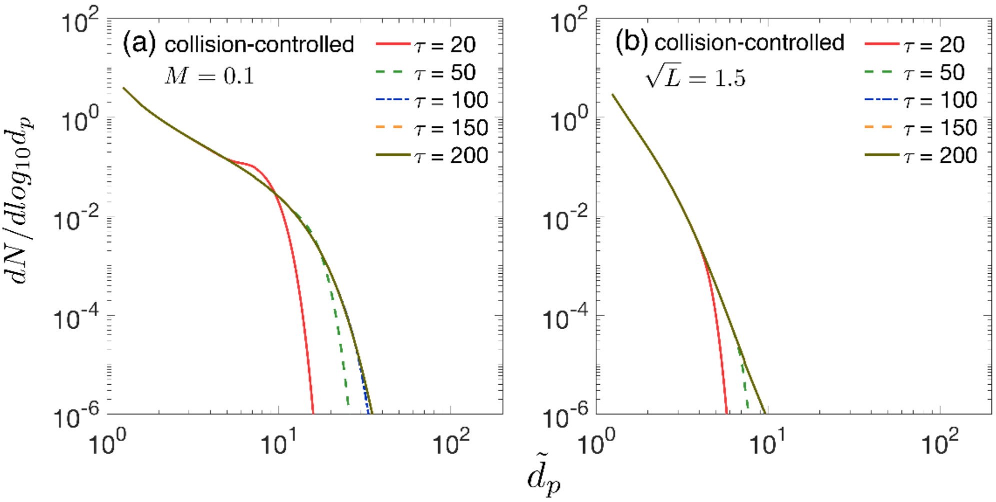

Figure 3.6. Particle size distribution for collision-controlled nucleation with (a) M=0.1 and (b) $\sqrt{L} = 1.5$. In both cases, sink processes not indicated in the figures were set to zero in the simulations.

3.4 Conclusions

We used a discrete-sectional model to solve a dimensionless form of aerosol population balance equation for a single-species system. True growth rate and various “measured” growth rates were examined for a variety of nucleation scenarios. Based on the simulation results, we draw the following conclusions:

1. Simulated data shows that for collision-controlled nucleation without preexisting particles, growth rates inferred from the modal size of nucleated particles ($GR_{m,mode}$) is as much as 6 times greater than true growth rates due to vapor condensation (GR_{true}).
2. In the absence of preexisting particles or other sink processes, comparison of different growth rates based on different representative sizes indicates the relationship $GR_{m,mode}$<$GR_{m,sr100}$<$GR_{m,tot50}$<$GR_{m,sr50}$ holds true for collision-

controlled nucleation. If clusters evaporate, the nucleation process is characterized by rapid particle growth following the nucleation burst.

3. Both evaporation and scavenging by preexisting particles can reduce the concentration of particles formed by nucleation. Lower particle concentrations reduce the effect of coagulation on GR_m, so overestimation of GR_{true} by GR_m is lower than is found in the absence of these processes.
4. Preexisting particles have dramatically different effects on collision-controlled nucleation and nucleation with cluster evaporation. For $\sqrt{L} \in [0,0.3]$, collision-controlled nucleation is only slightly affected. However, if preexisting particles are coupled with evaporation, the number of nucleated particles can drop significantly, thus reducing the contribution of coagulation to measure growth rates.
5. GR_m can underestimate GR_{true} in a system with strong dilution or other particle sink processes. Particle size distributions in such nucleation scenarios can approach a steady state that leads to a GR_m close to 0, which underestimates GR_{true}.

Chapter 4: Vapor Specific Extents of Uptake by Nanometer Scale Charged Particles

Abstract: The uptake of vapor molecules by nanometer scale aerosol particles (clusters) is of fundamental importance in aerosol science; uptake is the first step of condensational growth in both the ambient as well as in condensation based particle detectors. However, uptake is not well understood at the nanometer scale. We examined the uptake of organic vapor molecules by nanometer scale sodium chloride cluster ions ($(NaCl)_x(Na^+)_z$ and $(NaCl)_x(Cl^-)_z$) using a differential mobility analyzer coupled with a time-of-flight mass spectrometer. Through monitoring cluster ion inverse mobilities as functions of solvent vapor pressure in the mobility analyzer, the extent of uptake was monitored for 1-butanol, ethanol, methyl ethyl ketone (MEK), and toluene. With butanol vapor pressures in the < 300 Pa range, shifts in inverse mobility excess of a factor of 2 were observed for nearly all examined clusters. Ethanol and MEK uptake led to shifts for positively charged cluster ions upwards of a factor of 1.5. Ethanol exposure led to similar sized shifts for negatively charged clusters ions, while MEK exposure led to negative ion inverse mobility shifts less than a factor of 1.3. Toluene was sorbed much less efficiently than the other solvents; toluene exposure led to shifts in inverse mobility below a factor of 1.2. In total, relative inverse mobility shifts, which are direct functions of the extent of vapor uptake, were found to be only weakly dependent on cluster ion size when compared to the influence of vapor molecular structure and cluster ion charge polarity. Classical (Kelvin-based) models are found inadequate to explain

the observed mobility shifts, and we instead used a site-specific, Langmuir type model to describe the vapor uptake behavior by the cluster ions.

4.1 Introduction

The ability to control vapor uptake by nanoparticles (condensation) with minimal homogeneous nucleation makes possible the design and operation of condensation particle counters (CPCs) (P. H. McMurry, 2000). Critically important to CPC performance is the CPC's activation efficiency curve, i.e. the fraction of sampled particles which are condensationally grown to an optically detectable size, as a function of the original nanoparticle size. Such curves typically take on a value close to unity above a critical size, but decrease rapidly below it. For > 3 nm particles, the critical size is determined largely by the Kelvin effect, i.e. the surface tension driven enhancement in vapor pressure around a small particle. Efforts to decrease the critical size are commonly made by finding working fluids, aerosol flowrates, and temperature settings for which the vapor concentration in the CPC growth region exceeds the Kelvin model predicted vapor pressure at a particle's surface.

Using the Kelvin model as a guide, commercially available CPCs have been developed with critical sizes near 3 nm (Iida et al., 2008; M. R. Stolzenburg & McMurry, 1991). Further, recent improvements in CPC design have led to critical sizes in the 1-2 nm mobility size range (Gamero-Castano & Fernandez de la Mora, 2000; Iida et al., 2009; Chongai Kuang et al., 2012; Vanhanen et al., 2011; Wimmer et al., 2013). However, in investigating condensation onto 1-2 nm particles, several observations have been made suggesting that the Kelvin model alone is inappropriate to fully describe the activation efficiency curve for nanometer scale particles. Specifically, dependencies on particle chemical composition and charge state (i.e. positive or negative) are not expected based on the Kelvin model (and similarly, the Kelvin-Thomson model). Both particle chemical composition and charge state have been experimentally observed to have large effects on CPC activation efficiency in the 1-2 nm range (Iida et al., 2009; Wimmer et al., 2013), with these effects often difficult to decouple from one another (Kangasluoma, Samodurov, et al., 2016). The working fluid chemical composition is also observed to influence activation efficiency in a manner not expected based on the Kelvin model (Iida et al., 2009).

For 1-2 nm particles, which are composed of a limited number of atoms/molecules, the main issue with the Kelvin model is presumably that it invokes bulk matter approximations. In doing so it considers neither effects of molecular scale interactions between the particle and working fluid molecules, nor the influences of particle and vapor molecule structure. Molecular interactions and structure govern completely whether a vapor molecule will bind and remain bound to a surface upon collision and are particularly important at the nanometer scale. Therefore, in spite of the continued use of Kelvin model in predicting condensation and growth rates for nanometer scale species, (M. Kulmala, Kerminen, Anttila, Laaksonen, & O'Dowd, 2004; M. Kulmala, Lehtinen, & Laaksonen, 2006) there is a clear need to better understand vapor molecule sorption onto nanometer scale particles.

Recently, our group has shown it is possible to use a differential mobility analyzer (DMA) coupled to a mass spectrometer (MS) to probe vapor molecule condensation onto nanometer scale particles (ions) (D. R. Oberreit et al., 2015; Thomas et al., 2016) under sub-saturated conditions. Though CPCs invariably operate under supersaturated conditions, subsaturated vapor uptake measurements provide information on the earliest stages of condensation, i.e. they permit examination of the uptake/sorption of several molecules and importantly, the influences of charge state, particle/ion structure and working fluid chemical composition. In DMA-MS measurements (or alternative mobility-mass measurement systems (Rawat, Vidal-de-Miguel, & Hogan, 2015)), charged species migrating through the mobility classification equilibrate with their surroundings, which are laden with vapor at a controlled concentrations. As an ion/particle traverses the mobility classifier vapor molecules sorb and desorb from it; the net result is a shift in the apparent electrical mobility of the ion/particle from its value in the absence of vapor. After mobility analysis but prior to mass measurement, ions/particles pass through a high pressure drop, high electric field interface, in which nearly all vapor molecules evaporate, and the bare ion/particle is detected in the mass spectrometer (yielding its chemical composition). Mobility shifts monitored as function of vapor pressure hence serve to quantify the extent to which a specific vapor sorbs onto chemically identified ions/particles; these shifts have been shown to be directly linked to the equilibrium sorption coefficients for successive vapor molecules, as well as the structures of formed ion/particle-vapor molecule complexes (Oberreit, McMurry, & Hogan, 2014).

To date, this approach has been applied to proof concept measurements of the sorption of water vapor to metal halide ions (D. R. Oberreit et al., 2015), to examine mobility shifts of peptide ions brought about by isopropanol sorption (Rawat et al., 2015), to examine the influence of vapor sorption on protein ion structure (Meyer, Root, Zenobi,

& Vidal-de-Miguel, 2016), and to examine water vapor sorption by dimethylamine-sulfuric acid clusters (Thomas et al., 2016). In this study, our purpose is to extend such DMA-MS measurements to examine the sorption of a commonly employed CPC working fluid (butanol), chemically related compounds, (ethanol, a shorter alcohol than butanol, and methyl ethyl ketone, MEK, a four carbon compound with a different functional group), as well as an aromatic compound (toluene) onto positively and negatively charged sodium chloride clusters/particles of the form $(NaCl)_x(Na^+)_z$ and $(NaCl)_x(Cl^-)_z$ with $x = 1\text{-}30$ and $z = 1\text{-}2$. In doing so, we demonstrate that the influence of vapor molecule chemical structure on the earliest stages of condensation is substantial, and is coupled to the influence of particle charge polarity.

4.2 Experimental Methods

4.2.1 Nanometer Scale Particle/Cluster Generation

Nanometer scale charged species may be interchangeably referred to as cluster ions or charged particles. For consistency with prior DMA-MS literature, in the remainder of this work we refer to the species examined as clusters ions. Sodium chloride cluster ions were generated by electrospray ionization (ESI). The solutions for ESI were prepared using HPLC grade methanol as solvent with sodium chloride concentration of 10mM. Both positive and negative ESI were performed following procedures as described by Hogan and Fernandez de la Mora (Hogan & Fernandez de la Mora, 2009, 2010), using a silica capillary with an inner diameter of 75μm and outer diameter of 360μm. For a given experiment, the ESI was operated in stable cone-jet mode and the current carried by produced drops was maintained to be 100-200nA, with a variation of ±5 nA.

4.2.2 Differential Mobility Analysis-Mass Spectrometry

The DMA-MS system and its operation has been described in detail in previous studies (Rus et al., 2010). Briefly, singly and multiply charged sodium chloride clusters ions were directed electrostatically into a parallel plate DMA (SEADM, Boecillo, Spain) to be separated by electrical mobility. A counter flow of ~0.3 L min^{-1} was used to prevent methanol vapor from entering the DMA. A QSTAR XL quadruple time-of-flight mass spectrometer (qTOF–MS, MDS Sciex) was interfaced with the DMA to determine the mass-to-charge ratio of the selected ions. The DMA was operated with a circulating sheath flow pumped by a vacuum blower. DMA calibration was performed for all experiments by measuring the voltage required to transmit the tetraheptylammonium^{+} ion (produced via ESI of tetraheptylammonium bromide dissolved in methanol), as is commonly used in high sheath flowrate DMA calibration.(Kangasluoma, Attoui, et al., 2016; Ude & Fernandez de la Mora, 2005) To collect mobility spectra, the voltage difference across the DMA electrodes was stepped in 10 V increments in the 800-5000 V range. The temperature of the DMA sheath flow was controlled by a water jacket heat exchanger at 293±0.5K for all experiments. At each DMA voltage difference, a mass spectrum in 10-3000 Th range was collected using the time-of-flight section of the QSTAR XL mass spectrometer. Inlet declustering potentials and focusing potentials, which aid in particle/ion transmission into the mass spectrometer but also promote fragmentation, were set to minimum values, following Thomas et al (Thomas et al., 2016).

The DMA sheath flow consisted of high purity N_2 with an organic vapor (butanol, MEK etc.) concentration in the 0.0% to 0.5% range (0-500 Pa). The organic vapor was added into the sheath flow utilizing a nebulizer as described by Oberreit et al. (2014). A carrier gas flow (N_2) through the nebulizer was maintained at ~0.8 L min^{-1} during all experiments. To ensure the nebulized liquids evaporate completely prior to entering the DMA, the nebulizer was heated to 75˚C with a heating tape. The organic vapor pressure within the DMA was calculated from the organic liquid flow rate (set using a syringe pump) and the carrier gas flow rate. Prior to each measurement, the DMA-MS system (with the sheath flow pump turned on as well as the heat exchanger) was allowed to equilibrate for 1.5-2 hours. In cases where the sorption of vapor changes the electrical mobility significantly, constant organic vapor pressure could be ascertained by observing constant mobilities for a given species over several consecutive measurements.

During DMA-MS measurements, system contamination, even at the parts-per-million level, can influence measurements (Maisser, Thomas, Larriba-Andaluz, He, & Hogan, 2015). Contamination at such levels can arise if impurities are present in the nebulized solvents, which deposit in sheath flow tubing. More concerning is residual solvent from one experiment carrying over to subsequent experiments. Therefore, prior to changing solvents, the DMA plates were thoroughly cleaned by disassembling the DMA and the DMA sheath flow was operated in open loop for hours (days in some cases) without any solvent introduction. To ensure solvent carryover was mitigated, the electrical mobilities of sodium chloride cluster ions were measured in dry N_2 and were normalized by the electrical mobility of the tetraheptylammonium$^+$ ion. Cleaning was repeated until the normalized electrical motilities for each singly charged sodium chloride particle was within 5% of an established baseline value.

4.3 Results and Discussion

4.3.1 Characteristic DMA-MS Mass-Mobility Spectra

Figure 4.1 displays contour plots of the mass-mobility spectra for positively charged sodium chloride cluster ions ($(NaCl)_x(Na^+)_z$). Specifically, Figure 4.1a displays results obtained in the absence of vapor and Figure 4.1b displays results obtained with butanol introduced into the DMA with a vapor pressure of 166 Pa. Following prior DMA-MS studies (Ouyang, Larriba-Andaluz, Oberreit, & Hogan, 2013), on the horizontal axes of contour plots are the inverse mobilities of the cluster ions, while on the vertical axes are x/z values, where x is the number of neutral ion-pairs (NaCl) in the cluster ions and z is number of charges the ions possess. Detected signals for the cluster ions are represented by line segments in the contour plots, with their length defined by the DMA resolution. Signal intensities are indicated by a logarithmic color scale, with yellow indicating the lowest intensity above a set threshold and blue the highest. Because chlorine has two stable isotopes with masses of 35 Da and 37 Da, detection of larger clusters leads to a series of line segments closely spaced in x/z; these lines are not discernable from one another in contour plots. Singly charged cluster ions appear near integer x/z values only, doubly charged ions differ in x/z from another by approximately ½, and higher charge state by $1/z$. As is common for electrospray generated clusters ions,(Hogan & Fernandez de la Mora, 2009) for sodium chloride ions under all measurement conditions we find the line segments are grouped by charge state in specific regions of mass-mobility plots. In Figure 4.1b, both the singly and doubly charged cluster ions are labelled, and the triply charged (z = 3) are circled. Higher charge state cluster ions are detected with lower signal intensities, hence in this study we elect to focus on singly and doubly charged cluster ion only, with a particular emphasis on the singly charged cluster ions.

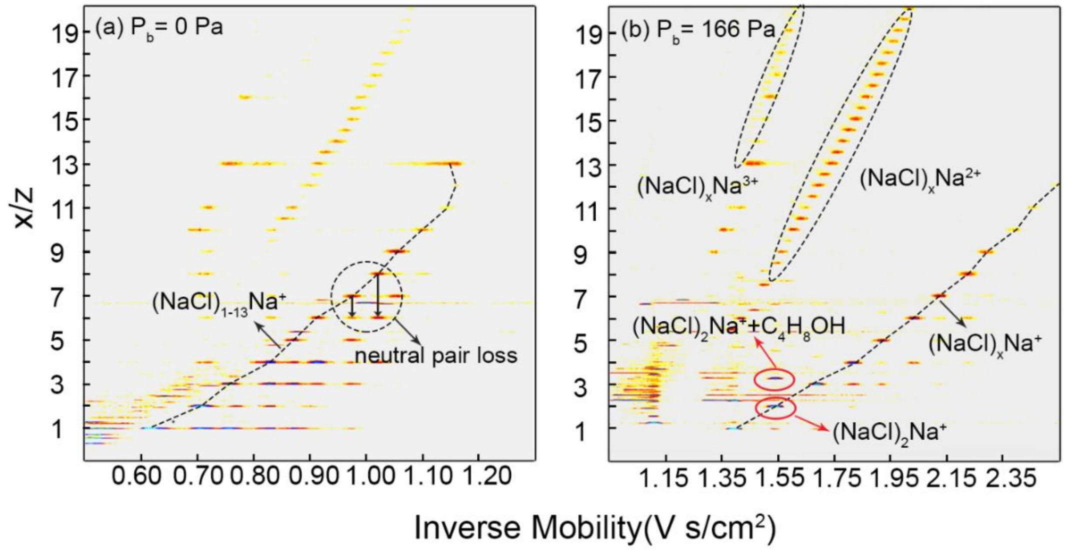

Figure 4.1. Contour plots of mass-mobility spectra for positively charged sodium chloride cluster ions ($(NaCl)_x(Na^+)_z$) in (a) pure N_2 (b) mixture of butanol vapor and N_2 with P_b=166 Pa. Singly charged cluster ions are connected by dashed lines. Doubly and triply charged cluster ions are circled. Signal corresponding to one butanol molecule bound to $(NaCl)_2Na^+$ is red circled in (b). Note the cluster ion inverse mobility approximately doubles at P_b=166 Pa.

Singly charged cluster ions containing up to 13 and 11 neutral pairs, respectively, are connected by dashed lines in (a) and (b). Beneath several identified singly charge cluster ion line segments there are columns of line segments spanning an identical inverse mobility range, but with x/z values differing by one. These signals are the results of neutral ion-pair loss (evaporation) from cluster ions in the inlet of the mass spectrometer, prior to mass measurement ($(NaCl)_xNa^+ \rightarrow (NaCl)_{x-y}Na^+ + (NaCl)_y$) (Hogan & Fernandez de la Mora, 2010; Ouyang et al., 2013; Trimpin & Clemmer, 2008). Other paths of dissociation, which could occur either within the DMA or the mass spectrometer inlet are documented in Ouyang et al (2013) and Thomas et al (Thomas et al., 2016).

Also apparent in contour plots is that the inverse mobilities of singly charged cluster ions are approximately twice as large when measured with a butanol vapor pressure (P_b) of 166 Pa in comparison to dry conditions. This is a significantly larger inverse mobility shift than been observed for nanometer scale ions exposed to water vapor and isopropanol in prior studies (D. R. Oberreit et al., 2015; Rawat et al., 2015; Thomas et al., 2016), and suggests that multiple butanol molecules (on average) are sorbed to the cluster ions in the DMA. These molecules dissociate from cluster ions due collision activation in the mass spectrometer inlet, prior to mass analysis, (D. R. Oberreit et al., 2015) as the measured masses of most cluster ions do not shift in the presence of vapor. However, for the smallest cluster ions ($x = 1$ or 2), signal is detected for some ions at a mass-to-charge ratio 74 Th above the baseline mass-to-charge ratio; this corresponds to the attachment of a single butanol molecule during mass measurement. Such a mass shift provides direct evidence of butanol sorption, in addition to the indirect evidence provided by inverse mobility shifts.

Similar to Figure 4.1, Figure 4.2 displays contour plots for negatively charged cluster ions at $P_b = 0$ Pa, 44 Pa, 66 Pa and 166 Pa. As was the case for positively charged ions, significant vapor uptake appears to take place, and the clusters ions have greatly reduced mobilities (larger inverse mobilities) in the presence of butanol. Positively and negatively charged cluster ion contour plots are qualitatively similar to one another, with line segments results from neutral loss between mobility and mass measurement present. However, the contour plots of negative cluster ions have two noteworthy features which are distinct from the positive case. First, for positively charged cluster ions with z =1, with the exception of the x = 13 cluster ion (a $3 \times 3 \times 3$ cube (Dugourd, Hudgins, & Jarrold, 1997)), *x/z* increases monotonically with inverse mobility. Made apparent by the dashed guideline in Figure 4.2a this correlation is clearly perturbed for negatively charged cluster ions; the cluster ions *x = 3* and *x = 4* have similar inverse mobilities in the absence of vapor, as do the clusters with *x = 7-9*. Second, we note that for positively charged ions, cluster ions of higher mass have higher inverse mobilities than lower mass clusters for all examined vapor pressures (again with the exception of *x = 13*). This is not the case for the *x = 2-4* as well as for the *x = 7- 9* negatively charged ions exposed to both butanol and ethanol; for these ion groups the ions which have the largest and smallest inverse mobilities change with changing vapor pressure. To illustrate this, line segments corresponding to $(NaCl)_7Cl^-$, $(NaCl)_8Cl^-$, and $(NaCl)_9Cl^-$ are circled in all four Figure 4.2 contour plots. In the absence of vapor, these cluster ions are closely packed horizontally with inverse mobility values $\frac{1}{Z_9} > \frac{1}{Z_8} > \frac{1}{Z_7}$ (Z_x is the electrical mobility of the cluster ion containing *x* neutral pairs). As P_b is increased from 0 to 44 Pa, these clusters become separated in mobility, with their relative inverse mobility ranking reserved to $\frac{1}{Z_7} > \frac{1}{Z_8} > \frac{1}{Z_9}$ (i.e. the least massive cluster ion has the largest inverse mobility under this condition). The relative positions of these cluster ions continue to evolve as P_b increases, returning to $\frac{1}{Z_9} > \frac{1}{Z_8} > \frac{1}{Z_7}$ in Figure 4.2d, and remaining as such as P_b is increased further. A phenomenon similar to this is observed for the $(NaCl)_2Cl^-$, $(NaCl)_3Cl^-$ and

$(NaCl)_4Cl^-$ group. This behavior has not been observed previously in examining water uptake by cluster ions (D. R. Oberreit et al., 2015; Thomas et al., 2016); presumably it is related to the structures of the negatively charged sodium chloride cluster ions which give rise to unique inverse mobilities under dry conditions, in addition to leading to unique amounts of vapor uptake.

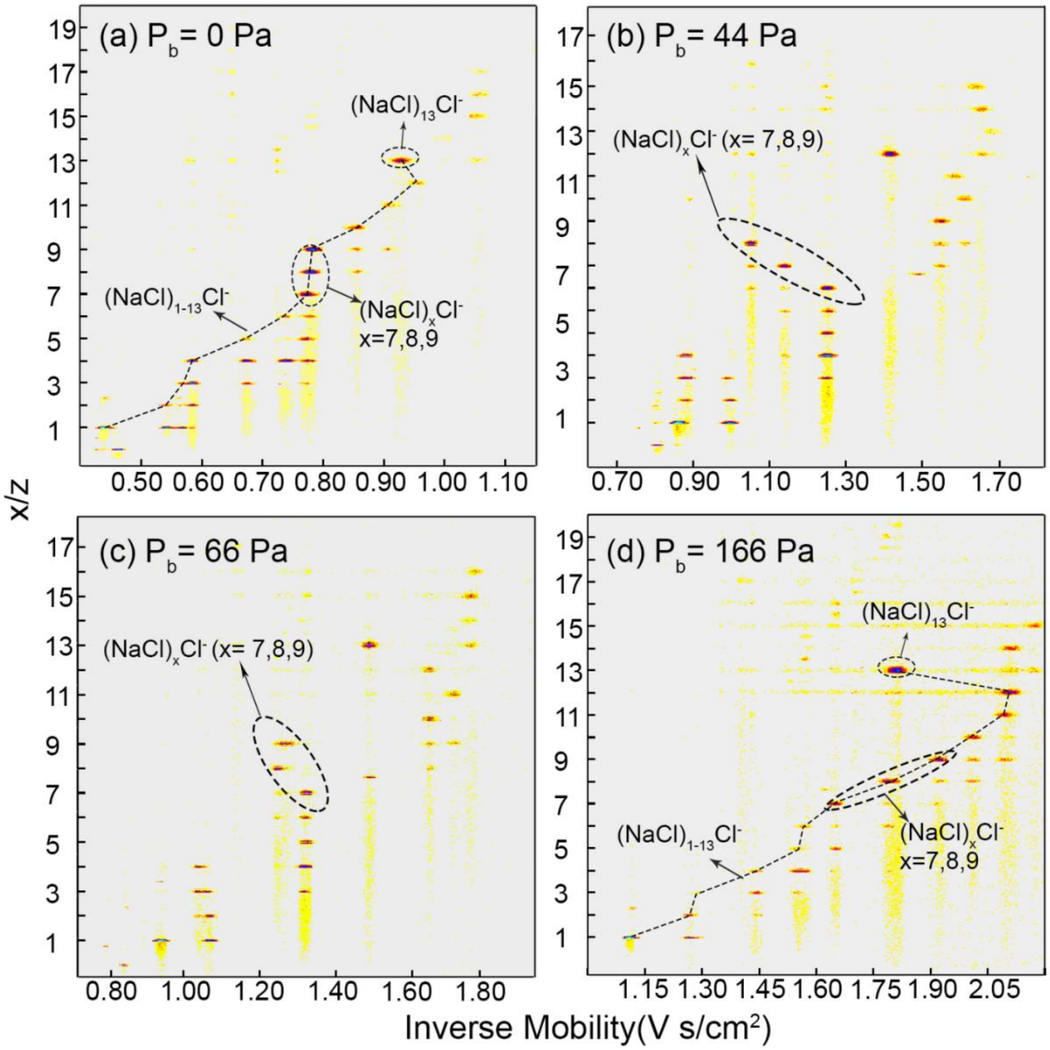

Figure 4.2. Contour plots of mass-mobility spectra for negatively charged sodium chloride cluster ions ($(NaCl)_x(Cl^-)_z$) with (a) P_b=0 Pa, (b) P_b=44 Pa, (c) P_b = 66 Pa, (d) P_b=166 Pa. Singly charged cluster ions are connected by dashed lines. $(NaCl)_xCl^-$ (x = 7,8,9) are circled on each plot to show their relative position change in the contour plots.

4.3.2 Inverse Mobility Shifts due to Vapor Adsorption

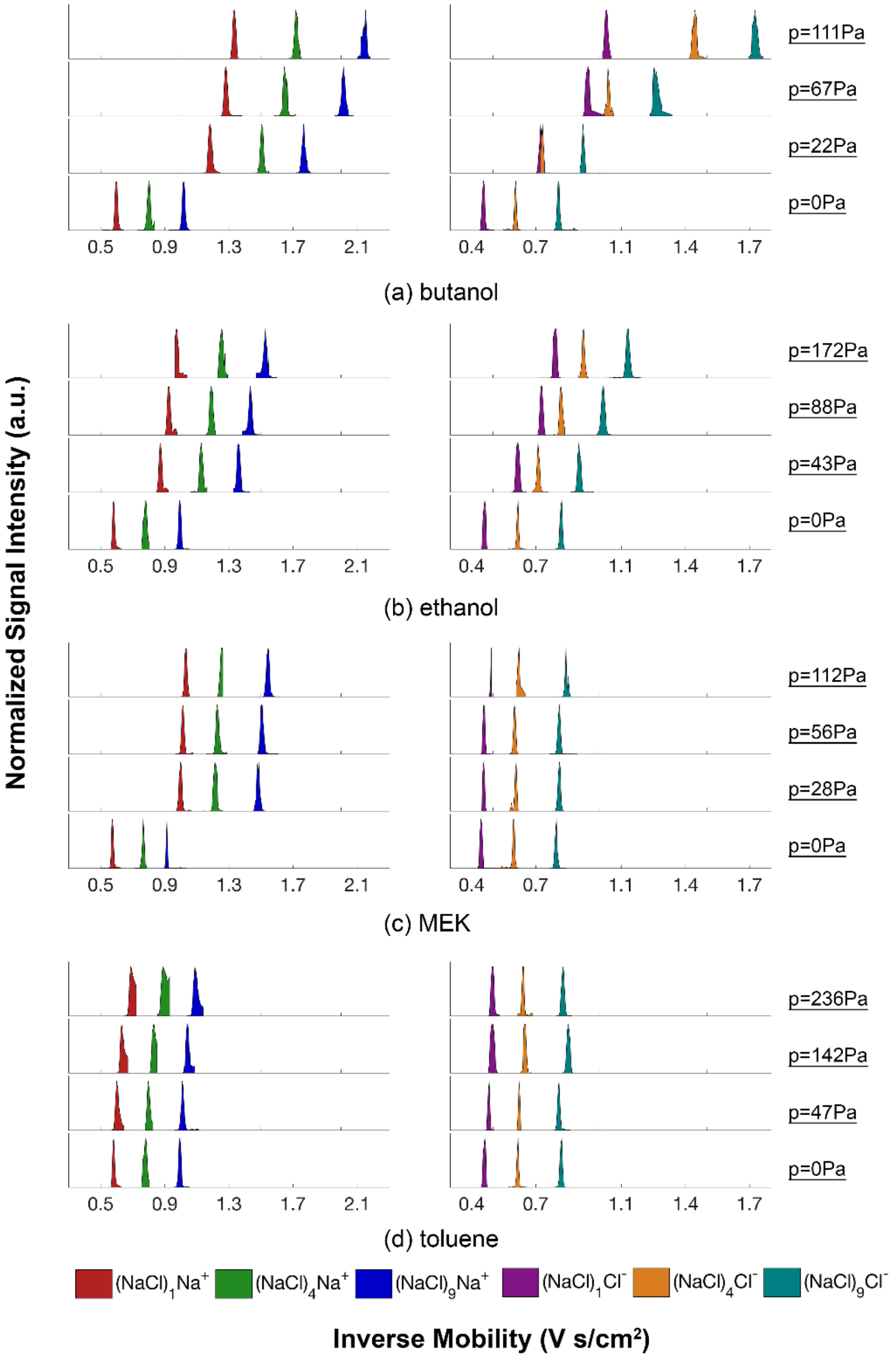

Figure 4.3. Signal intensity-normalized inverse mobility spectra for the singly charged x = 1, 4, and 9 ions (both positively and negatively charged) at selected vapor pressures

within the sheath flow. Results are provided for (a) butanol, (b) ethanol, (c) MEK, and (d) toluene.

It is difficult to explicitly show how the inverse mobility of a particular ion (i.e. an ion of specific x and z) evolves with changing vapor pressure through contour plots alone. We therefore elect to display signal intensity-normalized inverse mobility spectra for the singly charged x = 1, 4, and 9 ions (both positively and negatively charged) at selected vapor pressures in Figure 4.3. Results are provided with (a) butanol, (b) ethanol, (c) MEK, and (d) Toluene. These ions were selected because they are found in higher signal intensity in all measurements (i.e. they were the most easily detected ions). However, similar conclusions to those presented here would result from examination of other singly charged cluster ions. Signals resulting from neutral and ion evaporation events have been removed from Figure 4.3 spectra, hence each peak corresponds to one of the ions of interest. We display results for each vapor type in a similar vapor pressure range; though the tested vapors have disparate saturation vapor pressures we find that $\left.\frac{d\left(\frac{1}{Z_x}\right)}{dP}\right|_T$, the change in inverse mobility per unit change in vapor pressure (at constant temperature), attains a local maximum in in 0 – 200 Pa vapor pressure range. We remark that this observation may simply be coincidence for the vapor examined as is by no means universal for all ion and vapor molecule compositions.

For all tested vapor types, shifts to larger inverse mobilities are apparent, but the extent of shift is clearly vapor molecule type and charge state specific. Specifically, large shifts in inverse mobility for ions (larger than a factor of 1.3 when compared to the dry inverse mobility) are experimentally observed for butanol and ethanol with all singly charged ions (with significantly larger shifts observed for butanol), as well for the positively charged cluster ions exposed to MEK. Conversely, toluene gives rise to smaller mobility shifts for all ions, as does MEK for negatively charged cluster ions. These findings are neither quantitatively nor qualitatively consistent with classical model predictions considering the Kelvin and Thomson influence alone (all vapor molecules have similar surface tensions), the influence sodium chloride dissolution may have on uptake (NaCl is more soluble in ethanol than in butanol), as well as with modifications classical theory (Yu, 2005) considering ion-dipole and ion-induced dipole interactions (MEK has the highest dipole moment of any test vapor molecule, while Toluene has the highest polarizability). While toluene is chemically very distinct from the other test vapors and differences between them are hence anticipated, the other test vapor molecules are chemically related; butanol and ethanol share the same functional group and differ only in carbon chain length, while butanol and MEK share the same number carbons and differ only in functional group. The variable extents of uptake observed for these vapor molecules hence suggest that the earliest stages of heterogeneous condensation onto nanometer scale species are extremely dependent on cluster-vapor molecule interactions, and small changes to vapor molecule chemical structure or ion charge state may have drastic influences on the extent of vapor molecule sorption.

4.3.3 Influence of Charge State

Because of the observed deviations in uptake behavior from what is anticipated based on classical theory, it is of interest to examine the influence of charge state and cluster size on vapor uptake isolated from another. Figure 4.4 displays the variation in inverse mobility for selected cluster ions (x = 1, 4, 9, 13) with butanol, ethanol and MEK partial pressure, both positively and negatively charged. Specifically, normalized inverse mobility, $\left.\frac{1}{Z_x}\right|_P / \left.\frac{1}{Z_x}\right|_0$ the ratio of the inverse cluster ion mobility at partial pressure p and to the dry inverse mobility, is plotted as a function of solvent partial pressure. For the positively charged cluster ions, all the curves are concave downward. The curves obtained for ethanol sorption are the least concave, butanol curves are intermediate, and MEK curves display the greatest concavity, as $\left.\frac{d\left(\frac{1}{Z_x}\right)}{dP}\right|_T$ approaches 0 as MEK partial pressure increases. Concave inverse mobility versus concentration curves have been observed previously for isopropanol sorption onto peptide ions (Rawat et al., 2015), and are also observed when applying mobility to examine protein binding to nanoparticles (Seongho Jeon et al., 2016; Jeon, Oberreit, Van Schooneveld, & Hogan, 2016). In these prior studies, this finding has been interpreted as resulting from the binding of molecules at specific surface site or the formation of a monolayer onto ions/particles. In a subsequent section, we hence compare the positive cluster ion inverse mobility versus partial pressure curves to theoretical models of site specific-binding.

Inverse mobility versus partial pressure curves for negative ions have clear differences from the positive ion curves. The curves describing butanol and ethanol sorption by negatively charged cluster ions intersect with one another, reflecting the relative position change of the signal line segments noted previously (Figure 4.2). In the case of butanol sorption, for negative ions the value of $\left.\frac{d\left(\frac{1}{Z_x}\right)}{dP}\right|_T$ is larger than for positive ions at higher partial pressures (i.e. negative ion curves are less concave). Most prominently, negative cluster ions show minimal uptake of MEK, in stark contrast to positive ions. Meanwhile, fewer differences between the positive and negation ion ethanol sorption curves are discernable.

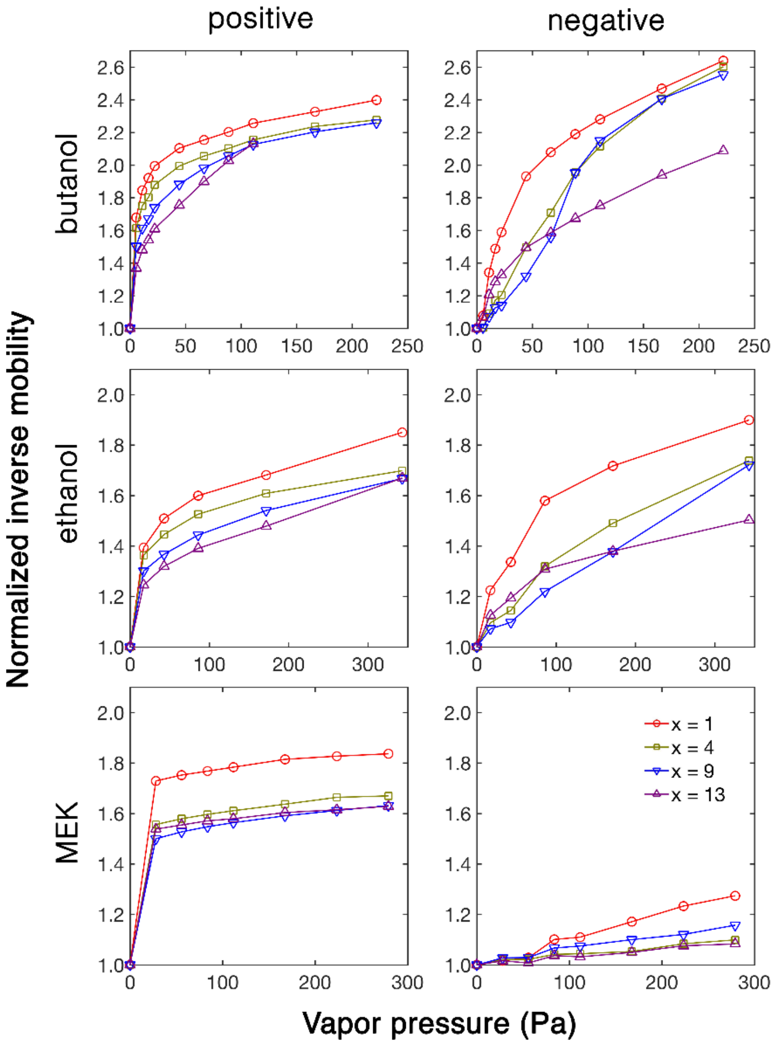

Figure 4.4. Inverse mobilities of selected cluster ions (x = 1, 4, 9, 13) as a function solvent partial pressure.

Though charge state dependencies have been examined and reported previously in CPC activation efficiency studies (Chongai Kuang et al., 2012), recently, Kangasluoma et al (2016) examined heterogeneous nucleation of organic vapor onto tungsten oxide nanoparticle/ion seeds, with a specific focus on examining the influence of nanoparticle/ion charge polarity on the growth process. They suggest that ion charge state is a less important factor in controlling vapor uptake and growth than is the chemical composition of the ions; specifically, they found that positive and negative tungsten oxide ions contained different impurities and that the impurity content had a larger influence on uptake than the charge polarity. We remark that here the ions of interest were chemically identified, contained no impurities, and those of different charge polarity had near identical composition (i.e. positive and negative cluster ions simply have an Na^+ and Cl^- exchanged). Therefore, the differences we observe for different charge state ions cannot be attributed to chemical impurities in ions of different charge state. In total, our comparison of uptake by ions differing in charge state shows that the influence of charge polarity is significant and clearly vapor dependent.

4.3.4 Influence of Cluster Size

Figure 4.5 displays plots of the normalized inverse mobility versus solvent partial pressure curves for $(NaCl)_xNa^+$ (x = 1, 4, 9 ,13) clusters (Figure 4.5a) and for $(NaCl)_x(Na^+)_2$ (x= 21, 27, 31, 34) (Figure 4.5b). For all the cluster ions displayed, sorption of butanol molecules produces the most significant inverse mobility shifts and sorption of toluene molecules produces the least given the same partial pressure. Sorption of MEK molecules results in greater shifts of inverse mobility than ethanol in the pressure range of 0~250Pa for the selected singly charged cluster ions. However, the opposite is observed for doubly charged cluster ions over the entire pressure range; for doubly charged clusters the sorption of ethanol molecules produces larger inverse mobility shifts than MEK (i.e. the magnitude of the charge influences the relative mobility shift).

CPC activation studies and classical theory suggest that cluster/particle size has a large influence on condensational growth. Interestingly, in our measurements, with few exceptions (notably x = 13 with butanol), positively charged cluster ions with the same charge state (+1 or +2) display highly similar normalized inverse mobility versus solvent partial pressure curves for a given solvent vapor. Stated differently, $\Delta\left(\frac{1}{Z_x}\right)$, the shift in inverse mobility appears proportional to $\left(\frac{1}{Z_0}\right)$, hence normalized inverse mobility curves for different sized cluster ions are similar to one another.

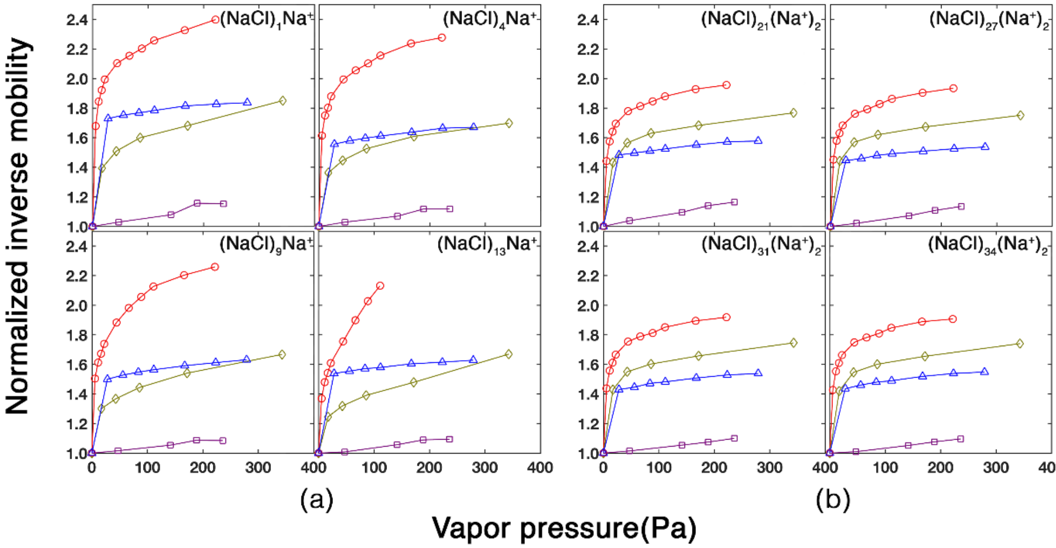

Figure 4.5. Comparison of sorption of different vapors by (a) $(NaCl)_xNa^+$ (x = 1, 4, 9 ,13) and (b) by $(NaCl)_x(Na^+)_2$ (x= 21, 27, 31, 34). Red circles: butanol; Yellow diamonds: ethanol; Blue triangles: MEK; Purple squares: toluene.

4.3.5 Heterogeneous Vapor Uptake Modelling

Observations of inverse mobility versus solvent partial pressure suggest that (1) sorption is highly vapor molecule structure dependent, (2) sorption is charge state dependent, and (3) relative mobility shifts brought about by sorption are only weakly dependent on cluster size. The concavity of the relative mobility versus solvent partial pressure curves also suggest that results can be fit and parameterized by a vapor molecule site-specific binding model. This model, (a Langmuir-adsorption based model) is described by Oberreit et al (D. R. Oberreit et al., 2015), and in it a cluster ion is assumed to have a maximum number (ζ_x) of sites to which a specific kind of solvent vapor molecules could bind. The activity coefficient a_x, defined as the ratio solvent vapor pressure at the surface of the cluster ion to the solvent saturation vapor pressure at a given temperature, is adjusted along with ζ_x to fit the data to the model. To perform the calculation, a unimolecular equilibrium sorption coefficient is defined as:

$$K'_{eq,g} = \frac{n_g}{n_{g-1}} \tag{4.1}$$

where n_g and n_{g-1} are the number of cluster ions with g and $g-1$ vapor molecules bound. If cluster ions quickly equilibrate with their surroundings once they enter the DMA, $K'_{eq,g}$ can be treated as a constant at a given saturation ratio S and can be calculated as:

$$K'_{eq,g} = \frac{S}{a_x}\left(\frac{\zeta_x+1}{g} - 1\right)\left(\frac{\mu_{v,g}}{\mu_{v,g-1}}\right)^{1/2}\left(\frac{\mathrm{PA}_{g-1}}{\mathrm{PA}_g}\right)\eta\left[\psi_{D,g-1}\right] \tag{4.2}$$

where PA_g is the projected area of the cluster ion with g vapor molecules bound to it, $\mu_{v,g}$ is the reduced mass of the sorbing vapor-cluster ion pair, $\eta\left[\psi_{D,g}\right]$ is an enhancement factor in vapor-cluster ion collision rate considering the interaction between the charge on the cluster ion and the dipole moments of the sorbing vapor molecule (defined in (D. R. Oberreit et al., 2015)). For simplicity, here, PA_g is estimated with the bulk material properties assuming the clusters are spherical. The probability that a cluster ion has g molecules attached to it is then calculated as:

$$P_g = \frac{n_g}{n_0 + \sum_{i=1}^{i=\infty} n_i} \tag{4.3}$$

With the equilibrium coefficients, P_g can be alternatively expressed as,

$$P_g = \frac{\prod_{j=1}^{g} K'_{eq,j}}{1 + \sum_{i=1}^{i=\infty} \prod_{j=1}^{j=i} K'_{eq,j}} \quad (g \geq 1) \tag{4.4a}$$

$$P_g = \frac{1}{1 + \sum_{i=1}^{i=\infty} \prod_{j=1}^{j=i} K'_{eq,j}} \quad (g = 0) \tag{4.4b}$$

the average mobility of the cluster ion at a specific saturation ratio of the solvent vapor can then be determined:

$$Z_{S,cal} = \sum_{g=0}^{g=\zeta_x} P_g Z_g \tag{4.5}$$

Given a combination of ζ_x and a_x, the calculated cluster ion mobilities $Z_{S,cal}$ are compared with the mobilities at different saturations ratios for selected ions. A weighted least square method with weights proportional to the partial pressure range that each data point represents is used to determine the most appropriate ζ_x and a_x values. Resultant fitting parameters for the sorption of butanol, ethanol, MEK and toluene molecules by both positively and negatively charged cluster ions $(NaCl)_xNa^+$ /$(NaCl)_xCl^-$ (x = 1, 4, 9 ,13) are listed in Table 4.1. Selected results of x =4 and x = 9 clusters are shown in Figure 4.6, with other fit results displayed in Figure C1 in Appendix C. For butanol, ethanol and MEK, the number of available sites on positively charged cluster ions increases with cluster size, as do the activity coefficients, with the exception of $(NaCl)_4Na^+$. For toluene, which shows little uptake by positively charged cluster ions, the activity coefficient is greater than 1, similar to Kelvin effect included in classical nucleation theory. For negatively charged cluster ions, the fit parameters do not scale with size, likely because of structural differences in different sized cluster ions, as evidenced in the results plotted in Figure 4.2 and Figure 4.4.

Table 4.1. The fitting parameters, determined for $(NaCl)_xNa^+$ (positive) and $(NaCl)_xCl^-$ (negative) clusters by comparing experiments to Equation (4.1-4.5) predictions.

Solvent Vapor	**Positive**			**Negative**		
	x	a_x	ζ_x	**x**	a_x	ζ_x
butanol	1	0.0358	8	1	0.476	9
	4	0.0392	12	4	2.50	42
	9	0.0606	18	9	1.67	48
	13	0.0794	20	13	0.0526	22
ethanol	1	8.03×10^{-3}	7	1	0.0478	6
	4	7.24×10^{-3}	9	4	0.200	20
	9	9.97×10^{-3}	13	9	0.714	49
	13	0.0163	17	13	0.036	10
MEK	1	1.02×10^{-4}	4	1	3.33	15
	4	1.77×10^{-3}	5	4	0.345	1
	9	2.45×10^{-3}	7	9	0.233	3
	13	2.92×10^{-3}	9	13	1.67	11
Toluene	1	5.00	24	1	0.286	1
	4	5.00	15	4	0.0787	1
	9	1.25	12	9	0.120	1
	13	3.33	24	13	0.0971	1

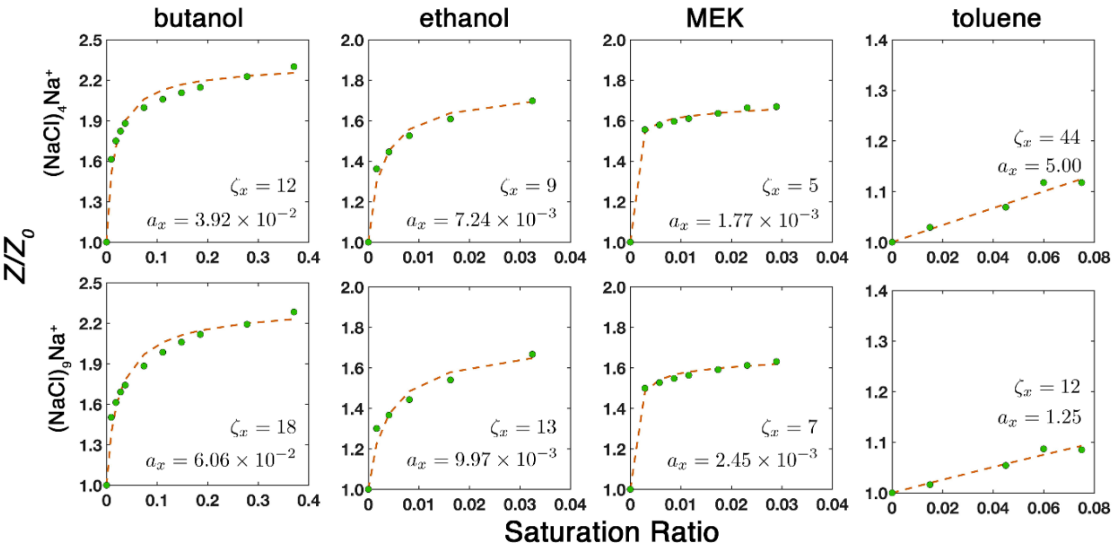

Figure 4.6. Langmuir model fitting for (NaCl)$_4$Na$^+$ and (NaCl)$_9$Na$^+$. ζ_x is the maximum number of available sites on the cluster ion surface; a_x is the activity coefficients of the solvent vapor when all the available sites are occupied by vapor molecules. Green dots are experimental data points and yellow dashed lines are fitting curves with the values of ζ_x and a_x displayed.

4.3.6 Sorption and Molecular Structure

For butanol and ethanol, it is observed that the inverse mobility of all cluster ions is a strong function of solvent partial pressure. Such a similarity is expected since butanol and ethanol have the same hydroxyl group at one end of their molecules, which should result in similar interaction between the vapor molecules and the cluster ions. The larger shifts of inverse mobility due to butanol sorption, however, do not necessarily indicate significantly more butanol molecules are attached to cluster ions, but rather a reflection of larger molecular size of butanol than that of ethanol. This is further supported by the Langmuir-model fitting; the total number of binding sites is similar for butanol and ethanol (1-5 more sites for butanol).

Meanwhile, MEK sorbs much more prevalently to positively charged cluster ions than to their negative counterparts in the pressure range considered. We speculate that such charge polarity discrimination could arise from electrostatic interactions between the cluster ions and MEK molecules. The carbonyl group in MEK molecules has a negative partial charge on the oxygen atom, which could facilitate adsorption by positively charged cluster ions. However, the positive partial charge on the carbon atom (in C=O) is less pronounced, as this net charge is distributed to neighboring carbon ions.

Unlike the other three solvents that contain strongly polar functional groups, toluene has less pronounced effect on cluster ion mobilities for all charge states. We speculate this is due to the lack of polar functional groups in toluene. It is also possible that the smaller dipole moment of toluene (0.36 D) compared to the other solvent vapor (butanol~1.66 D, ethanol ~1.69 D, MEK~2.76 D) could cause such differences in sorption. To ascertain if this is the case, we conducted experiments with chlorobutane as solvent vapor. Chlorobutane has a larger dipole moment (1.90 D) than both butanol and ethanol and should therefore be readily adsorbed by cluster ions if the dipole moment plays a central role. However, chlorobutane vapor induces inverse mobility shift less than 10% for all the cluster ions within the pressure range *0*-300 Pa (as shown in Figure C2 in Appendix C), suggesting that it is not simply dipole moment that governs sorption.

4.4 Conclusions

We used a differential mobility analyzer-mass spectrometry to investigate organic vapor uptake by nanometer scale particles, i.e. sodium chloride cluster ions. Results for four solvent vapors (butanol, ethanol, MEK and toluene) are displayed and were compared. Based on this study, we make the following concluding remarks:

1. Overwhelmingly, cluster ion charge polarity and the molecular structures of the vapor molecules are found to control the extent of vapor uptake, in qualitative agreement with previous CPC activation efficiency studies which strong chemical composition and charge polarity influences. All tested vapors appear to sorb to ions when present at partial pressure of 10^2 Pa, irrespective of their saturation vapor pressure. Cluster size is found to have a much smaller influence on uptake facilitated inverse mobility shift (when normalized by the dry inverse mobility) than vapor molecular structure and ion polarity.
2. While cluster "size" does not appear to strongly influence vapor sorption, cluster structure appears to have a pronounced influence. In particular, for $(NaCl)_xCl^-$ x =7, 8, 9 group (among others), under dry conditions the measured inverse mobility does not scale with cluster mass, suggesting that clusters differing by one cation-anion pair have disparate structures from one another. For these clusters we also find unique extents of uptake.
3. Taking (1) and (2) into account, our measurement suggest that the earliest of uptake are not dependent purely on cluster "size", rather electrostatic interactions and molecular/cluster structure govern vapor sorption. We suggest that in the future design of condensers and condensation particle counters for the 1 nm size range, that activation efficiencies (which hinge upon particles/clusters first sorbing vapor) the activation efficiency not be reported solely as a function of mobility equivalent size, but should be examined for a variety of clusters with

variable structures. It is unlikely that any single cluster type can serve as surrogate for all clusters/particles of interest in different environments.

4. The vapor-scavenging behavior observed in this work by cluster ions, even at the ~100 parts per million vapor concentration level implies that the presence of solvent vapor will influence ion properties in most environments, which has implications not only growth on ions but also in the application of ions in charging pre-existing particles. Specifically, trace amounts of vapors might have an impact on the stationary charge distribution attained of aerosol neutralizers, as has been observed experimentally (Steiner & Reischl, 2012). This may be particularly problematic in studies where particles are aerosolized via organic solvent sprays and residue solvent in the vapor phase is likely.

Chapter 5: Mass, Momentum, and Energy Transfer in Supersonic Aerosol Deposition Processes

Abstract: Aerosol deposition (AD) has emerged as a novel additive manufacturing (AM) method for surface coating and thin film production. In contrast to cold spray, AD does not require pressurized gas, works at room temperature and is frequently used to deposit sub-micron particles. It is generally acknowledged that the instantaneous particle speed upon impaction is critical to controlling coating/film properties such as porosity, and mitigating particle bounce during deposition. Therefore, converging-diverging nozzles are often employed in AD to accelerate particles to the desirable impaction speed. In this work, we simulated flow field profiles as well as particle trajectories for typical AD working conditions for a slit type converging-diverging nozzle. In examining the flow filed profile, we show that the velocity, pressure profile as well as shock structure are sensitive to the upstream and downstream operating pressures of the nozzle, which in turn affects particle impaction speed. To aid particle trajectory simulations, we trained a neural network to predict drag force on the particles based on existing experimental data, theoretical limits and simulation results obtained by direct simulation of Monte Carlos (DSMC). The neural network based drag law shows better agreement with the DSMC simulation data. Particle trajectory simulation results reveal that for a given particle density, there exists an optimal particle diameter to maximize particle impaction speed, as well as a diameter to maximize particle initial focusing, though these two diameters are typically not equal. We developed a framework that can be

used to evaluate the position-dependent mass, momentum and kinetic energy flux to the deposition substrate for any aerosol size distribution upstream the nozzle. It is shown for typical aerosol concentrations achievable in laboratory, the kinetic energy flux can approach a magnitude normally observed in convective heat transfer with phase change due to particle inertial focusing.

5.1 Introduction

Aerosol deposition (AD) has emerged as an additive manufacturing method for coating and thin film production (Akedo, 2006, 2008; Hanft et al., 2015; C. Huang et al., 2007; M. W. Lee et al., 2011; Park et al., 2014; Park et al., 2017). Distinct from other particle deposition methods, such as thermal and cold spray (Stoltenhoff, Kreye, & Richter, 2002; Yin, Meyer, Li, Liao, & Lupoi, 2016), AD can function at room temperature and does not require highly pressurized gas (Adachi, Okuyama, Kousaka, & Tanaka, 1988; Hanft et al., 2015); this facilitates deposition onto low-melting point materials with simpler manufacturing devices. The AD process involves accelerating particles with a compressible, high-speed carrier gas, leading to particle impaction at supersonic speeds and reduced pressure, with the potential for both particle heating as well as plastic deformation upon collision with the substrate (while the substrate itself is relatively undisturbed). It is generally acknowledged that high particle speed during impaction is critical to control coating/film properties such as porosity, and to mitigate particle bounce upon deposition (Hamid Assadi, Gärtner, Stoltenhoff, & Kreye, 2003; Yin et al., 2016). To this end, converging-diverging nozzles (i.e. de Laval nozzles) are frequently used, as such nozzles enable the acceleration of flow and of particles to supersonic speeds within the nozzles themselves.

Though considerable effort has been devoted to simulation of particle trajectories within converging-diverging nozzles and to estimate impaction speeds in particle deposition systems (Abouali & Ahmadi, 2005; C. Huang et al., 2007; Katanoda, Fukuhara, & Iino, 2007; M.-W. Lee et al., 2011), many critical aspects the AD process remain uninvestigated. First, the drag force of the carrier gas on particles needs to be carefully considered in designing AD systems. As particles traverse through the nozzle, rapid gas rarefication and densification (due to shock formation) can lead to particle Knudsen number (Kn) variations by as much as $\sim 10^2$, hence the drag regime rapidly varies between the ballistic/free molecular and continuum limits. In addition, due to gas stagnation close to the substrate or insufficient particle acceleration, particle Mach numbers (Ma, based on relative speed of gas and particles) can exceed unity, with potential shock formation close to the particle surface (Fernández de la Mora, Rao, & McMurry, 1990). Modeling of particle trajectories, therefore, requires a drag law that is valid for a wide range of Kn and Ma. To date, many models of the AD process do not appropriately consider the Knudsen and Mach number evolution for particles (C. Huang et al., 2007; G. Huang, Gu, Li, Xing, & Wang, 2014; Johnson, Schwer, Park, Park, & Gorzkowski, 2017), and for those where this is considered (Ning, Wang, Ma, & Kim, 2010), the most widely used particle drag correlation is that proposed by Henderson (Henderson, 1976). The basis dataset for Henderson’s correlation is unfortunately incomplete; in particular, it does not span the Kn and Ma number ranges critical to AD systems operating at reduced pressure. For example, submicrometer particles typically lie within the transition regime (0.1<Kn<10), and can have Mach numbers between 0 and 3 during deposition; however, a large fraction of the data utilized in Henderson's correlation in this Kn range were collected at extremely low Mach number, i.e. $\mathrm{Ma} \in (5 \times 10^{-7}, 6 \times 10^{-6})$, and there are few data points with Kn of order 10^{-1} and Ma > 1 (Bailey & Hiatt, 1971) .

Another aspect to be explored in AD relates to how operating conditions of the nozzle influences particle impaction speed. Relevant factors, such as gas temperature and composition, substrate position and particle size, have been examined closely for cold spray process (Champagne, Helfritch, Dinavahi, & Leyman, 2011; Katanoda et al., 2007; M.-W. Lee et al., 2011; Yin et al., 2016), wherein the upstream pressures are typically on the order of 10^6 Pa, the downstream pressure is atmospheric pressure, and the particles are tens of micrometers in diameter. The AD process, conversely, is characterized by atmospheric upstream pressure and reduced downstream pressure, and has significantly larger gas rarefaction effects. Because of low downstream pressures AD has the potential for application with submicrometer and nano-sized (<100nm) particles (Adachi et al., 1988; Fernández de la Mora et al., 1990; Rao et al., 1998), though this is not commonly considered in AD design.

A final concern regarding the AD process is the influence of the input particle size distribution function on linewidth/mass deposition profile, as well as momentum and energy fluxes to the substrate. Ultimately, aerosol deposition is an inertial process. Inertial motion of particles is not only known to be highly particle size dependent, but also leads to lateral focusing of particles (de Juan & Fernandez de la Mora, 1998; X. L. Wang, Kruis, & McMurry, 2005), i.e. the depositing particle linewidths will be highly particle size specific, and there will be an optimally focused particle size which has the minimal deposition linewidth. Such focusing effects, coupled with polydisperse size distributions, dramatically impact the mass, momentum, and energy flux distributions over the substrate area, though this has not been described previously.

Here, we apply a combined computational fluid dynamics-particle trajectory model to better examine particle mass, momentum, and energy transfer to substrates in aerosol deposition. Specifically, in our modeling we examine a slit shaped converging-diverging nozzle under conditions applicable to AD. Particle trajectories are simulated using drag coefficients derived from a neural network (to correct the drag coefficient relationship) incorporating new direct simulation Monte Carlo data to compute particle drag coefficients for Ma $\in (0, 5)$ over a wide Kn number range. Particle trajectories and spatial distributions at impaction are examined varying particle size and density. Finally, mass, momentum, and energy flux distribution equations are developed and applied to examine how the spatial distribution of depositing particles affects the overall mass deposition rate, particle momentum flux, and impinging particle kinetic energy flux.

5.2 Computational Methods

5.2.1 Nozzle Geometry and Simulation Domain

The nozzle geometry used in this study is shown in Figure 5.1. The nozzle is a slit-shaped, converging-diverging de Laval nozzle, which would be suitable for deposition of coatings via rastering of the substrate.(Hanft et al., 2015) It has an inlet width of 4.4 mm and an outlet width of 2 mm, as well as a throat width of 0.2 mm. The converging section of the nozzle has a length of 2.5 cm, while the diverging section is 3.5

cm. A 20 mm width, flat substrate is placed 6 mm below the nozzle outlet; the chamber housing the substrate is 44 mm in width.

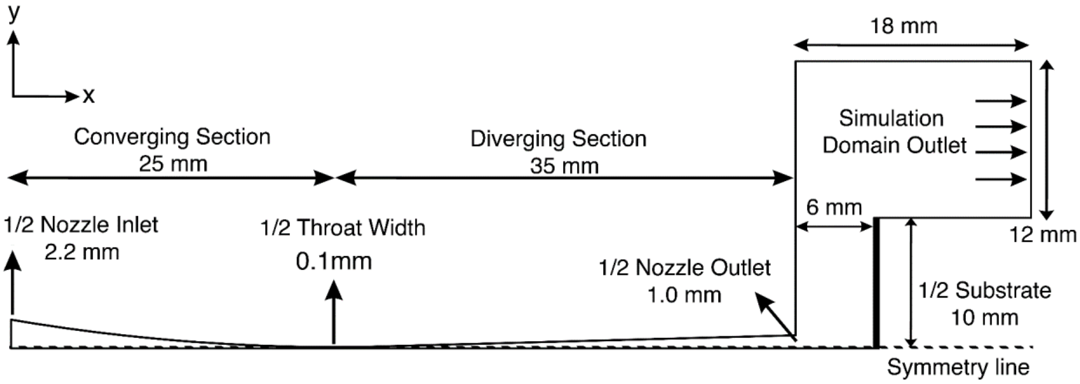

Figure 5.1. Nozzle geometry and simulation domain.

5.2.2 Computational Fluid Dynamics Simulation

We employed finite volume simulations using ANSYS Fluent 18, solving the two dimensional compressible Navier-Stokes equations to obtain the fluid flow profile under steady conditions coupled with solution to the energy equation. We elected to use two-dimensional simulations in consideration of the high nozzle cross section aspect ratio (near 10^2) commonly utilized in AD with slit-type nozzles; in this instance two-dimensional simulation should provide reasonable accuracy in a more computationally efficient manner than a fully three-dimensional model. A turbulence model was employed because at the nozzle throat, the hydraulic diameter based Reynolds number is ~5×10^3 with atmospheric pressure upstream, hence a modest degree of turbulence may arise in the flow. Prior work has shown that the SST $k-\omega$ turbulence model (Menter, 1994) is accurate in simulating compressible flows in converging-diverging nozzles

(Balabel, Hegab, Nasr, & El-Behery, 2011); thus, we chose this model to account for turbulent dissipation in flow-profile simulations. The governing equations for continuity, momentum transfer, and energy using this model are provided in (Ding, Wang, & Wang, 2017; Fluent, 2009) and noted in the Appendix E.

It is important in AD fluid flow simulations to have a sufficiently high node density near the substrate to resolve the shock structure at the substrate surface. A grid independence study was carried out to determine the number of grid points required to fully resolve the flow profile. In this study, we simulated half of the nozzle geometry (because of symmetry conditions) with 1.0×10^6, 1.6×10^6, and 3.0×10^6 nodes. We observed negligible difference in simulation velocity and pressure fields between these three simulations, indicating all were appropriate in modeling the flow and pressure fields. In all simulations the gas modeled was nitrogen (N_2); its viscosity varied with temperature in accordance with the Sutherland equation, as noted in Appendix G. The boundary conditions were set as follows: (1) the no-slip condition was invoked at all solid walls and the substrate, and all solid boundaries were treated as adiabatic; (2) the inlet temperature was set to 300K, at a stagnation pressure of either 190 or 760 Torr; and (3) the outlet static pressure (at the boundaries, Figure 5.1) was set to either 1 Torr or 10 Torr. At the inlet the flow direction was set to be normal to the boundary and the turbulence intensity was set to be 1% (low turbulence). Simulations were run until the scaled residual reached the following criteria, which are commonplace in ANSYS Fluent simulations (Fluent, 2009): continuity$< 1\times10^{-5}$, x-velocity$< 1\times10^{-5}$, y-velocity$< 1\times10^{-5}$, energy $\leq 1\times10^{-5}$, $k < 5\times10^{-5}$, and $\omega < 1\times10^{-6}$. The difference between inlet and outlet mass flow rates were checked as another criterion for convergence: for all cases examined, the flowrate differences were less 0.1%.

5.2.3 Particle Trajectory Simulations

We assumed one way coupling between the fluid and the particles, i.e. the presence of particles was assumed to have negligible effect on the flow profile. To estimate particle impaction velocity and flux distribution to the substrate, particles of prescribed diameter and density were released uniformly along the inlet boundary of the nozzle. The examined particle diameters range from 3 nm to 10 μm, and two densities were selected: 2650 kg m^{-3} and 8960 kg m^{-3}, which correspond to silica and copper, respectively. Particle Brownian (thermal) motion was not considered as this effect is expected to be small relative to the influences of flow and inertia. (Lindquist, Pui, & Hogan Jr, 2014) Additionally, as shown in the Results & Discussion section, for the simulated flow conditions, only particles > 15 nm impact upon the substrate (for copper), for which Brownian motion would certainly minimally impact trajectories.

For trajectory calculations, user-defined functions were incorporated in Fluent's discrete phase model (DPM). At each time step, the gas properties (specifically the velocity vector, the temperature, and the pressure) were sampled from the cell in which a particle was located. These properties were then used to compute the drag force on the particles using user defined drag laws. The equation of motion for a particle is expressed as:

$$\rho_p \frac{\pi}{6} d_p^3 \frac{d\overrightarrow{v_r}}{dt} = -\frac{1}{2} \rho_g \|\overrightarrow{v_r}\|^2 A_p C_d \frac{\overrightarrow{v_r}}{\|\overrightarrow{v_r}\|} \tag{5.1}$$

where $\overrightarrow{v_r}$ is the relative velocity vector between the particle and fluid, ρ_p is the particle density, d_p is the particle diameter, ρ_g is the gas density, A_p is the particle cross sectional area, and C_d is the drag coefficient. Correlations have been developed for C_d in different Mach number and Knudsen number regimes. We review selected regimes here, showing that until recently, there were limited results in the Ma and Kn ranges of interest for AD. In the limit of particle Mach number $Ma \rightarrow 0$, the Cunningham correction factor is used to modify Stokes's law to account for the rarefaction effect. $C_{d,C}$, is given by (Davies, 1945):

$$C_{d,C} = \frac{24}{Re}\left(1 + 2Kn\left[1.257 + 0.4\exp(-\frac{0.55}{Kn})\right]\right)^{-1} \tag{5.2}$$

where the subscript "C" denotes it is Cunningham's correlation, and $Re = \frac{\rho_g \|\overrightarrow{v_r}\| d_p}{\mu}$ and $Kn = \frac{\lambda}{d_p}$ are particle Reynolds and Knudsen number, respectively (μ is the gas dynamic viscosity and λ is the gas hard sphere mean free path, calculated as noted in Appendix G). We note that this definition of Kn, used throughout this manuscript, is is in agreement with some of the previous work on particle drag with direct simulation Monte Carlo(Singh & Schwartzentruber, 2017) (Macrossan, 2006), but is distinct from the commonly used definition normalizing by particle radius (C. L. Zhang, Thajudeen, Larriba, Schwartzentruber, & Hogan, 2012) and common equations have been adjusted accordingly. For particles in the free molecular regime ($Kn \rightarrow \infty$), assuming all gas molecules are reflected diffusely after colliding with the particle surface, an analytical expression for C_d was derived by Patterson (Patterson, 1971):

$$C_{d,P} = \frac{2}{S^3}\left[\frac{2S^2+1}{2\sqrt{\pi}}\exp(-S^2) + \left(\frac{4S^4+4S^2-1}{4S}\right)\operatorname{erf}(S)\right] + \frac{2\sqrt{\pi}}{3S}\left(\frac{T_p}{T_\infty}\right)^{\frac{1}{2}} \tag{5.3}$$

where the subscript “P” denotes Patterson’s equation (derived), $S = Ma\sqrt{\frac{\gamma}{2}}$, γ is the heat capacity ratio of the gas, and T_p and T_∞ are the particle and the free stream temperature, respectivley. Equation (5.3) applies at all Mach numbers (and hence all values of S) in the free molecular limit.

Equations (5.2) and (5.3) give the drag coefficients only in limiting cases, unfortunately. Based on theoretical results (Stalder & Zurick, 1951) as well as experimental data (Bailey & Hiatt, 1971; Goldstein, 1938; Millikan, 1923), Henderson (Henderson, 1976) derived a correlation that is applicable to particle Reynolds numbers up to the critical Reynolds number (for formation of a turbulent boundary layer) and all Mach numbers. The Knudsen number is a better indication of gas rarefaction effects, with the relationship of Re, Kn and Ma for a spherical particle given by the equation:

$$Kn = \frac{Ma}{Re}\sqrt{\frac{\gamma\pi}{2}} \tag{5.4}$$

Henderson’s correlation can be rewritten in terms of Ma and Kn:

for $Ma \leq 1$

$$C_{d,H} = 24\left[1.77\frac{S}{Kn} + S\left\{4.33 + \left(\frac{3.65-1.53\frac{T_p}{T_\infty}}{1+0.353\frac{T_p}{T_\infty}}\right) \times \exp\left(-\frac{0.438}{Kn}\right)\right\}\right]^{-1} + \exp\left(-0.447\sqrt{\frac{Ma \cdot Kn}{\gamma^{0.5}}}\right) \times \left[\frac{4.5Kn+0.38\left(0.053S+0.639\sqrt{Kn \cdot S}\right)}{Kn+0.053S+0.639\sqrt{Kn \cdot S}} + 0.1Ma^2 + 0.2Ma^8\right] + 0.6S \cdot \left[1 - \exp\left(-0.798\frac{Kn}{\gamma^{0.5}}\right)\right] \tag{5.5}$$

for $Ma \geq 1.75$

$$C_{d,H} = \frac{0.9+\frac{0.34}{Ma^2}+1.661\frac{Kn^{0.5}}{\gamma^{0.25}}\left[2+\frac{2}{S^2}+\frac{1.058}{S^2}\left(\frac{T_p}{T_\infty}\right)^{0.5}-\frac{1}{S^4}\right]}{1+1.661\frac{Kn^{0.5}}{\gamma^{0.25}}} \tag{5.6}$$

for $1 \leq Ma \leq 1.75$

$$C_{d,H}(Ma, Kn) = C_d(1.0, Kn) + \frac{4}{3}(Ma - 1)[C_d(1.75, Kn) - C_d(1.0, Kn)] \quad (5.7)$$

where the subscript "H" denotes Henderson's correlation. However, Henderson's data set is incomplete for particles in the slip and transition regime for compressible flow, and the accuracy of the correlation in this regime had not been evaluated. In light of this, we compared Henderson's correlation with simulation results obtained by DSMC (direct simulation of Monte Carlo) (Boyd & Schwartzentruber, 2017) under isothermal conditions (identical particle and free stream gas temperature), considering a uniform flow of nitrogen gas upstream of a particle (which was immobile) at specified Knudsen number and Mach number. Details on the DSMC approach are provided in Zhang & Schwartzentruber (C. Zhang & Schwartzentruber, 2012) as well as Singh & Schwartzentruber. (Singh & Schwartzentruber, 2017) We find that drag coefficients predicted by Henderson's correlation deviate as much as 30% from the simulated values in the transition regime (see Figure F1 in Appendix F). A new correlation, based on neural network, is proposed for $10^{-4} < Kn < \infty$ and $0 < Ma < 5$:

$$C_d = C_{ic}(Kn, Ma) \cdot (\boldsymbol{W_2} \tanh(\boldsymbol{W_1 X} + \boldsymbol{b_1}) + b_2) \quad (5.8)$$

$$C_{ic} = \frac{24}{\frac{Ma}{Kn}\sqrt{\frac{\gamma\pi}{2}}\left[1+2Kn(1.257+0.4\exp\left(-\frac{0.55}{Kn}\right))\right]} +$$

$$\exp\left(-0.447\sqrt{\frac{Ma \cdot Kn}{\gamma^{0.5}}}\right) \times \left[\frac{4.5Kn+0.38\left(0.053S+0.639\sqrt{Kn \cdot S}\right)}{Kn+0.053S+0.639\sqrt{Kn \cdot S}}\right] \quad (5.9)$$

where $\boldsymbol{W_1}$, $\boldsymbol{W_2}$, $\boldsymbol{b_1}$, b_2 are weights and biases of the network, and C_{ic} is a fit to drag coefficient for $Ma \rightarrow 0$, and X is the input into the neural network with the form $\boldsymbol{X} = \begin{bmatrix} Ma \\ \min(log_{10}Kn, 1) \end{bmatrix}$. A more detailed description of the correlation is provided in Appendix F (along with Figure F2, providing a plot of Equation (5.8)). For AD, the particles of interest lie in the regime of $10^{-4} < Kn < \infty$ and $0 < Ma < 5$. In light of this, the particle drag coefficients are calculated with Equation (5.8) and (5.9) throughout this work.

5.3 Results & Discussion

In total, we simulate the velocity and pressure fields for a de Laval-type AD system and examine particle trajectories in the 3 nm – 10 μm range using drag coefficients determined for conditions relevant to AD. We first present results of flow field simulations, following by evaluation of the impaction velocities for particles of two different densities (under all three flow conditions). Finally, using copper particles as a model we examine the deposition distribution functions (over the substrate area) and calculate location dependent mass fluxes, momentum fluxes and energy fluxes for model particle size distribution functions.

5.3.1 Simulation results of flow properties

Though most AD systems function with atmospheric pressure upstream (Akedo, 2006; Akedo & Lebedev, 1999; Muneyasu, Tetsuo, & Jun, 2017), variable pressure is worthy of examination as it is possible to optimize the particle deposition process by varying upstream and downstream pressures (Holman & Kortshagen, 2010; Thimsen et al., 2014). In addition, the variability of flow properties brought about by operating conditions provides useful information in the optimization of nozzle design. The simulated operating conditions are summarized in Table 5.1, along with flow properties calculated by the isentropic, one-dimensional nozzle theory (Saad, 1985) for comparison.

Figures 5.2a-5.2c show the contour plots of gas speed for three different cases; correspondingly, gas pressure, density and velocity along the nozzle symmetry line are plotted in Figures 5.2d-5.2f as functions of distance to the nozzle inlet. For case 1 (760 Torr upstream pressure, 10 Torr downstream pressure), Figure 5.2a indicates that the gas is fully expanded within the nozzle and goes through a minimal amount of expansion after exiting the nozzle. This in contrast to isentropic theory for de Laval nozzles (Saad, 1985), which predicts that outlet to throat area ratio of 10 requires the upstream/downstream pressure ratio to be ~150 to fully expand the gas. Instead, due to the formation of a boundary layer, the 'effective' outlet area is reduced and a pressure ratio of 76 results in nearly full expansion. We remark that depending on the degree of turbulence in the boundary layer and the turbulence model used in simulations, the effective outlet area may change slightly. This in turn may change the magnitude of pressure and velocity fields, but all trends discussed here would not be affected by model choice.

Table 5.1. A summary of the three simulation cases examined and a comparison with isentropic nozzle theory.

Case No.	**Upstream pressure**	**Downstream pressure**	**Velocity at exit center (isentropic)**	**Velocity at exit center (simulation)**	**Pressure at exit center (isentropic)**	**Pressure at exit center (simulation)**
1	760 Torr	10 Torr	Shock inside nozzle	596 m/s	Shock inside nozzle	14.36 Torr
2	760 Torr	1 Torr	685 m/s	596 m/s	5.32 Torr	14.36 Torr
3	190 Torr	1 Torr	685 m/s	491 m/s	1.33 Torr	4.50 Torr

Figure 5.2b shows that if the downstream pressure of the nozzle is reduced to 1 Torr, the gas exiting the nozzle is underexpanded and goes through further expansion

after exiting the nozzle. However, comparison of the green and orange curves in Figures 5.2d and 5.2e reveals gas properties within the nozzle are exactly the same along the symmetry line for the downstream pressures of 1 Torr and 10 Torr. This is in accordance with supersonic flow theory; gas travelling supersonically prevents downstream conditions from affecting flow inside the nozzle.

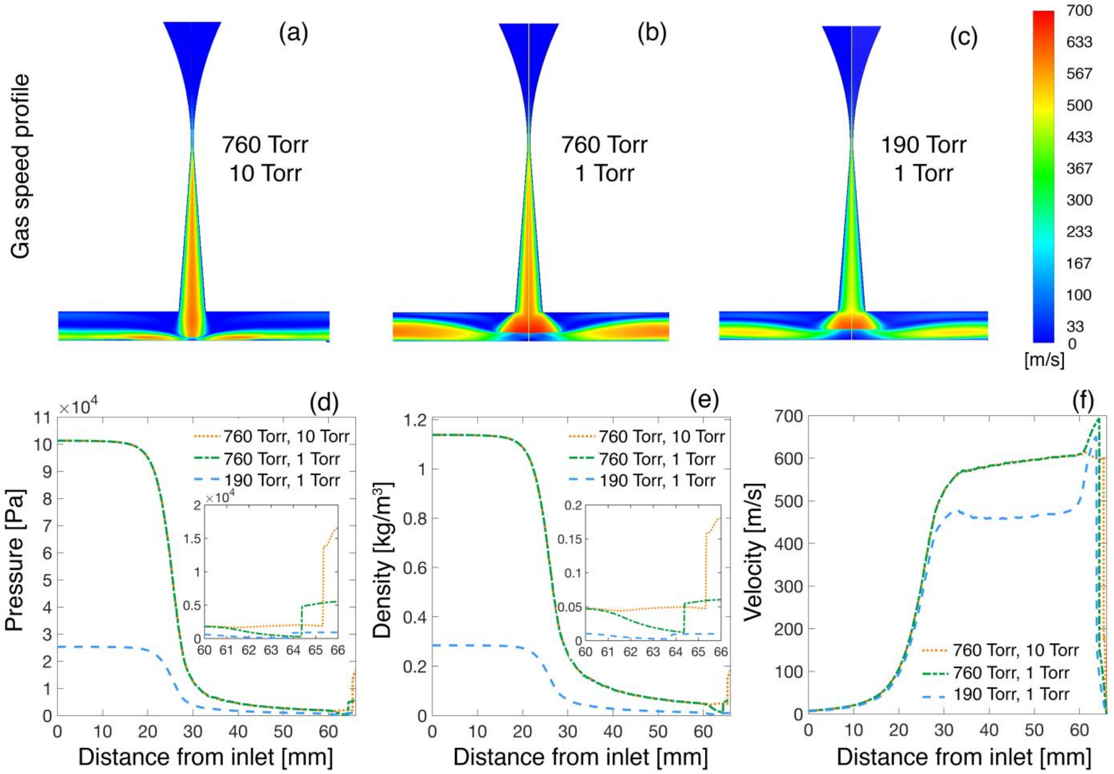

Figure 5.2. Fluid flow simulation results for the 3 examined cases. In (a-c), contour plots of gas speed are shown for different operating pressures of the nozzle: (a) 760 Torr at the inlet, 10 Torr at the outlet; (b) 760 Torr at the inlet, 1 Torr at the outlet; (c) 190 Torr at the inlet, 1 Torr at the outlet. In contour plots, the dimension of the nozzle along the symmetry line has been scaled down by a factor of 2.85 and the simulation domain beyond substrate is not displayed. Gas pressures, densities and velocities along the nozzle symmetry line are shown in (d), (e) and (f), respectively.

For case 3, Figure 5.2c reveals that as the upstream pressure is reduced, the flow speed within the nozzle is also reduced. This is in contradiction to the isentropic theory (c.f. Table 5.1), but is again attributable to viscous effects in the flow. The gas viscosity is independent of pressure, hence reducing the upstream pressure from 760 Torr to 190 Torr does not result in a decrease of viscous effects given the same velocity gradient. Therefore, a higher fraction of the pressure head must act to compensate for viscous effects in case 3 than in the higher upstream pressure cases; this results in a less accelerated gas. Additional pressure and temperature contour plots are shown for case 1 in Figure H1in Appendix H; qualitatively similar plots are obtained for other cases.

Figure 5.2 also provides useful information regarding the post-shock region, i.e. the region close to the substrate, as well as how operating pressures affect gas properties within this region. As the gas traverses through the shock, its properties change drastically, which is clearly evident in Figures 5.2d-5.2f. With static pressure as an example, changing the downstream pressure from 10 Torr to 1 Torr decreases the pressure in post-shock region from ~113 Torr to ~37 Torr. Simultaneously, the thickness of the post shock region (distance between the shock and the substrate) changes from ~0.68 mm to ~1.65 mm. Reducing the upstream operation pressure from 760 Torr to 190 Torr has a similar effect. The pressure in the post-shock region changes from ~37 Torr to ~6.75 Torr, and the thickness of the post-shock region increases form ~1.65mm to 2.25 mm. These results highlight the need for a drag coefficient correlation that is accurate over the wide range of particle Knudsen numbers and relative gas-particle Mach numbers caused by nozzle expansion and compression near the substrate. Figure H2 shows selected plots of particle Knudsen and Mach numbers (expressed as the relative particle velocity to speed of sound ratio) along the center line for case 1 (copper particles). With the exception of the largest particles examined (10 μm and larger), the Mach number is smaller than unity for particles until they approach the shock; however, for smaller particles, as they enter the shock the Mach number exceeds 1.0. Particle Knudsen numbers span more than one order of magnitude (for a given particle diameter) as they traverse the nozzle. The smallest particles examined reach Knudsen numbers above 10^1, while the Knudsen numbers of the largest particles remain below 10^{-1}. The effects of this unique Kn, Ma range on particle deposition are discussed in the next section.

5.3.2 Particle Impaction Simulation Results

Particle impaction speed at the substrate surface is of critical importance in the AD processes; it appears to be directly related to particle adhesion, plastic deformation, and is likely the key parameter governing the resulting coating/film properties in AD (Akedo, 2006; Champagne et al., 2011; Hanft et al., 2015). For trajectory calculations, utilizing the simulated flow fields, 100 particles of prescribed size and density were released with their initial positions equally spaced along the nozzle inlet. The velocities and positions of the particles were recorded until they were either trapped by a wall or they escaped the simulation domain.

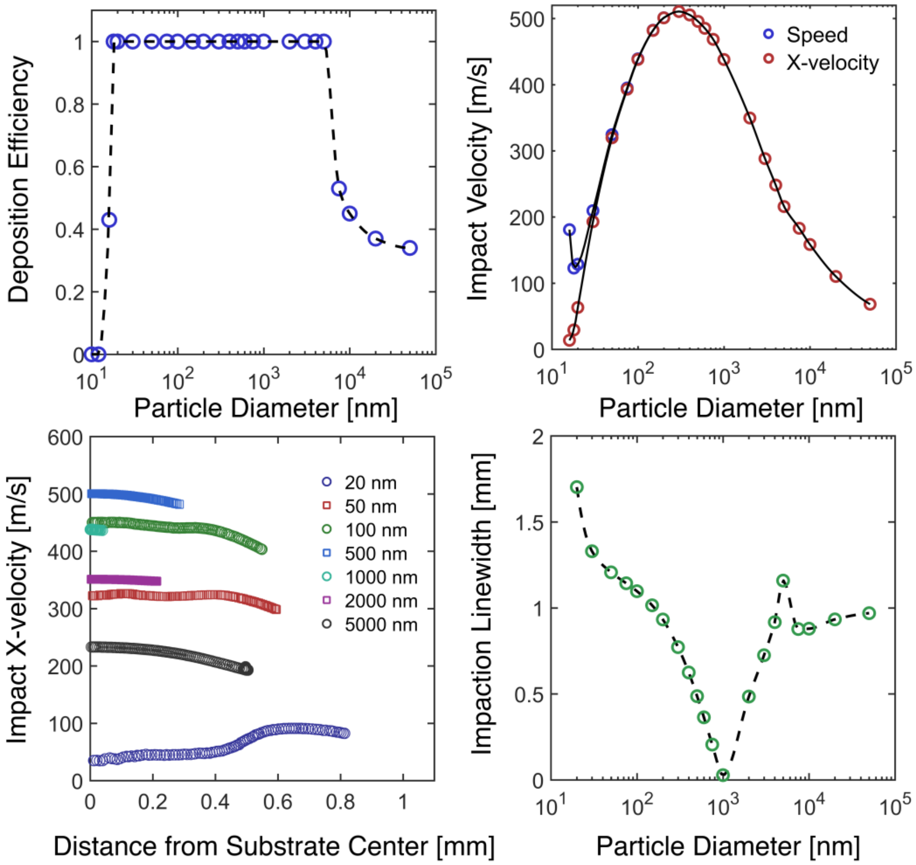

Figure 5.3. Particle trajectory simulation results for copper particles for case 1. **(a)** The particle impaction efficiency as a function of particle diameter. **(b)** Average particle impact speed and x-velocity (i.e. perpendicular to the substrate) as a function of particle diameter. **(c)** Impact x-velocity and impact position for different particles diameters. **(d)** Particle impaction linewidth for different diameter. Particle impaction linewidth is defined as four times the average distance of particle impaction point from the center of the substrate.

We first present particle trajectory results in detail for copper particles traversing the flow field of case 1 (760 Torr upstream pressure, 10 Torr downstream pressure), with results summarized in Figures 5.3a-5.3d. Specifically, Figure 5.3a shows the deposition efficiency (defined as the fraction of particles impacting upon the substrate) as a function of particle diameter. Both small particles ($d_p < 16nm$) and large particles ($d_p > 5\mu m$)

have low impaction efficiencies while particles intermediate to these diameters impact with perfect efficiency. For small particles, the drag force on particles is high compared to particle inertia, as a result, sufficiently small particles tend to follow gas stream lines in the post-shock region and escape the simulation domain (this phenomenon is observed in all particle inertial separation systems (Fernandez de la Mora, Hering, Rao, & McMurry, 1990; Marple & Willeke, 1976)). Conversely, particles larger than $5\mu m$ do not leave the simulation domain, but as a result of high inertia compared to drag force they cross the nozzle symmetry line at the throat and collide with the nozzle wall on the side opposite to their release point. Sample particle trajectories are provided in Figure H3. Figure 5.3b shows average particle impact velocity along with its x-component for different particle diameters. The average particle impaction velocity initially increases with particle diameter and then decreases with it, with a maximum impact speed for ~300 nm diameter particles. To our knowledge, this is first direct calculation revealing that particles of highest impaction speed in AD can be in the submicrometer size range, as most work has focused on supermicrometer particles. As particles traverse through the nozzle, they are first accelerated by the carrier gas and are then decelerated by stagnated gas in the post-shock region, just prior to impaction. Though particles of small sizes tend to be fully accelerated in the nozzle, they are decelerated significantly in the post-shock region, where the gas has an x-velocity approaching 0 (refer to Figure 5.2f). In contrast, sufficiently large particles are less affected by the post-shock region, but are not fully accelerated inside the nozzle. The net result of the acceleration-deceleration process is an optimal particle size that has the highest impact velocity. This phenomenon has been reported in simulations of cold spray (H. Assadi et al., 2011), though maximum deposition speed was found for significantly larger particles; this is because in high pressure cold spray, the effects of the post-shock are most pronounced but larger particles are better accelerated upstream (i.e. the drag coefficient is larger in cold spray). We can therefore conclude that the existence of an optimum in particle diameter for the impact speed is universal in nozzle based deposition systems, though the particle diameter impacting with highest speed is adjustable by adjusting upstream and downstream pressures.

Figure 5.3c shows the lateral position r (i.e. distance between the substrate center and the particle impaction point) and the x-velocity for each deposited particle at selected particle diameters. For $d_p = 20\ nm$, the particle impact positions are relatively dispersed in r. As particle diameter increases, the dispersity of particle impact positions decreases substantially, reaching a minimum at $d_p = 1\ \mu m$. This is attributable to inertial focusing of particles.(de Juan & Fernandez de la Mora, 1998; X. L. Wang et al., 2005) Inertial focusing occurs when particles are first directed towards the substrate center in the converging section the nozzle, but, because of their inertia, they are not sufficiently accelerated laterally outward in the diverging section. Focused particles hence deposit close to the substrate center, independent of their initial position. For the examined nozzle and flow conditions at diameters below 1 μm, the particles are underfocused, hence the deposition linewidth increases with decreasing particle diameter. Beyond a diameter of 1 μm particles are overfocused; overfocusing occurs when particles are inertially directed across the symmetry axis of the nozzle in the converging section. An alternative representation of focusing is shown in Figure 5.3d, which is a plot of the impaction linewidth as a function of particle diameter. Impaction linewidth is defined as

4 times the average impact position (accounting for the symmetry condition). Evidenced in the figure, an optimal diameter ($1\ \mu m$) for particle focusing exists and the nozzle functions as an aerodynamic lens (X. L. Wang et al., 2005). We note that for $d_p > 5\ \mu m$, the impaction width is approximately 0.8 mm. For these particle diameters the impaction efficiencies are less than 100%, and the impaction linewidth only reflects the dispersity of transmitted particles (i.e. the linewidth is reduced due to particle loss upstream). While focusing is a known phenomenon, commonly used in concentrating aerosol particles for chemical analysis (Jayne et al., 2000; Liu, Ziemann, Kittelson, & McMurry, 1995; Mallina, Wexler, Rhoads, & Johnston, 2000; Middha & Wexler, 2003), it has not been examined closely in either cold spray or aerosol deposition. However, our results indicate that the focusing effect is pronounced in AD with converging-diverging nozzles, and although the optimally focused diameter of $1\ \mu m$ is system specific, a maximally focused diameter will exist in all gas phase particle inertial deposition systems (similarly, smaller particles will be underfocused and sufficiently large particles will be overfocused). Through focusing, the input particle size distribution in any deposition system has a strong influence on the overall linewidth, as well as the momentum and kinetic energy flux distributions to the substrate. We examine these effects subsequently using test polydisperse particle size distribution functions. We also remark that focusing would be adversely affected were the turbulence intensity within the flow to reach appreciably high levels; this would lead to a distribution of particle trajectories (for a given diameter and initial position) as opposed to deterministic trajectories.

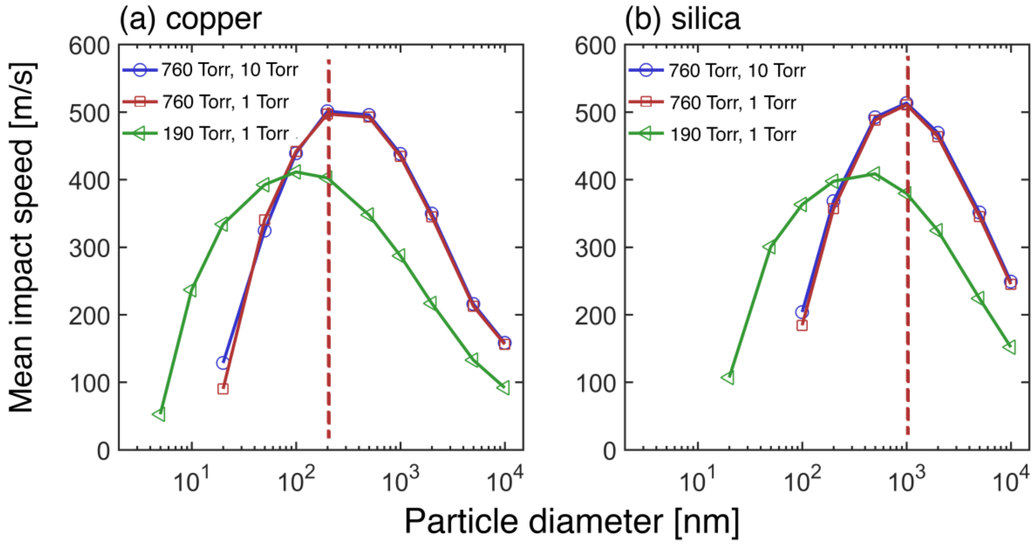

Figure 5.4. Comparison of (a) copper and (b) silica particle average impaction speeds. The red vertical lines denote the particle diameter of maximum impaction speed with 760 Torr upstream pressure.

The influence of particle density and nozzle operating pressures on average impaction speed are also shown in Figures 5.4a and 5.4b. For copper (denser) particles, Figure 4a indicates that changing the downstream pressure from 10 Torr to 1 Torr has a minimal effect on particle impaction speed. As discussed previously, a downstream pressure of 1 Torr results in a thicker post-shock region, albeit with lower gas density. The thickened post-shock region results in a longer deceleration distance for particles, while the decreased gas density reduces drag force on the particles in this region. These two effects work to oppose one another, such that impaction speeds for $d_p \geq 50\ nm$ are relatively insensitive to downstream pressure. Reduction of the upstream pressure has a much more significant effect on particle impaction speeds; an upstream pressure of 190 Torr leads to decreased particle impaction speed for $d_p > 100\ nm$, but a higher impaction speed $d_p < 100\,nm$. Supported by the results in Figure 5.2d, lowering the upstream pressure reduces the pressure in the post shock region, facilitating the deposition of small particles $(d_p < 100\,nm)$ but leads to incomplete acceleration of larger, more inertial particles in the nozzle. A comparison of Figure 5.4b to Figure 5.4a indicates that silica particle impaction speed follows the same trend qualitatively as copper particle impaction speed, but with one noticeable difference. The particle size for the maximum impaction speed is larger for silica particles (~$1\mu m$). Such a difference arises because silica particles have lower densities, and hence less inertia than copper particles of the same diameter. Though not shown, for silica, the maximally focused particle diameter is near 2 μm. Interestingly, the maximally focused particle diameter is larger than the particle diameter of maximum impaction speed for both materials. It is presently unclear if this is true in all deposition systems; all converging-diverging AD systems will display a maximally focused particle diameter and have maximum impaction speed diameter, though a clear relationship between these two diameters is likely system specific.

5.3.3 Mass, Momentum and Energy Transfer

5.3.3.1 A Framework for Flux Calculations

With particle size dependent impaction velocities and spatial distributions known, in this section we develop a framework to analyze the mass, momentum and kinetic energy fluxes to the substrate for any spatially uniform particle size distribution function in the upstream flow of the nozzle. The mass flux (M_A) at a point A on the substrate, which is a distance r from the center of the substrate, is given by:

$$M_A = \frac{\pi Q \rho_p}{6L} \int_0^\infty d_p^3 F\left(d_p, r\right) \frac{dn}{dd_p} dd_p \tag{5.10}$$

where Q is the volumetric gas flowrate through the nozzle, L is the nozzle slit length (i.e. *Q/L* is the flowrate per unit length) ρ_p is particle density, d_p is particle diameter, $F\left(d_p, r\right)$ is probability that a particle with diameter dp impinges at location A (i.e. it is the linewidth distribution function), and $\frac{dn}{dd_p}$ is the particle size distribution function upstream the nozzle, such that:

$$\int_0^\infty F\left(d_p, r\right) dr = P(d_p); \int_0^\infty \frac{dn}{dd_p} dd_p = N \tag{5.11}$$

where $P(d_p)$ is the deposition efficiency of particles with diameter d_p, *N* is the upstream number concentration of particles. The momentum flux (P_A) at location A in the direction perpendicular to the substrate (i.e. in the x direction) can be calculated via the equation

$$P_A = \frac{\pi Q \rho_p}{6L} \int_0^\infty \int_0^\infty (1 + \varphi_{dv}) d_p^3 v_x(d_{p,} r) F\left(d_p, r\right) \left.\frac{df}{dv_x}\right|_{r, d_p} \frac{dn}{dd_p} dv_x dd_p \tag{5.12}$$

where φ_{dv} is the fraction of particles rebounding (bouncing) from the surface, $v_x(d_{p,} r)$ is the particle velocity in the x direction, and $\left.\frac{df}{dv_x}\right|_{r, d_p}$ is the x-direction velocity distribution function of particles with diameter d_p impinging on location A ($\int_0^\infty \left.\frac{df}{dv_p}\right|_{r, d_p} dv_p = 1$). The quantity φ_{dv} needs to be determined by experiment or simulation, and is a function of particle size, particle material properties, impaction speed as well as substrate properties. Similar to the momentum flux equation, the kinetic energy flux from particles to the substrate surface (E_A) is given by:

$$E_A = \frac{\pi Q \rho_p}{12L} \int_0^\infty \int_0^\infty (1-\varphi_{dv}) d_p^3 v_p (d_{p,}r)^2 F(d_p, r) \left.\frac{df}{dv_p}\right|_{r,d_p} \frac{dn}{dd_p} dv_p dd_p \qquad (5.13)$$

where v_p is the particle speed and $\left.\frac{df}{dv_p}\right|_{r,d_p}$ is the speed distribution function.

The total mass, momentum, and energy flows/transfer rates can be obtained by integrating Equations (5.10), (5.12), and (5.13) over the substrate surface. To implement these equations, distribution functions, namely $F(d_p, r)$, $\left.\frac{df}{dv_p}\right|_{r,d_p}$ and $\frac{dn}{dd_p}$, need to be determined/prescribed. Among these quantities, $F(d_p, r)$ and $\left.\frac{df}{dv_p}\right|_{r,d_p}$ can be directly inferred from examining particle impinging locations and velocities, as are displayed in Figure 5.3c. We discuss both distribution functions in the subsequent section. Meanwhile, $\frac{dn}{dd_p}$ needs to be measured (and can be done using conventional aerosol measurement techniques, though is not commonly done in AD).

5.3.3.2 Flux Calculations

We elect to perform flow/transfer rate calculations for case 1 with copper particles, with an upstream pressure of 760 Torr and a downstream pressure of 10 Torr for different upstream particle size distributions. Figure 5.3c shows the impaction position and impaction velocity of individual particles. An examination of this figure leads to a number of simplifying assumptions for the implementation of flux equations. First, Figure 5.3c shows particles of a specific diameter deposit with clearly defined velocity at each impaction position. While this is the consequence of not including Brownian motion in the simulations, we anticipate the Brownian (thermal) influence on motion would be negligible. As a result, $\left.\frac{df}{dv_p}\right|_{r,d_p}$ can be approximated as a constant, and integration across this distribution function can be removed from the flux equations. Second, particles with diameters in the $50\text{nm} < d_p < 5\mu m$ range have impaction velocities/speeds which do not vary appreciably with impaction position. Therefore, $v_x(d_{p,}r)$ and $v_p(d_{p,}r)$ can be reduced to $v_x(d_p)$ and $v_p(d_p)$, independent of r in this size range. The last observation from Figure 5.3c is that within the impaction width, $F(d_p, r)$ can be approximated by a uniform distribution within a range, i.e.

$$F(d_p, r) = \begin{cases} \frac{1}{2\bar{r}(d_p)} & 0 \le r \le 2\bar{r}(d_p) \\ 0 & r > 2\bar{r}(d_p) \end{cases}, \tag{5.14}$$

where $2\bar{r}(d_p)$ is the half impaction linewidth. With these assumptions, equations (5.10), (5.12), and (5.13) can be rewritten as

$$M_A = \frac{\pi Q \rho_p}{6L} \int_0^\infty d_p^3 F(d_p, r) \frac{dn}{dd_p} dd_p \tag{5.15}$$

$$P_A = \frac{\pi Q \rho_p}{6L} \int_0^\infty (1 + \varphi_{dv}) d_p^3 v_x(d_p) F(d_p, r) \frac{dn}{dd_p} dd_p \tag{5.16}$$

$$E_A = \frac{\pi Q \rho_p}{12L} \int_0^\infty (1 - \varphi_{dv}) d_p^3 \left[v_p(d_p)\right]^2 F(d_p, r) \frac{dn}{dd_p} dd_p \tag{5.17}$$

Fluxes for three test lognormal particle size distributions of copper particles were calculated with the equations above. The three test lognormal distributions have different geometric mean diameters ($\mu =$200 nm, 800nm and $2\mu m$) but the same geometric standard deviation ($\sigma = 1.65$). The normalized particle size distribution functions of all three are shown in Figure 5.5a ($\frac{dF}{dln(d_p)}$, the integration of this distribution over $ln(d_p)$ is 1.0). The upstream particle concentrations, N, for the three distribution functions were

5 $\times 10^6$/cm^3, 7.85$\times 10^4$/cm^3 and 5.64 $\times 10^3$/cm^3, respectively. These concentrations were chosen so that the particle mass flowrate to the substrate is identical in each case. In general, these are dilute particle concentrations relative to what is experimentally obtainable. All subsequently reported results are linearly proportional to number concentration, provided the one-way coupling assumption remains satisfied (i.e. that the particles can be considered dilute). The gas flowrate through the nozzle, Q, was set to 21.3 liters per minute for a 1.2 cm length nozzle and was obtained from the fluid dynamics simulations.

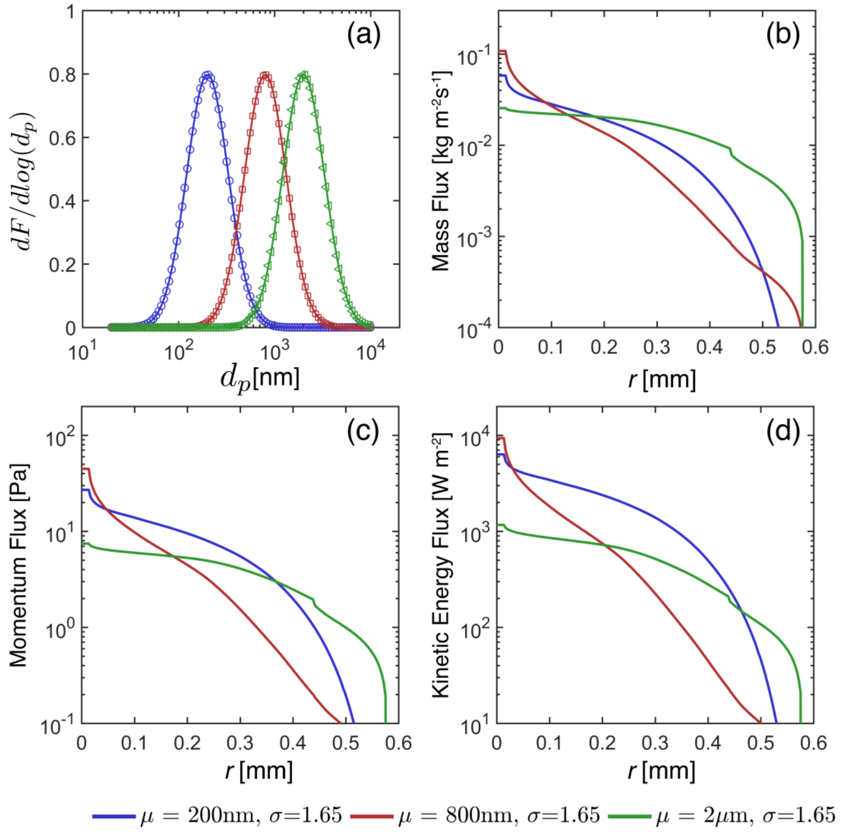

Figure 5.5. (a) Normalized test lognormal size distribution functions (μ: geometric mean, σ: geometric standard deviation). (b) Equation (5.10) calculated mass fluxes. (c) Equation (5.12) calculated x-direction momentum fluxes. (d) Equation (5.13) calculated kinetic energy fluxes.

The mass, x-momentum, and kinetic energy fluxes are plotted as functions of distance to the substrate center (r) in Figures 5.5b, 5.5c and 5.5d, respectively. The sudden drop in the 2 mm geometric mean curves near 4.5 mm arises because large particle deposition within the nozzle (affecting larger particle linewidth distribution functions). For mass fluxes, passage through the converging-diverging nozzle system has a clear focusing effect for all three distributions, as the mass flux is an order of magnitude higher (or more) at the nozzle center. Distribution 2 ($\mu =$800 nm) is most focused, while distribution 1 ($\mu =$2 μm) is the least focused. This is a direct result of the size-dependent focusing effect shown in Figure 5.3d. We note that although the geometric mean of distribution 3 ($\mu = 2\mu m$) is close to the optimal focusing size (refer to Figure 5.3d), the particles that take up the majority of particle mass have sizes greater than $2\mu m$; these particles are not as well focused.

Momentum and kinetic energy fluxes follow the same qualitative trend as the mass fluxes. However, it is not directly obvious from Figures 5.5c and 5.5d if momentum and kinetic energy are more focused than mass. To facilitate comparison, the ratio of mass, momentum and kinetic energy deposited within $r < 0.1$ mm and total mass, momentum and kinetic energy transfer rate is calculated for all three distributions ($r = 0.1$ mm corresponds to an impaction width of 0.2mm, which is the throat width of the nozzle). The ratios are provided in Table 5.2, together with the total transfer quantities. For distribution function 1, mass, momentum and kinetic energy have similar ratios, indicating the particles deposited within $r < 0.1$ mm do not have higher than average impaction speed. For distribution functions 2 and 3, kinetic energy and momentum are more focused than mass, indicating for these two distribution functions, particles deposited in the center region of the substrate also have greater impaction speed than average.

Table 5.2. Summary of upstream particle size distribution and flux quantities.

Distribution No.	1	2	3
Geometric mean	200 nm	800 nm	2 μm
Geometric standard deviation	1.65	1.65	1.65
Upstream particle concentration (#/cm3)	5×10^{6}	7.85×10^{4}	5.64×10^{3}
Total mass deposition rate (kg/s)	$\sim 2.05 \times 10^{-7}$	$\sim 2.05 \times 10^{-7}$	$\sim 2.05 \times 10^{-7}$
Total x-momentum transfer(N)	1.00×10^{-4}	7.58×10^{-5}	5.26×10^{-5}
Total kinetic energy transfer(W)	2.48×10^{-2}	1.44×10^{-2}	7.10×10^{-2}
Percentage of mass/momentum/ energy transfer within r<0.1mm	44.52% / 43.53% / 42.6%	61.83% / 66.22% / 70.07%	26.8% / 29.23% / 32.15%

With the framework proposed in Sect. 5.3.3.1, it is possible to calculate mass, momentum and kinetic energy fluxes for particle size distributions of any shape, as long as particle size distributions are spatially uniform in the upstream flow of the nozzle and the drag coefficients of the particles are appropriately described (C. L. Zhang et al., 2012). For spatially non-uniform particle size distribution functions, the framework is still applicable, and only requires modification of $F(d_p, r)$(which can be easily done when the spatial particle concentration function is prescribed). Also noteworthy in Figures 5.5c and 5.5d is that the momentum flux is relatively small (< 100 Pa) while the kinetic energy flux can be close to 10^4 W m^{-2}, even for the moderate particle number concentrations examined (concentrations two orders of magnitude higher are possible with standard fluidization approaches). This suggests that on average (not necessarily per particle impact) there is not a high pressure placed on the substrate by particle impaction. However, translational kinetic energy to thermal kinetic energy conversation can be extremely high, approaching a magnitude normally observed in convective heat transfer with phase change (particularly if the particle number exceeds the test concentration by an order of magnitude or more). Though this would be counteracted by convective cooling from the gas around the substrate, kinetic to thermal energy transfer may facilitate particle coalescence upon impact and may be a key reason that AD can yield dense, non-particulate coatings. We suggest that future studies of the AD process further investigate kinetic to thermal energy transfer during particle deposition, as energy flux calculations suggest the rate is high, enhanced by focusing effects, and strongly dependent and particle size distribution function. Such future investigations will require more detailed investigation of the one-way coupling assumption, which may breakdown if a sufficiently high concentration of particles is focused inertially.

5.4 Conclusions

We apply a trajectory calculation approach to examine particle transport in supersonic aerosol deposition using a converging-diverging nozzle and subsequently develop approaches to examine mass, momentum, and kinetic energy fluxes due to particle impaction on a substrate. To our knowledge, the latter flux calculations have not been attempted previously, and in addition the drag correlation applied in trajectory calculations is itself new, and specifically developed for AD gas conditions. Based upon this study, we draw the following conclusions.

1. The use of upstream atmospheric pressure in AD, as compared to its high upstream pressure cold spray counterpart, facilitates the inertial deposition of submicrometer particles. Further reducing the upstream pressure below atmospheric pressure enables inertial impaction for progressively smaller particles, which is also observed in experiments (Holman & Kortshagen, 2010). However, for a given upstream pressure, decreasing the downstream pressure beyond a critical value does not drastically influence inertial impaction. This is due to two counteracting effects; at reduced downstream pressure the pressure within the post-shock region is reduced, but the size of the post-shock region increases.
2. Simulations were performed dimensionally, mainly because AD conditions lead to drastically changing pressure and temperature, and hence selection of reference variables for non-dimensionalization is rather subjective. Nonetheless, we can generally conclude that in all supersonic deposition systems (i.e. those with converging-diverging nozzles and a perpendicular substrate), there is a particle diameter of maximum impaction velocity; smaller diameter particles are decelerated in the shock and post-shock region while larger particles are not accelerated to the gas velocity within the nozzle. The particle diameter of maximum impaction speed can be adjusted by changing nozzle dimensions

(though not studied directly here) as well as by varying upstream pressure and particle density. In addition, lateral inertial focusing in supersonic AD is significant and there will exist a particle diameter which is optimally focused (i.e. of infinitesimal deposition linewidth) in converging-diverging nozzle systems. Particles smaller than the critically focused diameter are underfocused while larger particles are overfocused. We suggest that future AD and cold spray systems be designed with the focused particle diameter in mind; rarely is the interplay between input particle size distribution function and inertial focusing considered in these processes.

3. Inertial focusing has significant effect on the particle mass, momentum, and kinetic energy flux distributions at the substrate surface. Among these, most interesting is the enhancement in kinetic energy flux distributions along the centerline of the nozzle; it appears such focusing can lead to kinetic energy fluxes approaching 10^4 W m^{-2} for modest aerosol concentrations (and hence up to 10^6 W m^{-2} for much higher concentration systems). We suggest that future studies of AD examine kinetic energy to thermal energy transfer for particle upon impact in light of the finding of highly focused kinetic energy transfer.

Chapter 6: Differentiation of Normal and Lung Cancer Cell Lines via VOC Profiling with Proton Transfer Reaction Time-of-Flight Mass Spectrometry

Abstract: There is growing interest in utilizing volatile organic compound (VOC) detection schemes in disease diagnosis and in monitoring cellular metabolism. However, the extent to which VOC analysis can be used in such applications remains to be determined. In this study, we employed proton transfer reaction-mass spectrometry (PTR-MS) to profile VOCs sampled from the headspace of *in-vitro* cultured cancerous (A549 and SHP-77) and non-cancerous (BEAS-2B) bronchial epithelial cell lines. The high resolution (>4000) of the mass spectrometer enabled ion signal distinction and ion formula identification by exact masses with high certainty in most instances. Using selected, standardized ion signals, we were able to partially separate different cell types with unsupervised statistical learning algorithms, i.e., principal component analysis (PCA) and hierarchical clustering. Separation and identification of cell types from VOC mass spectra was substantially improved by using supervised statistical learning algorithms. With multiple subsets of fewer than ten ions selected by an iterative procedure, 100% training and prediction accuracies were achievable in a repeated 6-fold cross validation using linear discriminant analysis (LDA) and support vector machine (SVM), which are both supervised learning algorithms. These results suggest that high-resolution PTR-MS coupled with supervised learning algorithm-based analysis is effective for VOC profiling and cell type identification. Furthermore, we found that with an

LDA classifier trained on samples cultivated in a single medium (BEGM), accurate predictions of cell types cultivated in a second medium (RPMI) are possible, provided that ion signals have been properly standardized.

6.1 Introduction

There is growing interest in developing diagnostic techniques that depend upon detection and quantification of biologically emitted, volatile organic compounds (VOCs) in gaseous mixtures (Banday et al., 2011; Rogers, Benkstein, & Semancik, 2012; Tuzson et al., 2017; Vergara, Benkstein, Montgomery, & Semancik, 2014), in particular as part of cancer screening (Haick et al., 2014; Hakim et al., 2012; Konvalina & Haick, 2014; Schmidt & Podmore, 2015). Such VOC profiling techniques have the potential to transform the manner in which medical diagnoses are performed; VOC profiling is generally non-invasive, can be performed in real-time, and with automation VOC analysis could enable point-of-care diagnosis. However, the extent to which VOC profiling can be used in cancer diagnostics remains to be determined, and there are presently no standardized and universally employed methods for VOC profile analysis (Hakim et al., 2012).

In the absence of standard methodologies, a variety of methods and instruments have been utilized to assess the potential of VOC profiling, using breath collected from cancer patients as well as headspace from *in vitro* cell culture experiments. The instruments employed include gas chromatography-mass spectrometry (GC-MS) (Filipiak et al., 2008; Kim, Mulholland, Kukuck, & Pui, 2005; Wojciech et al., 2014), selected ion flow tube-mass spectrometry (SIFT-MS) (Patrik & David, 2008; D. Smith &

Spanel, 2005; Sule-Suso, Pysanenko, Spanel, & Smith, 2009), proton transfer reaction-mass spectrometry (PTR-MS) (Brunner et al., 2010; Tali et al., 2017; Tali et al., 2016; Wehinger et al., 2007), along with a variety of nanosensors (Bartolazzi et al., 2010; Di Natale et al., 2003; Machado et al., 2005; Mazzone et al., 2007; Nakhleh et al., 2017; G. Peng et al., 2010; Gang Peng, Tisch, Adams, et al., 2009; Gang Peng, Tisch, & Haick, 2009; Rogers et al., 2012). GC-MS measurements provide the highest certainty in terms of compound identification for VOC profiling. However, this approach requires preconditioning of samples, and the relatively complex sample preparation and calibration procedures makes GC-MS unfit for online measurements in a diagnostic setting. Nanosensors are often rapid, portable, and potentially low cost, but individual sensors commonly respond to a wide range of VOCs (Röck, Barsan, & Weimar, 2008), complicating the interpretation of the sensor output (Konvalina & Haick, 2014). In contrast, SIFT-MS and PTR-MS (Adams & Smith, 1976; Lindinger, Hansel, & Jordan, 1998), which are one-dimensional separation detection techniques, are capable of online identification and quantification of VOCs. In prior studies using PTR-MS and SIFT-MS for VOC profiling (Brunner et al., 2010; Patrik & David, 2008; Sule-Suso et al., 2009; Tali et al., 2017; Tali et al., 2016), only unit mass resolution quadruple mass spectrometers were employed. Unit mass resolution prohibits clear determination of VOC atomic composition, leading to ambiguity in terms of the compounds detected and limiting the information obtained.

Online VOC detection with higher-resolution mass spectrometry would enable direct, near real-time identification of VOCs, and a more complete description of VOC profiles to aid in differentiation between samples. By itself, however, even highly comprehensive VOC profiling does not necessarily aid in diagnosis or classification. Typically, unique ions are not detected in different samples/patients, hence diagnosis or classification must be based upon subtle differences in signal intensity for multiple analytes. High-resolution VOC profiles need to be coupled with appropriate data analysis approaches in order to (1) identify metabolic VOCs (biomarkers) whose concentrations correlate with cell concentration (in *in vitro* studies) and disease progression; (2) detect the presence of different cell populations (i.e., cancerous and non-cancerous cells), or presence or absence of tumors; and (3) assess the degree to which VOC profiling is sensitive to environmental conditions or sampling procedures.

To date, VOC profiles, quantified by different means, have been analyzed via a variety of statistical learning algorithms, including principal component analysis (Barash, Peled, Hirsch, & Haick, 2009; Chen et al., 2016), linear/quadratic discriminant analysis (Brunner et al., 2010; Wehinger et al., 2007), logistic regression (Kumar et al., 2015), and support vector machine (Barash et al., 2012). Though prior work has made use of online mass spectrometry and statistical learning algorithms in VOC profiling *in-vitro* and *in-vivo*, these algorithms have not been applied to online high-resolution mass spectra. To directly address this gap, we have developed an approach to analyze VOC profiles generated by lung epithelial cell cultures (both cancerous, A549 and SHP-77, and non-cancerous BEAS-2B cells) using PTR-MS with a high-resolution (>4000 for most analytes) time-of-flight mass spectrometer. Measurements were made in real-time, with VOCs sampled in a continuous flow system. The resulting high-resolution spectra were analyzed to identify specific ions that correlate with cell concentration and to distinguish different cell lines from one another. For cell line identification, we employed both unsupervised and supervised learning algorithms; for the latter we specifically utilized linear discriminant analysis and support vector machine. Through cross-validations, we discovered that the supervised learning algorithms enabled cell type identification from high-resolution VOC profiles using signals from fewer than 10 ions. Additionally, we found that ions used for classifying cells cultivated in one medium (bronchial epithelial growth medium; BEGM) can be used to predict cell types cultivated in another medium (RPMI-1640). Based on these results, we propose that high-resolution PTR-MS can serve as a robust method for VOC profiling from cell culture headspace, and by extension in a variety of other biological and environmental systems.

6.2 Experimental Section

6.2.1 Cell Culture Preparation

We cultured cells in a manner enabling direct VOC sampling without the need to remove them from their growth medium. Human immortalized normal bronchial epithelial cells, BEAS-2B, and lung squamous cell carcinoma cells, A549 and SHP-77, were purchased from American Type Culture Collection (ATCC), Manassas, VA USA. BEAS-2B cells were maintained in bronchial epithelial base medium supplemented with additives (BEGM) provided by the manufacturer as a kit (cat# CC-3170, Lonza Inc., Walkersville, MD USA). A549 and SHP-77 were maintained in RPMI-1640 (ATCC, cat# 30-2001) supplemented with 10% fetal bovine serum (RPMI). To normalize growth medium conditions, all cells were maintained in either BEGM or RPMI-1640 during VOC sampling.

Prior to VOC sampling in BEGM, cells were seeded and cultured overnight in their respective growth medium at a total of 10^7 cells per chamber (n = 42) in Corning CellSTACK® Culture Chambers (Corning #3268, Fisher Scientific, Pittsburgh, PA USA) (Figure 6.1), as A549 and SHP-77 cells do not adhere well when seeded in BEGM. We also performed experiments with 2.5×10^6 (n = 6) and 5×10^6 (n = 6) cells per chamber to examine the influence of cell concentration on classification, but we found no detectable difference in the results relative to the chambers with 1×10^7 cells. Cells grown overnight were then washed twice with pre-warmed phosphate buffered saline (PBS) and cultured in BEGM for an additional 16 - 18 h. For VOC sampling with the RPMI-1640 medium, cells were seeded and maintained directly in RPMI-1640 for the same duration without the washing step. All cells were maintained in a humidified incubator at 37°C, 5% CO_2, and atmospheric pressure prior to and during VOC sampling. For growth medium controls, chambers containing growth medium (BEGM or RPMI-1640) alone were maintained and sampled under the same culture conditions.

To enable direct VOC sampling, two ports (¼” swagelok^{TM} ports) were custom-machined in each CellSTACK® Culture Chamber as shown in Figure 6.1. After machining, each chamber was resterilized using a vaporized peracetic acid (VPA) sterilant (Revox Sterilization Solutions, Plymouth, MN USA). Culture chambers were then repackaged and stored prior to use in cell growth.

6.2.2 Cell Culture Headspace VOC Sampling

A custom-made VOC sampling and PTR-MS introduction system was used for all experiments (depicted in Figure 6.1). VOCs were sampled from the headspace of cell cultures continuously for ~5 minutes by passing 0.5 L min^{-1} of ultrahigh purity zero air (sample flow) through one of the ports in each chamber. The sampling flow passed over the cell culture within each chamber, exiting through the second machined outlet port. During sampling and measurement, each cell culture chamber was held in a humidified incubator as described above (37°C; 5% CO_2). Upon exiting the cell culture chamber, the VOC-laden sample flow was mixed with a 2.0-4.5 L min^{-1} zero air dilution flow to avoid saturation of the PTR-MS detector during measurement. Heated Teflon sampling lines (>40°C) were used to minimize any VOC losses or surface reactions prior to measurement, with separate Teflon lines used for each cell type. Background measurements were performed by passing sample flow through an empty cell culture chamber (containing neither culture medium nor cells). New samples were not tested until measured PTR-MS signals for $(C_2H_7O)^+$ and $(C_2H_5O)^+$ returned to established background levels.

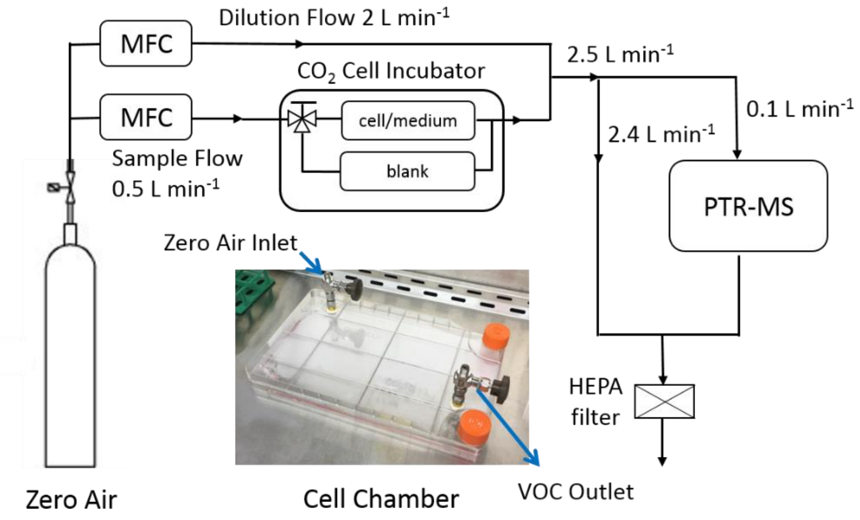

Figure 6.1. A schematic diagram of the cell chamber used for the VOC sampling experiments. PTR-MS: Proton transfer reaction-mass spectrometer; MFC: Mass flow controller.

6.2.3 PTR-MS Operation

VOCs were analyzed with a commercially available PTR-QiTOF (Ionicon Analytik, GmbH). Instrument settings were optimized to provide high resolution (Δm/m ~ 4500 for acetone) and sensitivity (700 cps/ppb for acetone). The PTR was operated with a drift tube pressure of 3.8 mbar, a drift tube temperature of 75°C, E/N of 138 Td, and an inlet temperature of 75°C. The time-of-flight analyzer was operated over an *m/z* range of 0-510 (extraction period 40 μs), with the mass axis calibrated continuously via addition of a diiodobenzene internal standard. In general, proton transfer reaction is a relatively soft ionization technique with limited fragmentation, and many VOCs are detected as the protonated molecular ion at (M+1.008) Th, where M is the molecular mass of the neutral compound. However, some fragmentation can occur (Yuan et al., 2017), with the extent dependent upon instrument operating conditions (Baasandorj, Millet, Hu, Mitroo, & Williams, 2015) (e.g., E/N > 120 Td) and type of VOC (e.g., alcohols). Mass axis calibration, transmission correction, and peak fitting and integration were performed with PTR-MS VIEWER 3.2.5 post processing software, using a dedicated peak table based on detected peaks over the observed *m*/*z* range. Subsequent data processing was performed using a custom set of R routines (www.R-project.org).

6.3 Data Analysis

Both unsupervised and supervised learning algorithms were employed in analyzing PTR-MS data in order to assess the relative value of these techniques in VOC profiling with exact mass measurements. We first describe how mass spectrometer signal intensities were standardized, followed by a description of each employed method.

6.3.1 Cell Type Classification

To determine whether VOC profiling can be used as a robust diagnostic method, we applied three statistical learning algorithms: Principal component analysis (PCA), linear discriminant analysis (LDA), and support vector machine (SVM). PCA is an unsupervised algorithm while the LDA and SVM are supervised learning algorithms. PCA projects the data onto new dimensions to maximize variance, without taking data categories (cell types, in our case) into account. LDA assigns a sample to a type that has the highest posterior probability, assuming different types are normally distributed and have the same covariance matrix. SVM is a maximum margin classifier that separates different sample types by a hyperplane in a ($p+1$)-dimensional space, where p is the number of features (standardized ion signals, in our case). SVM is readily extendable to the generation of non-linear separation boundaries via data transformation with non-linear kernel functions. All three algorithms were implemented with the Python machine learning package scikit-learn (Pedregosa et al., 2011).

The number of distinct peaks detected by high-resolution PTR-MS for our samples was more than 600, far exceeding the number of independent measurements (18 samples for each cell type). Using all detected peaks in cell classification would likely lead to overfitting (Ziegel, 2003) in training the statistical learning algorithms. We thus employed a procedure to select ions that can best classify and predict cell types. Specifically, we first selected the 100 most abundant ions in terms of average signals (after averaging over all samples), as higher signal ions are less affected by random measurement error, and the average signal intensity for ions other than the selected 100 are all below 0.7 counts per second. We next applied a Kruskal-Wallis test to the standardized signals of the individual ions and retained ions that give a p-value < 0.005 (which indicates there are likely multiple signal intensity distributions present, and the ion in question may thus be a good predictor of sample type). With the resulting ions, we then found the optimum combination of k ion signals that yields the highest sample type prediction accuracy in *6*-fold cross validation. We selected 6-fold for the convenience of data splitting. To mitigate the error introduced by specific fold divisions, we repeated the cross validation 10 times and obtained an average prediction accuracy, each time using a different, randomized fold division. The value of k ranges from 1 to the number of ions identified by the Kruskal-Wallis test. We iterated through all combinations of k ions to ensure identification of the optimum combination for classification.

6.3.2 Inter-medium Comparison

To compare VOC profiles for cells grown in different media, seven measurements were performed with cells grown in RPMI (with one measurement for the medium alone, and two measurements for each cell line). Because the number of measurements for cells grown in RPMI was limited, we applied the following method to verify that the statistical learning classifiers built for cell lines grown in BEGM could also be applied to cell lines grown in RPMI. First, we applied Equation (6.1) to standardize ions signals from cell lines grown in RPMI. In doing so, only the differences between different cell lines were preserved, while information regarding absolute VOC concentration was discarded.

Second, we built an LDA classifier based on cell lines grown in BEGM using ions identified by the aforementioned selection procedure. Third, we applied this classifier to cell lines grown in RPMI to calculate prediction accuracy for the cell lines grown in RPMI, as well as to visualize where each PTR-MS measurement for RPMI-grown cells was located in the LDA-transformed coordinates.

6.4 Results and Discussion

6.4.1 PTR-MS Raw Spectra

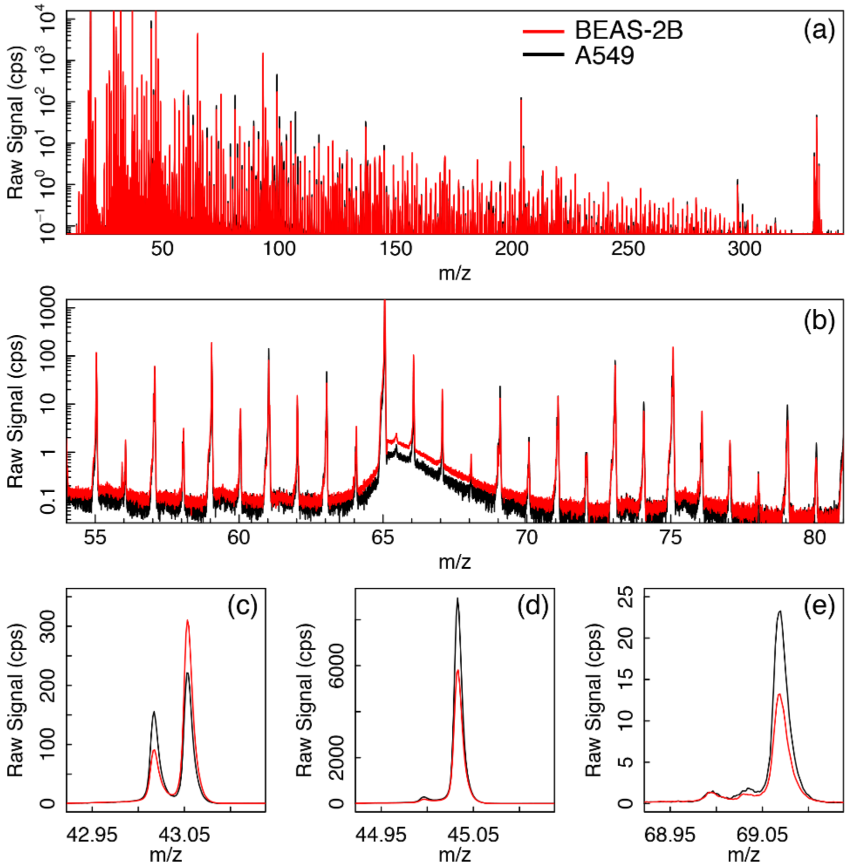

Figure 6.2. Representative PTR-MS spectra for BEAS-2B (red) and A549 (black) cell lines. (a) 0-350 Th range mass spectrum. (b) 54-81 Th range mass spectrum. (c) Separation of $C_2H_3O^+$ (measured *m/z* = 43.018) from $C_3H_7^+$ (measured *m/z* = 43.053). (d)

Separation of CO_2H^+ (measured *m/z* = 44.997) from $C_2H_5O^+$ (measured *m/z* = 45.034). (e) Ion signal of $C_5H_9^+$ (major peak, measured *m/z* = 69.070).

To illustrate differences between VOC profiles from different cell populations, Figure 6.2 shows the time-averaged representative PTR-MS spectra for one BEAS-2B sample (red) and one A549 sample (black). Figures 6.2a and 6.2b display the spectra for m/z ranges of 0-350 Th and 54-81 Th, respectively. From these two figures, it is evident that (1) VOC concentrations can differ by orders of magnitude, and (2) the ion peaks detected from both cell populations were identical in exact mass, i.e. biomarkers specific to only one cell population were not identified from these spectra. Figures 6.2c-6.2e are amplified versions of the spectra; they highlight ion signal differences from different cell populations, and further show that the high-resolution PTR-MS separates peaks of the same nominal mass but disparate exact mass. All three plots show discernable ion signal differences between the BEAS-2B and A549 samples, although such differences did not exceed the order of magnitude of the ion signals themselves.

6.4.2 Signal Distribution of Selected Ions

Prior to statistical analysis, we present the standardized concentration distributions for selected ions produced by cells lines grown in BEGM. These ions were among those that had the lowest *p*-values in the Kruskal-Wallis test, and their relatively low mass-to-charge ratios allowed us to determine their ion formulae with high certainty. Lower *p*-values indicate that the detected ion signals were less likely to be sampled from the same distribution, and therefore are potential ‘biomarkers’ of certain cell lines. The measured *m/z* values, tentative ion formulae, and identities of these ions are listed in

Table 6.1, along with their *p*-values. As noted in the "PTR-MS Operation" section, although PTR-MS employs a soft ionization technique (i.e., proton transfer reaction), certain species do dissociate/fragment during the ionization process, in some cases generating akyl chains. For instance, among the ions listed in Table 6.1, *m/z* = 55.051 corresponds to an ion formula of $C_4H_7^+$, which could either be a protonated unsaturated hydrocarbon (e.g., butadiene) or fragment of an aldehyde (Buhr, van Ruth, & Delahunty, 2002; Warneke, de Gouw, Kuster, Goldan, & Fall, 2003) (e.g., butanal). Similarly, *m/z* = 83.081 corresponds to an ion formula of $C_6H_{11}^+$, which could be a protonated unsaturated hydrocarbon (e.g., hexadiene), or the fragmentation product of an aldehyde or alcohol (Buhr et al., 2002; Warneke et al., 2003) (e.g., hexanal or hexenol) (Amelynck, Schoon, Kuppens, Bultinck, & Arijs, 2005; Lee et al., 2006).

Table 6.1. Measured mass-to-charge ratios, tentative molecular formulae, and assigned identities of selected ions. Mass difference (in milliDaltons) denotes the difference in mass-to-charge ratio determined via PTR-MS and the exact mass of the assigned formula. A Kruskal-Wallis test was applied to the standardized ion concentration.

Measured *m/z*	43.018	45.033	55.051	59.049	69.070	83.081
Ion formula	$C_2H_3O^+$	$C_2H_5O^+$	$C_4H_7^+$	$C_3H_7O^+$	$C_5H_9^+$	$C_6H_{11}^+$
Mass difference (mDa)	< 1	1	3	< 1	< 1	5
Possible identity	fragment	protonated acetaldehyde	fragment or protonated butadiene	protonated acetone or propanal	fragment or isoprene	fragment or protonated hexadiene
p-value of Kruskal-Wallis test	1.95×10^{-6}	6.9×10^{-7}	1.8×10^{-9}	1.1×10^{-5}	1.22×10^{-7}	1.1×10^{-9}

Figure 6.3 shows the signal distribution (box and whisker plot) for the six ions in Table 6.1, along with the formula for each ion. The abscissa indicates cell line type and the ordinate is standardized ion concentration calculated by Equation (6.1). It is evident from these data that ion signals from different cell types follow distinct distributions. For example, the A549 cell line exhibited lower concentrations of $C_2H_3O^+$, $C_2H_5O^+$ and $C_5H_9^+$ (Figures 6.3a, 6.3b and 6.3e) than BEAS-2B and SHP-77. In contrast, A549 cells exhibited more $C_4H_7^+$, $C_3H_7O^+$ and $C_6H_{11}^+$ than the other two cell lines (Figures 6.3c, 6.3d and 6.3f). Overall, A549 cells tend to separate from the other two cell lines while ion signals from BEAS-2B and SHP-77 cells showed a greater extent of overlap. Because our results showed that no single compound fully separated all three cell lines, we applied statistical learning algorithms for cell type identification.

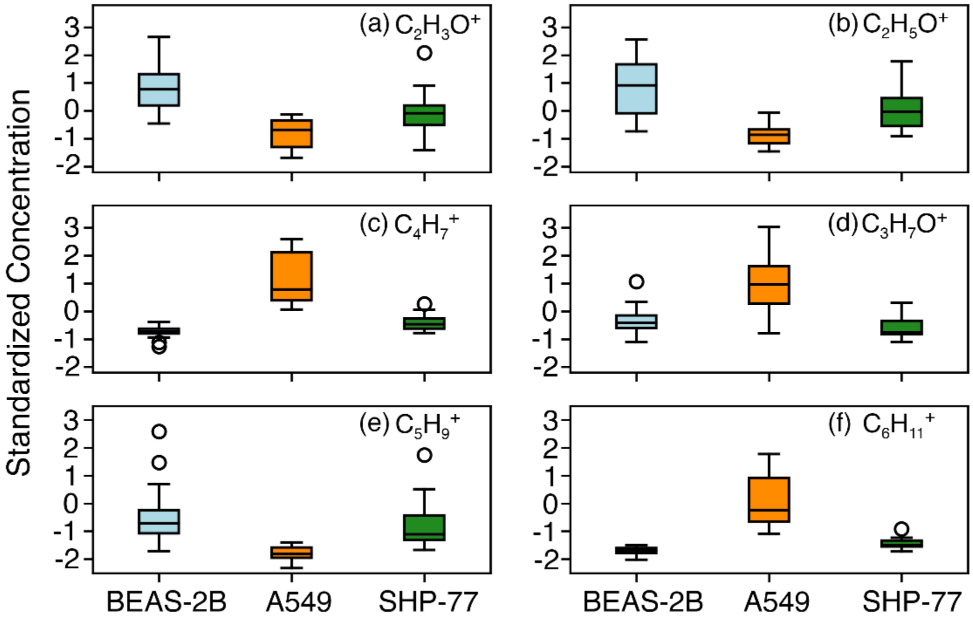

Figure 6.3. Standardized concentration distributions for selected ions. Each box represents the first and third quartiles, with the black line denoting the median for each sample. The whiskers extend to the most extreme point within 1.5 interquartile ranges from the box.

The ions identified above have been reported previously in VOC profiling of cancer cell lines (Brunner et al., 2010; Filipiak et al., 2008; D. Smith & Spanel, 2005; Sponring et al., 2009; Sule-Suso et al., 2009). In particular, *m/z* = 45.033 likely corresponds to acetaldehyde, which has been extensively studied in prior *in vitro* cell breath studies. The acetaldehyde concentration was previously shown to increase in the headspace of SK-MES and CALU-I metastatic lung carcinoma cell cultures (D. Smith & Spanel, 2005; Sule-Suso et al., 2009) and in the headspace of normal lung epithelial NL20 cell cultures (Sule-Suso et al., 2009), while decreases were observed in 35FL121 Tel+ lung fibroblast cells (Sule-Suso et al., 2009). In contrast, Brunner et al.(Brunner et al., 2010) reported that acetaldehyde was consumed by A549 and EPLC lung carcinoma cell lines. Filipiak et al.(Filipiak et al., 2008) and Sponring et al.(Sponring et al., 2009) also found decreased acetaldehyde concentrations in the headspace of CALU-I and NCI-H2087 metastatic lung carcinoma cell cultures, respectively. We found that the average *m/z* = 45.033 ion concentration decreased in the headspace of the A549 cells compared to that detected for the BEAS-2B and SHP-77 cell lines. The observed decrease in acetaldehyde concentration may be due to the increased aldehyde dehydrogenase (ALDH) enzymatic activity identified in A549 cells (Filipiak et al., 2008).

6.4.3 Statistical Learning Algorithm Classification & Prediction

We used the statistical analysis procedures outlined in the *Data Analysis* section to classify and predict different cell types grown in BEGM. By setting a screening criterion of $p < 0.005$ in the Kruskal-Wallis test, 19 peaks were selected as candidate features for statistical learning algorithms. The *m/z* values of the 19 peaks are provided in

Table I1. Using these top 19 candidate ions, we first performed unsupervised classification by PCA. Figure 6.4a shows that samples from different cell populations clustered around distinct positions in the 3-D principal component space. To aid visualization, 2-D plots with different principal components as axes are also included. Figure 6.4b demonstrates that the A549 cell population was well separated from the other two, while Figure 6.4c shows that separation between the BEAS-2B and SHP-77 cell populations was mainly along the third principal component, though the boundary between these two cell populations was narrow.

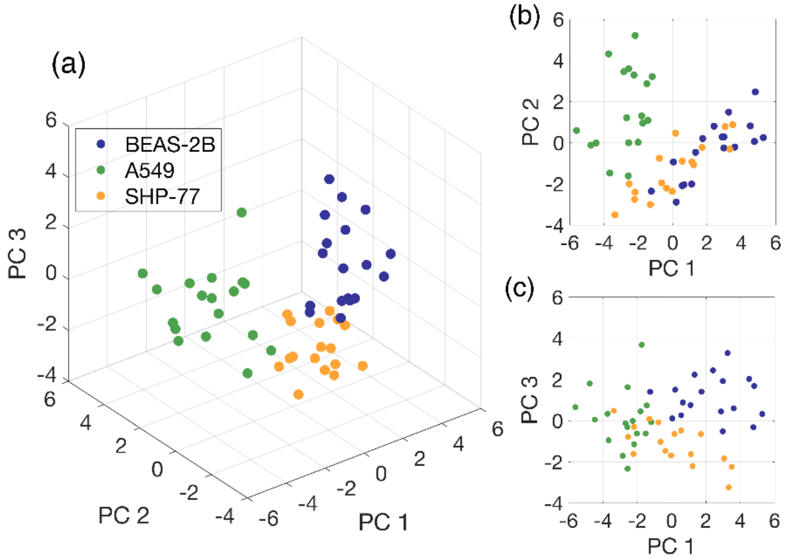

Figure 6.4. (a) 3-dimensional PCA results obtained using the 19 candidate ions selected by the Kruskal-Wallis test. (b) 2-dimensional plot of principal components 1 and 2. (c) 2-dimensional plot of principal components 1 and 3.

Though PCA reveals some degree of separation between cell types in three-dimensions, the resulting boundaries between cell types are narrow. Additionally, PCA alone is insufficient for cell type prediction; for this purpose, it would need to be combined with other techniques such as regression analysis. We hence used supervised machine learning algorithms (LDA and SVM) to more definitively classify and predict the cell types using the top 19 candidate ions. The relatively small number of candidates enabled us to use an iterative method to find the best subset of ions for predicting cell type with high accuracy. The prediction accuracy is calculated by repeated 6-fold cross validation. Results from the subset selection are shown in Figure 6.5 for both LDA and SVM. The abscissa is the number of ions in the subset (*k*), and the ordinate is the highest prediction accuracy obtained among all combinations of k ions. For example, if 5 peaks are chosen to predict the cell type, a total number of $C_5^{19} = 11628$ ion combinations exist. Figure 6.5a shows that the highest prediction accuracy achieved by LDA among the 11628 combinations (at k = *5*) is 98.1%, while Figure 6.5b shows that the highest prediction accuracy achieved by SVM is 98.3%. We note that for SVM, a grid search was performed for the regularization parameter λ in the range $\lambda \in [0.5, 3]$. Results were not sensitive to the value of λ within this range and Figure 6.5b shows the result for λ=1.5.

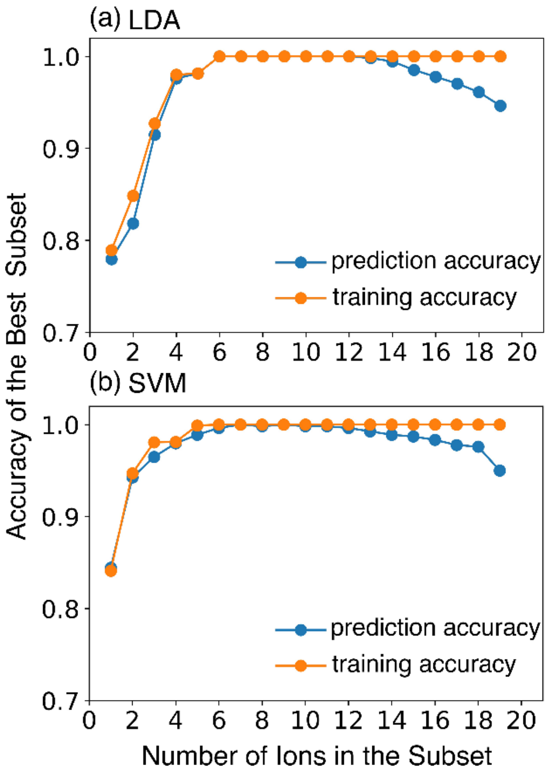

Figure 6.5. Highest prediction accuracy as a function of the number of features used in the classification algorithm for linear discriminant analysis (LDA) and support vector machine (SVM). Training accuracy denotes the accuracy of the method in cell line identification when applied to the same samples used in training the algorithm in question (orange line). Prediction accuracy applies when identifying samples not used in the training set (blue line).

For LDA and SVM, the training accuracy and prediction accuracy both increased initially and reached perfect prediction accuracy when 6-7 ions were included in the predictions (Figure 6.5). However, as the number of ions included in the algorithms was further increased, prediction accuracy started to decrease, while training accuracy remained close to 1.0. The decline of prediction accuracy was attributed to overfitting, since an increased number of features lead to a close fit to the training dataset yet resulted in poorer prediction of cell type when applied to data beyond the training set. The *m/z* values for ions in the best subset for *k* = 1-5, along with their training and prediction accuracies, are shown in Table 6.2. We note that the ‘best subset’ of ions is not necessarily unique, i.e. there can be multiple subsets containing *k* ions that give the same or nearly the same prediction accuracies. As a result, the subset presented in Table 6.2 should be regarded as representative of a number of ideal subsets. More comprehensive results for *k* = 6~10 are included in Table I2 in Appendix I. It is also important to note that the results presented in Figure 6.5 are subject to data availability, i.e. a larger dataset typically enables the effective use of more features without overfitting.

Table 6.2. A summary of the highest-level prediction accuracy sets using both linear discriminant analysis and support vector machine, for *k* = 1-5.

	k	m/z	Prediction Accuracy	Training Accuracy
LDA	1	83.081	0.780	0.789
	2	55.052,149.103	0.819	0.849
	3	55.052,70.073,99.080	0.915	0.927
	4	70.073,71.050,83.081,149.103	0.976	0.980
	5	69.070,70.073,71.050,83.081,149.103	0.981	0.981
SVM	k	m/z	Prediction Accuracy	Training Accuracy
	1	83.081	0.828	0.837
	2	55.052,149.103	0.946	0.948
	3	55.052,71.050,149.103	0.970	0.980
	4	31.018,71.050,83.081,149.103	0.980	0.981
	5	43.018,55.052,70.073,71.050,179.106	0.983	0.996

Importantly, we found that (1) signal intensity measurements for as few as five VOC-derived ions allowed identification of the cancer cell lines with high accuracy (>95%), and (2) multiple subsets in this *k*-range (*k* = 1-19) were successful in achieving high-accuracy prediction. These subsets contain multiple features (standardized ion signals), yet do not include all features (suppressing overfitting). The data analysis procedure (Kruskal-Wallis test followed by subset selection) is general and can be applicable to similar problems. For example, the technique can be applied to non-mass spectrometric data, or for improved classification by mass spectrometry in other biological/environmental systems (e.g., bacterial identification).(Hamid et al., 2014) More advanced data processing techniques, such as quadratic discriminant analysis (Wehinger et al., 2007) and non-linear SVM (Ziegel, 2003) can be used depending on the complexity of the problem and data availability, though we find LDA and linear SVM adequate for the present study.

6.4.4 Predicting Cell Type Cultivated in a Distinct Medium (RPMI)

Concentrations of VOCs sampled from cell cultures can certainly be influenced by medium composition and growth conditions due to changes in metabolic pathways (Tali et al., 2017). To determine whether the statistical learning classifiers built for cells grown in one medium can be applied to cells grown in a second medium for cell type classification, we used 12 ions to build an LDA classifier that was trained on the data from cells cultured in BEGM growth medium. These ions (denoted by '*' in Table I1) were chosen by the same subset selection procedure as above and achieved 100% prediction accuracy in cross validation for cell lines grown in BEGM. We then applied this classifier to the 6 cell culture samples (two of each cell line) grown in RPMI. Prior to classification, we standardized the ion signals of the 6 samples grown in RPMI using Equation (6.1).

We found that cell types grown in both BEGM and RPMI medium are well-separated, and the prediction accuracy is 100% (6/6) for cell lines grown in RPMI. Figure 6.6 shows the location of each cell type in the transformed coordinates by LDA. Compared to the PCA results shown in Figure 6.4, separation of different cell types was significantly improved; the boundary areas between cell types are comparable in size to the areas spanned by individual cell type data in Figure 6.6. Figure 6.6 also suggests that by using properly standardized data analysis procedures with exact mass PTR-MS, it is possible to build statistical learning classifiers that successfully predict cell types across distinct mediums. We note that the use of standardized data (e.g., via Equation (6.1)) is necessary to achieve cross-medium classification since classification using unstandardized data was unsuccessful (data not shown). This issue arises because signals of the same ion from different media can differ significantly (even by orders of magnitude). For example, the m/z = 45.035 (likely protonated acetaldehyde) ion signals obtained from the BEGM medium are ~10^4 counts per second, versus ~10^2 counts per second for RPMI. Despite such differences in ion signal intensity, the standardization process (population averaging) converts ion signals to the same order of magnitude while preserving differences between cell lines, thus allowing the LDA classifier to be applied across cells grown under different conditions.

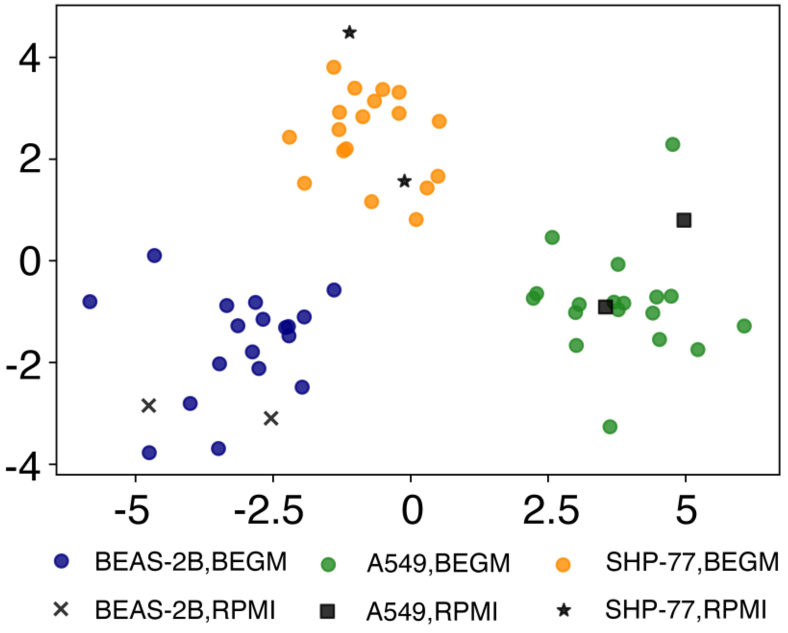

Figure 6.6. The positions of all samples on LDA transformed coordinates. The LDA is trained on 54 cell culture samples grown in BEGM, with 18 samples from each cell line. Twelve ions, selected by the subset selection procedure, are used as features for LDA. The trained LDA is then applied to standardized signals from 6 cell cultures grown in RPMI.

6.5 Conclusions

We performed online VOC profiling using proton transfer reaction time-of-flight mass spectrometry for in vitro cultured cancerous (A549 and SHP-77) and non-cancerous (BEAS-2B) cell lines. Based upon this study, we draw the following conclusions:

1. Compared to previous studies using PTR-MS, the high resolution of the instrument used in this study allowed us to determine the exact atomic composition of certain detected ions, greatly reducing the uncertainties in peak assignment.

2. Standardized ion signals from different cell populations followed distinct distributions. Statistical learning algorithms, both unsupervised (PCA and 2D-hierarchical clustering) and supervised (LDA and SVM), were applied to the standardized ion signals. Although PCA and hierarchical clustering enabled some degree of cell type separation, we were able to predict cell types with higher accuracy and confidence using LDA and SVM. An iterative selection method was employed to identify the best ion subsets for cell type classification. With multiple selected subsets, 100% prediction accuracy was achieved in repeated 6-fold cross validation.
3. Using an LDA classifier built for cells grown in BEGM, we were able to identify cell types grown in RPMI, despite the differences between VOC absolute concentrations from the two different growth conditions. Ion signal standardization that preserves differences between cell lines was required for such cross-media classification. To examine the limitations of this approach, more experiments with other cell lines and different growth conditions are needed.
4. The method presented for this study (VOC profiling by high resolution PTR-MS followed by ion signal standardization, Kruskal-Wallis test, and subset selection) can be incorporated into a framework for fast classification of *in vitro* cultured cell lines. This approach could be useful for the development of non-invasive methods for cancer diagnosis from human breath.

Chapter 7: Conclusions

The studies performed in this thesis aimed to further our understanding of particle formation, growth, and transport. Additionally, volatile organic compound profiling was performed to explore the possibility of cell type classification and prediction. These studies collectively lead to the following conclusions:

First, by non-dimensionalizing the general dynamic equation, solutions were obtained for a constant reaction rate system with a discrete-sectional model. The solutions were independent of the production rate of the condensing species; instead, they depend on a set of dimensionless parameters that characterizes evaporation, particle loss processes, dilution, and acid-base reaction. It was demonstrated that for a single species system, particle nucleation approaches the collision-controlled limit as the relevant dimensionless parameters approach zero. For nucleation involving acid-base reactions, the collision-controlled limit was reached when the dimensionless base concentration is sufficiently high. As a result, these parameters provide a guide to determine if a specific process has a significant effect on particle nucleation and growth. Using the same framework, the errors of commonly used growth rate calculation methods were evaluated. It was found that the log-normal distribution function method could lead to an overestimation of the true particle growth rate by a factor as large as 6. The maximum overestimation occurs at the collision-controlled limit, at which a maximum number of particles were produced that lead to significant particle coagulation. It was also shown that preexisting particles affect the particle nucleation process to a greater extent when evaporation is non-negligible.

Second, tandem DMA-MS measurements of organic vapor sorption to sodium chloride cluster ions suggest heterogeneous vapor uptake strongly depends on the structure of the vapor molecules, the cluster ion structure and the cluster ion polarity. Such measurements were performed systematically in this work for the first time. Butanol and ethanol showed strong uptake by both positive and negative cluster ions. MEK sorbs to positively charged cluster ions as well, but only slightly to negatively charged ions. Toluene showed only slight sorption to cluster ions of both polarities. A Langmuir model with two parameters, activity coefficient and number of sorption sites, was fitted to the experimental data to quantitatively infer the number of molecules that sorbs to the cluster ion surface. These results, along with existing CPC activation data, indicate heterogeneous vapor uptake process should be examined from a molecular perspective in future studies. Additionally, in the future design of condensers and condensational particle counters for size ranges close to 1nm, activation efficiencies should be examined for a variety of clusters with variable structures.

Third, as to particle transport in a converging-diverging nozzle, fluid dynamics along with particle trajectory simulations of the aerosol deposition process enabled detailed calculation of particle impaction speeds as well as mass, momentum and heat transfer rates to the substrate. By fitting to existing experimental data and simulation data obtained by direct simulation Monte Carlo (DSMC), a neural network fitting was found to give a more accurate drag law than previously developed empirical correlations. Using the new drag law, it was found that there was an optimal particle size that achieves maximum impaction speed due to presence of the shockwave close to substrate. This indicates a good control over the depositing particle size distribution can maximize particle impaction speed, facilitating production of compact films. Similarly, particle trajectory simulations showed that size dependent particle inertial focusing occurs, with an optimal focusing particle size that produces the smallest deposition linewidth on the substrate; this effect facilitates mass and energy focusing along the centerline of the nozzle. Future design of the aerosol deposition apparatus should take into the account the size dependency of the particle impaction speed and particle focusing.

Finally, cell type classification and prediction were performed with PTR-MS VOC profiling and selected machine learning algorithms. Though unique biomarkers specific to cell types were not discovered, VOC concentration differences among cell types were sufficient for accurate cell type classification and prediction. Using a few standardized ion signals (6~7) as an input to supervised machine learning algorithms can lead to near 100% prediction accuracy of cell types. It was also found that the influence of cell culture medium can be mitigated by proper data standardization; as a result, machine learning classifier trained with samples cultivated in one medium can be used to predict cell types cultivated in another medium. The result of this study suggests robust cell type prediction can be achieved based on VOC measurements by PTR-MS.

Bibliography

Abouali, O., & Ahmadi, G. (2005). A model for supersonic and hypersonic impactors for nanoparticles. *Journal of Nanoparticle Research, 7*(1), 75-88. doi:10.1007/s11051-004-7910-3

Adachi, M., Okuyama, K., Kousaka, Y., & Tanaka, H. (1988). Preparation of gas sensitive film by deposition of ultrafine tin dioxide particles. *Journal of Aerosol Science, 19*(2), 253-263. doi:10.1016/0021-8502(88)90227-3

Adams, N. G., & Smith, D. (1976). The selected ion flow tube (SIFT); A technique for studying ion-neutral reactions. *International Journal of Mass Spectrometry and Ion Physics, 21*(3), 349-359. doi:10.1016/0020-7381(76)80133-7

Akedo, J. (2006). Aerosol Deposition of Ceramic Thick Films at Room Temperature: Densification Mechanism of Ceramic Layers. *Journal of the American Ceramic Society, 89*(6), 1834-1839. doi:10.1111/j.1551-2916.2006.01030.x

Akedo, J. (2008). Room Temperature Impact Consolidation (RTIC) of Fine Ceramic Powder by Aerosol Deposition Method and Applications to Microdevices. *Journal of Thermal Spray Technology, 17*(2), 181-198. doi:10.1007/s11666-008-9163-7

Akedo, J., & Lebedev, M. (1999). Microstructure and Electrical Properties of Lead Zirconate Titanate (Pb(Zr 52 /Ti 48)O 3) Thick Films Deposited by Aerosol Deposition Method. *Japanese Journal of Applied Physics, 38*(9S), 5397.

Almeida, J., Schobesberger, S., Kürten, A., Ortega, I. K., Kupiainen-Määttä, O., Praplan, A. P., . . . Kirkby, J. (2013). Molecular understanding of sulphuric acid–amine particle nucleation in the atmosphere. *Nature, 502*, 359. doi:10.1038/nature12663

Amelynck, C., Schoon, N., Kuppens, T., Bultinck, P., & Arijs, E. (2005). A selected ion flow tube study of the reactions of H3O+, NO+ and O2+ with some oxygenated biogenic volatile organic compounds. *International Journal of Mass Spectrometry, 247*(1), 1-9. doi:10.1016/j.ijms.2005.08.010

Assadi, H., Gärtner, F., Stoltenhoff, T., & Kreye, H. (2003). Bonding mechanism in cold gas spraying. *Acta Materialia, 51*(15), 4379-4394. doi:10.1016/S1359-6454(03)00274-X

Assadi, H., Schmidt, T., Richter, H., Kliemann, J.-O., Binder, K., Gärtner, F., . . . Kreye, H. (2011). On Parameter Selection in Cold Spraying. *Journal of Thermal Spray Technology, 20*(6), 1161-1176. doi:10.1007/s11666-011-9662-9

Baasandorj, M., Millet, D., Hu, L., Mitroo, D., & Williams, B. (2015). Measuring acetic and formic acid by proton-transfer-reaction mass spectrometry: sensitivity, humidity dependence, and quantifying interferences. *Atmospheric Measurement Techniques, 8*(3), 1303-1321.

Bailey, A. B., & Hiatt, J. (1971). *Free-flight measurements of sphere drag at subsonic, transonic, supersonic, and hypersonic speeds for continuum, transition, and near-free-molecular flow conditions*. Retrieved from

Balabel, A., Hegab, A. M., Nasr, M., & El-Behery, S. M. (2011). Assessment of turbulence modeling for gas flow in two-dimensional convergent–divergent rocket nozzle. *Applied Mathematical Modelling, 35*(7), 3408-3422. doi:10.1016/j.apm.2011.01.013

Banday, K. M., Pasikanti, K. K., Chan, E. C. Y., Singla, R., Rao, K. V. S., Chauhan, V. S., & Nanda, R. K. (2011). Use of Urine Volatile Organic Compounds To Discriminate Tuberculosis Patients from Healthy Subjects. *Analytical Chemistry, 83*(14), 5526-5534. doi:10.1021/ac200265g

Barash, O., Peled, N., Hirsch, F. R., & Haick, H. (2009). Sniffing the Unique "Odor Print" of Non-Small-Cell Lung Cancer with Gold Nanoparticles. *Small, 5*(22), 2618-2624. doi:10.1002/smll.200900937

Barash, O., Peled, N., Tisch, U., Bunn, P. A., Hirsch, F. R., & Haick, H. (2012). Classification of lung cancer histology by gold nanoparticle sensors. *Nanomedicine : nanotechnology, biology, and medicine, 8*(5), 580-589. doi:10.1016/j.nano.2011.10.001

Barsanti, K. C., McMurry, P. H., & Smith, J. N. (2009). The potential contribution of organic salts to new particle growth. *Atmos. Chem. Phys., 9*(9), 2949-2957. doi:10.5194/acp-9-2949-2009

Bartolazzi, A., Santonico, M., Pennazza, G., Martinelli, E., Paolesse, R., D'Amico, A., & Di Natale, C. (2010). A sensor array and GC study about VOCs and cancer cells. *Sensors and Actuators B: Chemical, 146*(2), 483-488. doi:10.1016/j.snb.2009.11.046

Boyd, I. D., & Schwartzentruber, T. E. (2017). *Nonequilibrium Gas Dynamics and Molecular Simulation*: Cambridge University Press.

Brunner, C., Szymczak, W., Höllriegl, V., Mörtl, S., Oelmez, H., Bergner, A., . . . Oeh, U. (2010). Discrimination of cancerous and non-cancerous cell lines by headspace-analysis with PTR-MS. *Analytical and Bioanalytical Chemistry, 397*(6), 2315-2324. doi:10.1007/s00216-010-3838-x

Buhr, K., van Ruth, S., & Delahunty, C. (2002). Analysis of volatile flavour compounds by Proton Transfer Reaction-Mass Spectrometry: fragmentation patterns and discrimination between isobaric and isomeric compounds. *International Journal of Mass Spectrometry, 221*(1), 1-7. doi:10.1016/S1387-3806(02)00896-5

Chakrabarty, S., Ferreiro, J. J., Lippe, M., & Signorell, R. (2017). Toluene Cluster Formation in Laval Expansions: Nucleation and Growth. *The Journal of Physical Chemistry A, 121*(20), 3991-4001. doi:10.1021/acs.jpca.7b03162

Champagne, V. K., Helfritch, D. J., Dinavahi, S. P. G., & Leyman, P. F. (2011). Theoretical and Experimental Particle Velocity in Cold Spray. *Journal of Thermal Spray Technology, 20*(3), 425-431. doi:10.1007/s11666-010-9530-z

Chan, T. W., & Mozurkewich, M. (2001). Measurement of the coagulation rate constant for sulfuric acid particles as a function of particle size using tandem differential mobility analysis. *Journal of Aerosol Science, 32*(3), 321-339. doi:10.1016/S0021-8502(00)00081-1

Chen, Y., Zhang, Y., Pan, F., Liu, J., Wang, K., Zhang, C., . . . Cui, D. (2016). Breath Analysis Based on Surface-Enhanced Raman Scattering Sensors Distinguishes Early and Advanced Gastric Cancer Patients from Healthy Persons. *ACS Nano, 10*(9), 8169-8179. doi:10.1021/acsnano.6b01441

Clark, W. E. (1972). *Measurements of aerosols produced by the photochemical oxidation of SO_2 in air.* (Ph.D.), University of Minnesota, Minneapolis, MN.

Clark, W. E., & Whitby, K. T. (1975). Measurements of Aerosols Produced by the Photochemical Oxidation of SO_2 in Air. *Journal of Colloid and Interface Science, 51*, 477-490.

Crump, J. G., & Seinfeld, J. H. (1981). Turbulent deposition and gravitational sedimentation of an aerosol in a vessel of abritrary shape. *J. Aerosol Sci., 12*(5), 405-415.

Davies, C. N. (1945). Definitive equations for the fluid resistance of spheres. *Proceedings of the Physical Society, 57*(4), 259.

Davis, J., Ravindran, P., & Ray, A. K. (1981). Single aerosol particle studies. *Advances in Colloid and Interface Sciences, 15*, 1-24. doi:10.1016/0001-8686(81)80001-2 de Juan, L., & Fernandez de la Mora, J. (1998). Sizing nanoparticles with a focusing impactor: Effect of the collector size. *Journal of Aerosol Science, 29*(5-6), 589-599.

Di Natale, C., Macagnano, A., Martinelli, E., Paolesse, R., D'Arcangelo, G., Roscioni, C., . . . D'Amico, A. (2003). Lung cancer identification by the analysis of breath by means of an array of non-selective gas sensors. *Biosens Bioelectron, 18*. doi:10.1016/s0956-5663(03)00086-1

Ding, H., Wang, C., & Wang, G. (2017). Transient conjugate heat transfer in critical flow nozzles. *International Journal of Heat and Mass Transfer, 104*, 930-942. doi:10.1016/j.ijheatmasstransfer.2016.09.021

Dugourd, P., Hudgins, R. R., & Jarrold, M. F. (1997). High-resolution ion mobility studies of sodium chloride nanocrystals. *Chemical Physics Letters, 267*(1-2), 186-192. doi:10.1016/s0009-2614(97)00062-6

Fernandez de la Mora, J., Hering, S. V., Rao, N., & McMurry, P. H. (1990). Hypersonic Impaction of Ultrafine Particles. *Journal of Aerosol Science, 21*(2), 169-187.

Fernández de la Mora, J., Rao, N., & McMurry, P. H. (1990). Inertial impaction of fine particles at moderate reynolds numbers and in the transonic regime with a thin-plate orifice nozzle. *Journal of Aerosol Science, 21*(7), 889-909. doi:10.1016/0021-8502(90)90160-Y

Filipiak, W., Sponring, A., Mikoviny, T., Ager, C., Schubert, J., Miekisch, W., . . . Troppmair, J. (2008). Release of volatile organic compounds (VOCs) from the lung cancer cell line CALU-1 in vitro. *Cancer Cell Int, 8*. doi:10.1186/1475-2867-8-17

Fluent, A. (2009). 12.0 User's guide. *Ansys Inc*.

Friedlander, S. K. (2000). *Smoke, dust, and haze : fundamentals of aerosol dynamics* (2nd ed.. ed.). New York: New York : Oxford University Press.

Fuchs, N. A. (1964). *The Mechanics of Aerosols*. Oxford: Pergamon Press.

Fuchs, N. A., & Sutugin, A. (1971). High dispersed aerosols. In G. M. Hidy & J. R. Brock (Eds.), *Topics in Current Aerosol Research (Part 2)* (pp. 1-60). New York: Pergamon.

Fuchs, N. A., & Sutugin, A. G. (1971). HIGH-DISPERSED AEROSOLS A2 - HIDY, G.M. In J. R. Brock (Ed.), *Topics in Current Aerosol Research* (pp. 1): Pergamon.

Gamero-Castano, M., & Fernandez de la Mora, J. (2000). A condensation nucleus counter (CNC) sensitive to singly charged sub-nanometer particles. *Journal of Aerosol Science, 31*(7), 757-772. doi:10.1016/s0021-8502(99)00555-8

Gelbard, F., & Seinfeld, J. H. (1979). The general dynamic equation for aerosols. Theory and application to aerosol formation and growth. *Journal of Colloid and Interface Science, 68*(2), 363-382. doi:10.1016/0021-9797(79)90289-3

Gelbard, F., & Seinfeld, J. H. (1980). Simulation of multicomponent aerosol dynamics. *Journal of Colloid and Interface Science, 78*(2), 485-501. doi:10.1016/0021-9797(80)90587-1

Goldstein, S. (1938). *Modern developments in fluid dynamics: an account of theory and experiment relating to boundary layers, turbulent motion and wakes* (Vol. 1): Clarendon Press.

Gopalakrishnan, R., & Hogan Jr., C. J. (2011). Determination of the transition Regime Collision Kernel from Mean First Passage Times. *Aerosol Science and Technology, 45*(12), 1499-1509. doi:10.1080/02786826.2011.601775

Haick, H., Broza, Y. Y., Mochalski, P., Ruzsanyi, V., & Amann, A. (2014). Assessment, origin, and implementation of breath volatile cancer markers. *Chemical Society Reviews, 43*(5), 1423-1449. doi:10.1039/c3cs60329f

Hakim, M., Broza, Y. Y., Barash, O., Peled, N., Phillips, M., Amann, A., & Haick, H. (2012). Volatile Organic Compounds of Lung Cancer and Possible Biochemical Pathways. *Chemical Reviews, 112*(11), 5949-5966. doi:10.1021/cr300174a

Hamid, A. M., Jarmusch, A. K., Pirro, V., Pincus, D. H., Clay, B. G., Gervasi, G., & Cooks, R. G. (2014). Rapid Discrimination of Bacteria by Paper Spray Mass Spectrometry. *Analytical Chemistry, 86*(15), 7500-7507. doi:10.1021/ac501254b

Hanft, D., Exner, J., Schubert, M., Stocker, T., Fuierer, P., & Moos, R. (2015). An Overview of the Aerosol Deposition Method: Process Fundamentals and New Trends in Materials Applications. *Journal of Ceramic Science and Technology, 6*(3), 147-181. doi:10.4416/jcst2015-00018

Haynes, B. S., & Wagner, H. G. (1981). Soot formation. *Progress in Energy and Combustion Science, 7*(4), 229-273. doi:10.1016/0360-1285(81)90001-0

Heisler, S. L., & Friedlander, S. K. (1977). Gas-to-particle conversion in photochemical smog: Aerosol growth laws and mechanisms for organics. *Atmospheric Environment (1967), 11*(2), 157-168. doi:10.1016/0004-6981(77)90220-7

Henderson, C. B. (1976). Drag Coefficients of Spheres in Continuum and Rarefied Flows. *AIAA Journal, 14*(6), 707-708. doi:10.2514/3.61409

Hodshire, A. L., Lawler, M. J., Zhao, J., Ortega, J., Jen, C., Yli-Juuti, T., . . . Pierce, J. R. (2016). Multiple new-particle growth pathways observed at the US DOE Southern Great Plains field site. *Atmos. Chem. Phys., 16*(14), 9321-9348. doi:10.5194/acp-16-9321-2016

Hogan, C. J., & Fernandez de la Mora, J. (2009). Tandem ion mobility-mass spectrometry (IMS-MS) study of ion evaporation from ionic liquid-acetonitrile nanodrops. *Physical Chemistry Chemical Physics, 11*(36), 8079-8090. doi:Doi 10.1039/B904022f

Hogan, C. J., & Fernandez de la Mora, J. (2010). Ion-Pair Evaporation from Ionic Liquid Clusters. *Journal of the American Society for Mass Spectrometry, 21*(8), 1382-1386. doi:DOI 10.1016/j.jasms.2010.03.044

Holman, Z. C., & Kortshagen, U. R. (2010). A flexible method for depositing dense nanocrystal thin films: impaction of germanium nanocrystals. *Nanotechnology, 21*(33), 335302.

Huang, C., Nichols, W. T., O'Brien, D. T., Becker, M. F., Kovar, D., & Keto, J. W. (2007). Supersonic jet deposition of silver nanoparticle aerosols: Correlations of impact conditions and film morphologies. *Journal of Applied Physics, 101*(6), 064902. doi:10.1063/1.2710304

Huang, G., Gu, D., Li, X., Xing, L., & Wang, H. (2014). Numerical simulation on syphonage effect of laval nozzle for low pressure cold spray system. *Journal of Materials Processing Technology, 214*(11), 2497-2504. doi:10.1016/j.jmatprotec.2014.05.014

Iida, K., Stolzenburg, M. R., & McMurry, P. H. (2009). Effect of working fluid on sub-2 nm particle detection with a laminar flow ultrafine condensation particle counter. *Aerosol Science and Technology, 43*, 81-96.

Iida, K., Stolzenburg, M. R., McMurry, P. H., Smith, J. N., Quant, F. R., Oberreit, D. R., . . . Hering, S. V. (2008). An ultrafine, water-based condensation particle counter and its evaluation under field conditions. *Aerosol Science and Technology, 42*(10), 862-871. doi:10.1080/02786820802339579

Jayne, J. T., Leard, D. C., Zhang, X., Davidovits, P., Smith, K. A., Kolb, C. E., & Worsnop, D. R. (2000). Development of an Aerosol Mass Spectrometer for Size and Composition Analysis of Submicron Particles. *Aerosol Science and Technology, 33*(1-2), 49-70. doi:10.1080/027868200410840

Jen, C., McMurry, P. H., & Hanson, D. R. (2014). Stabilization of Sulfuric Acid Dimers by Ammonia, Methylamine, Dimethylamine, and Trimethylamine. *Journal of geophysical research, 119*, 7502-7514. doi:10.1002/2014JD021592

Jeon, S., Oberreit, D. R., Van Schooneveld, G., Gao, Z., Bischof, J. C., Haynes, C. L., & Hogan, C. J. (2016). Ion-Mobility-Based Quantification of Surface-Coating-Dependent Binding of Serum Albumin to Superparamagnetic Iron Oxide Nanoparticles. *ACS Applied Materials & Interfaces, 8*(37), 24482-24490. doi:10.1021/acsami.6b09070

Jeon, S., Oberreit, D. R., Van Schooneveld, G., & Hogan, C. J. (2016). Liquid Nebulization-Ion Mobility Spectrometry Based Quantification of Nanoparticle-Protein Conjugate Formation. *Analytical Chemistry, 88*, 7667–7674.

Johnson, S. D., Schwer, D., Park, D.-S., Park, Y.-S., & Gorzkowski, E. P. (2017). Deposition efficiency of barium hexaferrite by aerosol deposition. *Surface and Coatings Technology, 332*(Supplement C), 542-549. doi:10.1016/j.surfcoat.2017.06.085

Jun, A., & Maxim, L. (2002). Powder Preparation in Aerosol Deposition Method for Lead Zirconate Titanate Thick Films. *Japanese Journal of Applied Physics, 41*(11S), 6980.

Kangasluoma, J., Attoui, M., Korhonen, F., Ahonen, L., Siivola, E., & Petaja, T. (2016). Characterization of a Herrmann-type high-resolution differential mobility analyzer. *Aerosol Science and Technology, 50*(3), 222-229. doi:10.1080/02786826.2016.1142065

Kangasluoma, J., Samodurov, A., Attoui, M., Franchin, A., Junninen, H., Korhonen, F., . . . Kulmala, M. (2016). Heterogeneous Nucleation onto Ions and Neutralized Ions: Insights into Sign-Preference. *Journal of Physical Chemistry C, 120*(13), 7444-7450. doi:10.1021/acs.jpcc.6b01779

Katanoda, H., Fukuhara, M., & Iino, N. (2007). Numerical Study of Combination Parameters for Particle Impact Velocity and Temperature in Cold Spray. *Journal of Thermal Spray Technology, 16*(5), 627-633. doi:10.1007/s11666-007-9087-7

Kerminen, V. M., & Kulmala, M. (2002). Analytical formulae connecting the "real" and the "apparent" nucleation rate and the nuclei number concentration for atmospheric nucleation events. *Journal of Aerosol Science, 33*(4), 609-622.

Kim, J. H., Mulholland, G. W., Kukuck, S. R., & Pui, D. Y. H. (2005). Slip correction measurements of certified PSL nanoparticles using a nanometer differential mobility analyzer (nano-DMA) for Knudsen number from 0.5 to 83. *Journal of Research of the National Institute of Standards and Technology, 110*(1), 31-54.

Kirkby, J. (2011). Role of sulphuric acid, ammonia and galactic cosmic rays in atmospheric aerosol nucleation. *Nature, 476*, 429-433.

Kirkby, J., Duplissy, J., Sengupta, K., Frege, C., Gordon, H., Williamson, C., . . . Curtius, J. (2016). Ion-induced nucleation of pure biogenic particles. *Nature*. doi:10.1038/nature17953

Koirala, R., Pratsinis, S. E., & Baiker, A. (2016). Synthesis of Catalytic Materials in Flames: Opportunities and Challenges. *Chem. Soc. Rev., 45*, 3053-3068. doi:10.1039/c5cs00011d

Kontkanen, J., Olenius, T., Lehtipalo, K., Vehkamäki, H., Kulmala, M., & Lehtinen, K. E. J. (2016). Growth of atmospheric clusters involving cluster–cluster collisions: comparison of different growth rate methods. *Atmos. Chem. Phys., 16*(9), 5545-5560. doi:10.5194/acp-16-5545-2016

Konvalina, G., & Haick, H. (2014). Sensors for Breath Testing: From Nanomaterials to Comprehensive Disease Detection. *Accounts of Chemical Research, 47*(1), 66-76. doi:10.1021/ar400070m

Kuang, C., Chen, M., McMurry, P. H., & Wang, J. (2012). Modification of Laminar Flow Ultrafine Condensation Particle Counters for the Enhanced Detection of 1 nm Condensation Nuclei. *Aerosol Science and Technology, 46*(3), 309-315. doi:10.1080/02786826.2011.626815

Kuang, C., Chen, M., Zhao, J., Smith, J., McMurry, P. H., & Wang, J. (2012). Size and time-resolved growth rate measurements of 1 to 5 nm freshly formed atmospheric nuclei. *Atmos. Chem. Phys., 12*(7), 3573-3589. doi:10.5194/acp-12-3573-2012

Kuang, C., McMurry, P. H., McCormick, A. V., & Eisele, F. L. (2008). Dependence of nucleation rates on sulfuric acid vapor concentration in diverse atmospheric locations. *Journal of Geophysical Research-Atmospheres, 113*(D10), D10209. doi:10.1029/2007JD009253

Kuang, C., Riipinen, I., Sihto, S.-L., Kulmala, M., McCormick, A. V., & McMurry, P. H. (2010). An improved criterion for new particle formation in diverse atmospheric environments. *Atmospheric Chemistry and Physics, 10*(17), 8469-8480. doi:10.5194/acp-10-8469-2010

Kuang, C., Riipinen, I., Yli-Juuti, T., Kulmala, M., McCormick, A. V., & McMurry, P. H. (2010). An improved criterion for new particle formation in diverse atmospheric environments. *Atmospheric Chemistry and Physics, 10*, 1-12. doi:10.5194/acp-10-1-2010

Kulmala, M., Kerminen, V. M., Anttila, T., Laaksonen, A., & O'Dowd, C. D. (2004). Organic aerosol formation via sulphate cluster activation. *Journal of Geophysical Research-Atmospheres, 109*(D4). doi:10.1029/2003jd003961

Kulmala, M., Lehtinen, K. E. J., & Laaksonen, A. (2006). Cluster activation theory as an explanation of the linear dependence between formation rate of 3nm particles and sulphuric acid concentration. *Atmos. Chem. Phys., 6*(3), 787-793. doi:10.5194/acp-6-787-2006

Kulmala, M., Petäjä, T., Nieminen, T., Sipilä, M., Manninen, H. E., Lehtipalo, K., . . . Kerminen, V.-M. (2012). Measurement of the nucleation of atmospheric aerosol particles. *Nature Protocols, 7*, 1651. doi:10.1038/nprot.2012.091

Kumar, S., Huang, J., Abbassi-Ghadi, N., Mackenzie, H. A., Veselkov, K. A., Hoare, J. M., . . . Hanna, G. B. (2015). Mass Spectrometric Analysis of Exhaled Breath for the Identification of Volatile Organic Compound Biomarkers in Esophageal and Gastric Adenocarcinoma. *Annals of Surgery, 262*(6), 981-990. doi:10.1097/sla.0000000000001101

Kürten, A., Jokinen, T., Simon, M., Sipilä, M., Sarnela, N., Junninen, H., . . . Curtius, J. (2014). Neutral molecular cluster formation of sulfuric acid–dimethylamine observed in real time under atmospheric conditions. *Proceedings of the National Academy of Sciences, 111*(42), 15019-15024. doi:doi/10.1073/pnas.1404853111

Kürten, A., Li, C., Bianchi, F., Curtius, J., Dias, A., Donahue, N. M., . . . McMurry, P. H. (2018). New particle formation in the sulfuric acid–dimethylamine–water system: reevaluation of CLOUD chamber measurements and comparison to an aerosol nucleation and growth model. *Atmos. Chem. Phys., 18*(2), 845-863. doi:10.5194/acp-18-845-2018

Larriba, C., & Hogan, C. J. (2013). Ion Mobilities in Diatomic Gases: Measurement vs. Prediction with Non-Specular Scattering Models. *The Journal of Physical Chemistry A, 117*, 3887-3901.

Lee, A., Goldstein Allen, H., Keywood Melita, D., Gao, S., Varutbangkul, V., Bahreini, R., . . . Seinfeld John, H. (2006). Gas-phase products and secondary aerosol yields from the ozonolysis of ten different terpenes. *Journal of Geophysical Research: Atmospheres, 111*, D07302. doi:10.1029/2005jd006437

Lee, M.-W., Park, J.-J., Kim, D.-Y., Yoon, S. S., Kim, H.-Y., James, S. C., . . . Coyle, T. (2011). Numerical Studies on the Effects of Stagnation Pressure and Temperature on Supersonic Flow Characteristics in Cold Spray Applications. *Journal of Thermal Spray Technology, 20*(5), 1085-1097. doi:10.1007/s11666-011-9641-1

Lee, M. W., Park, J. J., Kim, D. Y., Yoon, S. S., Kim, H. Y., Kim, D. H., . . . Park, D. S. (2011). Optimization of supersonic nozzle flow for titanium dioxide thin-film coating by aerosol deposition. *Journal of Aerosol Science, 42*(11), 771-780. doi:10.1016/j.jaerosci.2011.07.006

Lehtinen, K. E. J., & Kulmala, M. (2003). A model for particle formation and growth in the atmosphere with molecular resolution in size. *Atmos. Chem. Phys., 3*(1), 251-257. doi:10.5194/acp-3-251-2003

Lehtinen, K. E. J., Rannik, U., Petaja, T., Kulmala, M., & Hari, P. (2004). Nucleation rate and vapor concentration estimations using a least squares aerosol dynamics method - art. no. D21209. *Journal of Geophysical Research-Atmospheres, 109*(D21), 21209.

Lehtipalo , K., Leppa , J , Kontkanen , J , Kangasluoma , J , Franchin , A , Wimnner , D , Schobesberger , S , Junninen , H , Petaja , T , Sipila , M , Mikkila , J , Vanhanen , J , Worsnop , D R & Kulmala. (2014). Methods for determining particle size distribution and growth rates between 1 and 3 nm using the Particle Size Magnifier. *Boreal Environment Research, 19*(no. B), 215-236.

Lehtipalo, K., Rondo, L., Kontkanen, J., Schobesberger, S., Jokinen, T., Sarnela, N., . . . Kulmala, M. (2016). The effect of acid-base clustering and ions on the growth of atmospheric nano-particles. *Nature Communications, 7*, 11594.

Ligor, T., Ligor, M., Amann, A., Ager, C., Bachler, M., Dzien, A., & Buszewski, B. (2008). The analysis of healthy volunteers' exhaled breath by the use of solid-phase microextraction and GC-MS. *J Breath Research, 2*. doi:10.1088/1752-7155/2/4/046006

Lindinger, W., Hansel, A., & Jordan, A. (1998). Proton-transfer-reaction mass spectrometry (PTR-MS): on-line monitoring of volatile organic compunds at pptv levels. *Chem Soc Rev, 27*. doi:10.1039/a827347z

Lindquist, G. J., Pui, D. Y. H., & Hogan Jr, C. J. (2014). Porous particulate film deposition in the transition regime. *Journal of Aerosol Science, 74*(0), 42-51. doi:10.1016/j.jaerosci.2014.03.007

Liu, P., Ziemann, P. J., Kittelson, D. B., & McMurry, P. H. (1995). Generating Particle Beams of Controlled Dimensions and Divergence: I. Theory of Particle Motion in Aerodynamic Lenses and Nozzle Expansions. *Aerosol Science and Technology, 22*(3), 293-313. doi:10.1080/02786829408959748

Lushnikov, A. A., & Kulmala, M. (1995). Source-Enhanced Condensation in Monocomponent Disperse Systems. *Physical Review E, 52*(2), 1658-1668.

Machado, R. F., Laskowski, D., Deffenderfer, O., Burch, T., Zheng, S., Mazzone, P. J., . . . Pyle, J. (2005). Detection of lung cancer by sensor array analyses of exhaled breath. *Am J Respir Crit Care Med, 171*. doi:10.1164/rccm.200409-1184OC

Macrossan, M. N. (2006). *Scaling Parameters for Hypersonic Flow: Correlation of Sphere Drag Data*. Paper presented at the 25th International Symposium on Rarefied Gas Dynamics
, St. Petersburg, Russia.

Maisser, A., Thomas, J. M., Larriba-Andaluz, C., He, S., & Hogan, C. J. (2015). The Mass-Mobility Distributions of Ions Produced by a Po-210 Source in Air. *Journal of Aerosol Science, 90*, 36-50.

Mallina, R. V., Wexler, A. S., Rhoads, K. P., & Johnston, M. V. (2000). High Speed Particle Beam Generation: A Dynamic Focusing Mechanism for Selecting Ultrafine Particles. *Aerosol Science and Technology, 33*(1-2), 87-104. doi:10.1080/027868200410868

Marple, V. A., & Willeke, K. (1976). Impactor Design. *Atmospheric Environment, 10*, 891-896.

Mazzone, P. J., Hammel, J., Dweik, R., Na, J., Czich, C., Laskowski, D., & Mekhail, T. (2007). Diagnosis of lung cancer by the analysis of exhaled breath with a colorimetric sensor array. *Thorax, 62*(7), 565-568. doi:10.1136/thx.2006.072892

McGrath, M. J., Olenius, T., Ortega, I. K., Loukonen, V., Paasonen, P., Kurtén, T., . . . Vehkamäki, H. (2012). Atmospheric cluster dynamics code: a flexible method for solution of the birth-death equations. *Atmos. Chem. Phys., 12*, 2345-2355. doi:10.5194/acp-12-2345-2012

McMurry, P. H. (1980). Photochemical aerosol formation from SO2: A theoretical analysis of smog chamber data. *Journal of Colloid and Interface Science, 78*(2), 513-527. doi:10.1016/0021-9797(80)90589-5

McMurry, P. H. (1983). New Particle Formation in the Presence of an Aerosol: Rates, Time Scales and sub-0.01 µm Size Distributions. *Journal of Colloid and Interface Science, 95*(1), 72-80.

McMurry, P. H. (2000). The history of condensation nucleus counters. *Aerosol Science and Technology, 33*(4), 297-322.

McMurry, P. H., Fink, M. A., Sakurai, H., Stolzenburg, M. R., Mauldin, L., Moore, K., . . . Voisin, D. (2005). A Criterion for New Particle Formation in the Sulfur-Rich Atlanta Atmosphere. *Journal of Geophysical Research - Atmospheres, 110*, D22S02. doi:10.1029/2005JD005901

McMurry, P. H., & Friedlander, S. K. (1979). New particle formation in the presence of an aerosol. *Atmos. Environ., 13*, 1635-1651.

McMurry, P. H., & Li, C. (2017). The dynamic behavior of nucleating aerosols in constant reaction rate systems: Dimensional analysis and generic numerical solutions. *Aerosol Science and Technology, 51*(9), 1057-1070. doi:10.1080/02786826.2017.1331292

McMurry, P. H., & Rader, D. J. (1985). Aerosol wall losses in electrically charged chambers. *Aerosol Sci. and Technol., 4*, 249-268.

McMurry, P. H., & Wilson, J. C. (1982). Growth laws for the formation of secondary ambient aerosols: Implications for chemical conversion mechanisms. *Atmospheric Environment (1967), 16*(1), 121-134. doi:10.1016/0004-6981(82)90319-5

Menter, F. R. (1994). Two-equation eddy-viscosity turbulence models for engineering applications. *AIAA Journal, 32*(8), 1598-1605. doi:10.2514/3.12149

Meyer, N. A., Root, K., Zenobi, R., & Vidal-de-Miguel, G. (2016). Gas-Phase Dopant-Induced Conformational Changes Monitored with Transversal Modulation Ion Mobility Spectrometry. *Analytical Chemistry, 88*(4), 2033-2040. doi:10.1021/acs.analchem.5b02750

Middha, P., & Wexler, A. S. (2003). Particle Focusing Characteristics of Sonic Jets. *Aerosol Science and Technology, 37*(11), 907-915. doi:10.1080/02786820300934

Millikan, R. A. (1923). Coefficients of Slip in Gases and the Law of Reflection of Molecules from the Surfaces of Solids and Liquids. *Physical Review, 21*(3), 217-238.

Muneyasu, S., Tetsuo, T., & Jun, A. (2017). Effect of starting powder morphology on film texture for bismuth layer-structured ferroelectrics prepared by aerosol deposition method. *Japanese Journal of Applied Physics, 56*(6S1), 06GH02.

Nakhleh, M. K., Amal, H., Jeries, R., Broza, Y. Y., Aboud, M., Gharra, A., . . . Haick, H. (2017). Diagnosis and Classification of 17 Diseases from 1404 Subjects via Pattern Analysis of Exhaled Molecules. *ACS Nano, 11*(1), 112-125. doi:10.1021/acsnano.6b04930

Ning, X.-J., Wang, Q.-S., Ma, Z., & Kim, H.-J. (2010). Numerical Study of In-flight Particle Parameters in Low-Pressure Cold Spray Process. *Journal of Thermal Spray Technology, 19*(6), 1211-1217. doi:10.1007/s11666-010-9548-2

Oberreit, D., Rawat, V. K., Larriba-Andaluz, C., Ouyang, H., McMurry, P. H., & Jr., C. J. H. (2015). Analysis of heterogeneous water vapor uptake by metal iodide cluster ions via differential mobility analysis-mass spectrometry. *The Journal of Chemical Physics, 143*(10), 104204. doi:10.1063/1.4930278

Oberreit, D. R., McMurry, P. H., & Hogan, C. J. (2014). Analysis of Heterogeneous Vapor Uptake by Nanoparticles via Differential Mobility Analysis-Drift Tube Ion Mobility Spectrometry (DMA-DTIMS). *Phys Chem Chem Phys, 16*, 6968-6979.

Oberreit, D. R., Rawat, V. K., Larriba-Andaluz, C., Ouyang, H., McMurry, P. H., & Hogan, C. J. (2015). Analysis of heterogeneous water vapor uptake by metal iodide cluster ions via differential mobility analysis-mass spectrometry. *The Journal of Chemical Physics, 143*, 104204.

Olenius, T., Riipinen, I., Lehtipalo, K., & Vehkamäki, H. (2014). Growth rates of atmospheric molecular clusters based on appearance times and collision–evaporation fluxes: Growth by monomers. *Journal of Aerosol Science, 78*, 55-70. doi:10.1016/j.jaerosci.2014.08.008

Ouyang, H., Larriba-Andaluz, C., Oberreit, D. R., & Hogan, C. J. (2013). The Collision Cross Sections of Iodide Salt Cluster Ions in Air via Differential Mobility Analysis-Mass Spectrometry *Journal of the American Society for Mass Spectrometry, 24*, 1833-1847. doi:10.1007/s13361-013-0724-8

Park, J.-J., Kim, D.-Y., Lee, J.-G., Cha, Y.-H., Swihart, M. T., & Yoon, S. S. (2014). Supersonic aerosol-deposited TiO2 photoelectrodes for photoelectrochemical solar water splitting. *RSC Advances, 4*(17), 8661-8670. doi:10.1039/c3ra47998f

Park, J.-J., Lee, J.-G., Kim, D.-Y., Lee, J.-H., Yun, J. H., Gwak, J., . . . Yoon, S. S. (2017). Rapid supersonic spraying of Cu(In,Ga)(S,Se)2 nanoparticles to fabricate a solar cell with 5.49% conversion efficiency. *Acta Materialia, 123*, 44-54. doi:10.1016/j.actamat.2016.10.027

Patrik, Š., & David, S. (2008). Quantification of trace levels of the potential cancer biomarkers formaldehyde, acetaldehyde and propanol in breath by SIFT-MS. *Journal of Breath Research, 2*(4), 046003.

Patterson, G. N. (1971). *Introduction to the kinetic theory of gas flows*: University of Toronto Press.

Pedregosa, F., Ga, #235, Varoquaux, l., Gramfort, A., Michel, V., . . . Duchesnay, d. (2011). Scikit-learn: Machine Learning in Python. *J. Mach. Learn. Res., 12*, 2825-2830.

Peng, G., Hakim, M., Broza, Y. Y., Billan, S., Abdah-Bortnyak, R., Kuten, A., . . . Haick, H. (2010). Detection of lung, breast, colorectal, and prostate cancers from exhaled breath using a single array of nanosensors. *British Journal Of Cancer, 103*, 542. doi:10.1038/sj.bjc.6605810

Peng, G., Tisch, U., Adams, O., Hakim, M., Shehada, N., Broza, Y. Y., . . . Haick, H. (2009). Diagnosing lung cancer in exhaled breath using gold nanoparticles. *Nature Nanotechnology, 4*, 669. doi:10.1038/nnano.2009.235

Peng, G., Tisch, U., & Haick, H. (2009). Detection of Nonpolar Molecules by Means of Carrier Scattering in Random Networks of Carbon Nanotubes: Toward Diagnosis of Diseases via Breath Samples. *Nano Letters, 9*(4), 1362-1368. doi:10.1021/nl8030218

Pichelstorfer, L., Stolzenburg, D., Ortega, J., Karl, T., Kokkola, H., Laakso, A., . . . Winkler, P. M. (2017). Resolving nanoparticle growth mechanisms from size- and time-dependent growth rate analysis. *Atmos. Chem. Phys. Discuss., 2017*, 1-24. doi:10.5194/acp-2017-658

Rao, N. P., & McMurry, P. H. (1989). Nucleation and Growth of Aerosol in Chemically Reacting Systems: A Theoretical Study of the Near-Collision-Controlled Regime. *Aerosol Science and Technology, 11*(2), 120-132. doi:10.1080/02786828908959305

Rao, N. P., Tymiak, N., Blum, J., Neuman, A., Lee, H. J., Girshick, S. L., . . . Heberlein, J. (1998). Hypersonic plasma particle deposition of nanostructured silicon and silicon carbide. *Journal of Aerosol Science, 29*(5), 707-720. doi:10.1016/S0021-8502(97)10015-5

Rawat, V. K., Vidal-de-Miguel, G., & Hogan, C. J. (2015). Modeling vapor uptake induced mobility shifts in peptide ions observed with transversal modulation ion mobility spectrometry-mass spectrometry. *Analyst, 140*(20), 6945-6954. doi:10.1039/c5an00753d

Riccobono, F. (2012). Contribution of sulfuric acid and oxidized organic compounds to particle formation and growth. *Atmos. Chem. Phys., 12*, 9427-9439.

Riccobono, F. (2014). Oxidation products of biogenic emissions contribute to nucleation of atmospheric particles. *Science, 344*, 717-721.

Riipinen, I., Sihto, S.-L., Kulmala, M., Arnold, F., Dal Maso, M., Birmili, W., . . . Lehtinen, K. E. J. (2007). Connections between atmospheric sulphuric acid and new particle formation during QUEST III - IV campaigns in Hyytiala and Heidelberg. *Atmos. Phys. Chem., 7*, 1899–1914.

Riipinen, I., Yli-Juuti, T., Pierce, J. R., Petäjä, T., Worsnop, D. R., Kulmala, M., & Donahue, N. M. (2012). The contribution of organics to atmospheric nanoparticle growth. *Nature Geoscience, 5*, 453. doi:10.1038/ngeo1499

Röck, F., Barsan, N., & Weimar, U. (2008). Electronic Nose: Current Status and Future Trends. *Chemical Reviews, 108*(2), 705-725. doi:10.1021/cr068121q

Rogers, P. H., Benkstein, K. D., & Semancik, S. (2012). Machine Learning Applied to Chemical Analysis: Sensing Multiple Biomarkers in Simulated Breath Using a Temperature-Pulsed Electronic-Nose. *Analytical Chemistry, 84*(22), 9774-9781. doi:10.1021/ac301687j

Rus, J., Moro, D., Sillero, J. A., Royuela, J., Casado, A., Estevez-Molinero, F., & Fernandez de la Mora, J. (2010). IMS–MS studies based on coupling a differential mobility analyzer (DMA) to commercial API–MS systems. *International Journal of Mass Spectrometry, 298*, 30-40.

Saad, M. A. (1985). Compressible fluid flow. *Englewood Cliffs, NJ, Prentice-Hall, Inc., 1985. 570 p.*

Schmidt, K., & Podmore, I. (2015). Current Challenges in Volatile Organic Compounds Analysis as Potential Biomarkers of Cancer. *Journal of Biomarkers, 2015*, 16. doi:10.1155/2015/981458

Seinfeld, J. H., & Pandis, S. N. (2016). *Atmospheric Chemistry and Physics: From Air Pollution to Climate Change, 3rd Edition*. New York: Wiley Interscience.

Shiraiwa, M., Selzle, K., & Pöschl, U. (2012). Hazardous components and health effects of atmospheric aerosol particles: reactive oxygen species, soot, polycyclic aromatic compounds and allergenic proteins. *Free Radical Research, 46*(8), 927-939. doi:10.3109/10715762.2012.663084

Sihto, S. L., Kulmala, M., Kerminen, V. M., Dal Maso, M., Petaja, T., Riipinen, I., . . . Lehtinen, K. E. J. (2006). Atmospheric sulphuric acid and aerosol formation: implications from atmospheric measurements for nucleation and early growth mechanisms. *Atmospheric Chemistry and Physics, 6*, 4079-4091.

Singh, N., & Schwartzentruber, T. E. (2017). Aerothermodynamic correlations for high-speed flow. *Journal of Fluid Mechanics, 821*, 421-439. doi:10.1017/jfm.2017.195

Smith, D., & Spanel, P. (2005). Selected ion flow tube mass spectrometry (SIFT-MS) for on-line trace gas analysis. *Mass Spectrometry Reviews, 24*. doi:10.1002/mas.20033

Smith, J., Dunn, M., VanReken, T., Iida, K., Stolzenburg, M., McMurry, P., & Huey, L. (2008). Chemical composition of atmospheric nanoparticles formed from nucleation in Tecamac, Mexico: Evidence for an important role for organic species in nanoparticle growth. *Geophysical Research Letters, 35*(4).

Smith, J. N., Barsanti, K. C., Friedli, H. R., Ehn, M., Kulmala, M., Collins, D. R., . . . McMurry, P. H. (2010). Observations of aminium salts in atmospheric nanoparticles and possible climatic implications. *Proceedings of the National Academy of Sciences, 107*(15), 6634-6639.

Sponring, A., Filipiak, W., Mikoviny, T., Ager, C., Schubert, J., Miekisch, W., . . . Troppmair, J. (2009). Release of volatile organic compounds from the lung cancer cell line NCI-H2087 in vitro. *Anticancer Res, 29*.

Stalder, J. R., & Zurick, V. J. (1951). *Theoretical aerodynamic characteristics of bodies in a free-molecule-flow field*. Retrieved from

Steiner, G., & Reischl, G. P. (2012). The effect of carrier gas contaminants on the charging probability of aerosols under bipolar charging conditions. *Journal of Aerosol Science, 54*(0), 21-31. doi:10.1016/j.jaerosci.2012.07.008

Stoltenhoff, T., Kreye, H., & Richter, H. J. (2002). An analysis of the cold spray process and its coatings. *Journal of Thermal Spray Technology, 11*(4), 542-550. doi:10.1361/105996302770348682

Stolzenburg, M. R., & McMurry, P. H. (1991). An Ultrafine Aerosol Condensation Nucleus Counter. *Aerosol Science and Technology, 14*(1), 48-65.

Stolzenburg, M. R., McMurry, P. H., Sakurai, H., Smith, J. N., Mauldin, R. L., Eisele, F. L., & Clement, C. F. (2005). Growth rates of freshly nucleated atmospheric particles in Atlanta. *Journal of Geophysical Research: Atmospheres, 110*(D22), n/a-n/a. doi:10.1029/2005JD005935

Strobel, R., & Pratsinis, S. E. (2007). Flame aerosol synthesis of smart nanostructured materials. *Journal of Materials Chemistry, 17*(45), 4743-4756. doi:10.1039/B711652G

Sule-Suso, J., Pysanenko, A., Spanel, P., & Smith, D. (2009). Quantification of acetaldehyde and carbon dioxide in the headspace of malignant and non-malignant lung cellsin vitro by SIFT-MS. *Analyst, 134*(12), 2419-2425. doi:10.1039/B916158A

Swihart, M. T., & Girshick, S. L. (1999). Thermochemistry and kinetics of silicon hydride cluster formation during thermal decomposition of silane. *J. Phys. Chem., 103B*, 64-73.

Tali, F., Jens, H., Ingrid, K., Guy, L., John, C. C., Jose, S. T., . . . Nir, P. (2017). Cancer metabolism: the volatile signature of glycolysis— in vitro model in lung cancer cells. *Journal of Breath Research, 11*(1), 016008.

Tali, F., Layah, A.-M., Jens, H., John, C. C., Jose, S. T., Naomi Gai, M., . . . Nir, P. (2016). Cancerous glucose metabolism in lung cancer—evidence from exhaled breath analysis. *Journal of Breath Research, 10*(2), 026012.

Thimsen, E., Johnson, M., Zhang, X., Wagner, A. J., Mkhoyan, K. A., Kortshagen, U. R., & Aydil, E. S. (2014). High electron mobility in thin films formed via supersonic impact deposition of nanocrystals synthesized in nonthermal plasmas. *Nature Communications, 5*, 5822. doi:10.1038/ncomms6822

Thomas, J. M., He, S., Larriba-Andaluz, C., DePalma, J. W., Johnston, M., & Hogan, C. J. (2016). Ion Mobility Spectrometry-Mass Spectrometry Examination of the Structures, Stabilities, and Extents of Hydration of Dimethylamine-Sulfuric Acid Clusters. *Physical Chemistry Chemical Physics*, DOI: 10.1039/C1036CP03432B. doi:10.1039/c6cp03432b

Trimpin, S., & Clemmer, D. E. (2008). Ion Mobility Spectrometry/Mass Spectrometry Snapshots for Assessing the Molecular Compositions of Complex Polymeric Systems. *Analytical Chemistry, 80*(23), 9073-9083.

Tröstl, J., Chuang, W. K., Gordon, H., Heinritzi, M., Yan, C., Molteni, U., . . . Baltensperger, U. (2016). The role of low-volatility organic compounds in initial particle growth in the atmosphere. *Nature, 533*, 527. doi:10.1038/nature18271

Tuzson, B., Jágerská, J., Looser, H., Graf, M., Felder, F., Fill, M., . . . Emmenegger, L. (2017). Highly Selective Volatile Organic Compounds Breath Analysis Using a Broadly-Tunable Vertical-External-Cavity Surface-Emitting Laser. *Analytical Chemistry, 89*(12), 6377-6383.

Ude, S., & Fernandez de la Mora, J. (2005). Molecular monodisperse mobility and mass standards from electrosprays of tetra-alkyl ammonium halides. *Journal of Aerosol Science, 36*(10), 1224-1237. doi:10.1016/j.jaerosci.2005.02.009

Vanhanen, J., Mikkila, J., Lehtipalo, K., Sipila, M., Manninen, H. E., Siivola, E., . . . Kulmala, M. (2011). Particle Size Magnifier for Nano-CN Detection. *Aerosol Science and Technology, 45*(4), 533-542. doi:10.1080/02786826.2010.547889

Vergara, A., Benkstein, K. D., Montgomery, C. B., & Semancik, S. (2014). Demonstration of Fast and Accurate Discrimination and Quantification of Chemically Similar Species Utilizing a Single Cross-Selective Chemiresistor. *Analytical Chemistry, 86*(14), 6753-6757. doi:10.1021/ac501490k

Verheggen, B., & Mozurkewich, M. (2006). An inverse modeling procedure to determine particle growth and nucleation rates from measured aerosol size distributions. *Atmospheric Chemistry and Physics, 6*, 2927-2942.

Wang, J., McGraw, R. L., & Kuang, C. (2013). Growth of atmospheric nano-particles by heterogeneous nucleation of organic vapor. *Atmos. Chem. Phys., 13*(13), 6523-6531. doi:10.5194/acp-13-6523-2013

Wang, X. L., Kruis, F. E., & McMurry, P. H. (2005). Aerodynamic focusing of nanoparticles: I. Guidelines for designing aerodynamic lenses for nanoparticles. *Aerosol Science and Technology, 39*(7), 611-623.

Warneke, C., de Gouw, J. A., Kuster, W. C., Goldan, P. D., & Fall, R. (2003). Validation of Atmospheric VOC Measurements by Proton-Transfer- Reaction Mass Spectrometry Using a Gas-Chromatographic Preseparation Method. *Environmental Science & Technology, 37*(11), 2494-2501. doi:10.1021/es026266i

Warren, D. R., & Seinfeld, J. H. (1985). Simulation of Aerosol Size Distribution Evolution in Systems with Simultaneous Nucleation, Condensation, and Coagulation. *Aerosol Science and Technology, 4*(1), 31-43. doi:10.1080/02786828508959037

Weber, R. J., Marti, J., McMurry, P. H., Eisele, F. L., Tanner, D. J., & Jefferson, A. (1996). Measured atmospheric new particle formation rates: implications for nucleation mechanisms. *Chem. Eng. Comm., 151*, 53-64. doi:10.1080/00986449608936541

Weber, R. J., Marti, J. J., McMurry, P. H., Eisele, F. L., Tanner, D. J., & Jefferson, A. (1997). Measurements of new particle formation and ultrafine particle growth rates at a clean continental site. *Journal of Geophysical Research: Atmospheres, 102*(D4), 4375-4385. doi:10.1029/96JD03656

Wehinger, A., Schmid, A., Mechtcheriakov, S., Ledochowski, M., Grabmer, C., Gastl, G., & Amann, A. (2007). Lung cancer detection by proton transfer reaction mass spectrometric analysis of human breath gas. *Int J Mass Spec, 265*. doi:10.1016/j.ijms.2007.05.012

Whitby, K. T., & Clark , W. E. (1966). Electrical aerosol particle counting and size distribution measuring system for the 0.015 to 1.0 µm size range. *Tellus, 13*, 573-586.

Wimmer, D., Lehtipalo, K., Franchin, A., Kangasluoma, J., Kreissl, F., Kurten, A., . . . Curtius, J. (2013). Performance of diethylene glycol-based particle counters in the sub-3 nm size range. *Atmospheric Measurement Techniques, 6*(7), 1793-1804. doi:10.5194/amt-6-1793-2013

Wojciech, F., Anna, F., Andreas, S., Thomas, S., Bettina, Z., Clemens, A., . . . Anton, A. (2014). Comparative analyses of volatile organic compounds (VOCs) from patients, tumors and transformed cell lines for the validation of lung cancer-derived breath markers. *Journal of Breath Research, 8*(2), 027111. doi:10.1088/1752-7155/8/2/027111

Yin, S., Meyer, M., Li, W., Liao, H., & Lupoi, R. (2016). Gas Flow, Particle Acceleration, and Heat Transfer in Cold Spray: A review. *Journal of Thermal Spray Technology, 25*(5), 874-896. doi:10.1007/s11666-016-0406-8

Yli-Juuti, T. (2011). Growth rates of nucleation mode particles in Hyytiälä during 2003–2009: variation with particle size, season, data analysis method and ambient conditions. *Atmos. Chem. Phys., 11*, 12865-12886.

Yu, F. Q. (2005). Modified Kelvin-Thomson equation considering ion-dipole interaction: Comparison with observed ion-clustering enthalpies and entropies. *Journal of Chemical Physics, 122*(8), 084503. doi:10.1063/1.1845395

Yuan, B., Koss, A. R., Warneke, C., Coggon, M., Sekimoto, K., & de Gouw, J. A. (2017). Proton-Transfer-Reaction Mass Spectrometry: Applications in Atmospheric Sciences. *Chemical Reviews, 117*(21), 13187-13229. doi:10.1021/acs.chemrev.7b00325

Zarin, N. A. (1970). Measurement of non-continuum and turbulence effects on subsonic sphere drag.

Zhang, C., & Schwartzentruber, T. E. (2012). Robust cut-cell algorithms for DSMC implementations employing multi-level Cartesian grids. *Computers & Fluids, 69*, 122-135. doi:10.1016/j.compfluid.2012.08.013

Zhang, C. L., Thajudeen, T., Larriba, C., Schwartzentruber, T. E., & Hogan, C. J. (2012). Determination of the Scalar Friction Factor for Nonspherical Particles and Aggregates Across the Entire Knudsen Number Range by Direct Simulation Monte Carlo (DSMC). *Aerosol Science and Technology, 46*(10), 1065-1078. doi:10.1080/02786826.2012.690543

Ziegel, E. R. (2003). The Elements of Statistical Learning (Vol. 45, pp. 267-268): Taylor & Francis.

Appendix A: Evaluation of Coagulation Effects on Mode Diameter Growth

To evaluate the contribution of self-coagulation of the mode ($GR_{m,self}$) and cluster coagulation ($GR_{m,clsuter}$) to measured growth rate based on mode diameter ($GR_{m,mode}$), we used the following first order numerical approximation method:

1. Find particle size distribution $\tilde{n} = \tilde{n}(k,\tau)$ at a given time τ. k is the number of monomers in a particle and $\tilde{n}_k$ is the concentration of particles that contains k molecules. Since the simulation code only reports discrete particle concentration for each bin, an interpolation is performed using Matlab function *griddedInterpolant.m*.
2. Find the value $k = k_{max}$ at which $3\log(10)\,k\tilde{n}(k,\tau)$ is locally maximized. A prefactor $3\log(10)\,k$ is multiplied to $\tilde{n}(k,\tau)$ to convert the particle size distribution to $d\tilde{N}/dlog_{10}\tilde{d}_p$. The mode diameter is then given by $\tilde{d}_{p,mode}(\tau) = \left(\frac{6k_{max}}{\pi}\right)^{1/3}$.
3. Use the following integration equations to obtain number distribution of the mode at time $\tau + \Delta\tau$ assuming only one process causes the distribution to shift.

   For self-coagulation:

   $$\tilde{n}_{self}(k,\tau+\Delta\tau) = \tilde{n}(k) +$$

   $$0.5 * \Delta\tau * \int_L^k c(x,k-x)\tilde{n}(x,\tau)\tilde{n}(k-x,\tau)dx - \int_L^H c(x,k)\tilde{n}(k,\tau)\tilde{n}(x,\tau)dx. \quad \text{(A1)}$$

   For coagulation with clusters:

   $$\tilde{n}_{cluster}(k,\tau+\Delta\tau) = \tilde{n}(k,\tau) + 0.5\cdot\Delta\tau\cdot\int_{L_c}^{H_c} c(x,k-x)\tilde{n}(x,\tau)\tilde{n}(k-x,\tau)H(H_c-k+x)dx +$$

$$\Delta\tau \cdot \int_{L_c}^{H_c} c(x, k-x)\tilde{n}(x,\tau)\tilde{n}(k-x,\tau)H(k-x-H_c)dx + -\Delta\tau \cdot \int_{L_c}^{H_c} c(x,k)\tilde{n}(x,\tau)\tilde{n}(k,\tau)dx. \quad \text{(A2)}$$

In the above equations, L and H are the lower and upper boundary of the mode, L_c and H_c are the lower and upper boundary of clusters, $c(i,j)$ is the collision frequency function, *H(x)* is the Heaviside step function. $\Delta\tau$ is typically set between 0.1 to 1.

4. Find the k values at which the expressions $3\log(10)\, k\tilde{n}_{self}(k, \tau + \Delta\tau)$ and $3\log(10)\, k\tilde{n}_{cluster}(k, \tau + \Delta\tau)$ are locally maximized. The corresponding diameters are $\tilde{d}_{p,self}(\tau + \Delta\tau)$ and $\tilde{d}_{p,cluster}(\tau + \Delta\tau)$.
5. The growth rate due to self-coagulation and coagulation with clusters are then given by $GR_{m,self} = \frac{\tilde{d}_{p,self}(\tau+\Delta\tau) - \tilde{d}_{p,mode}(\tau)}{\Delta\tau}$; $GR_{m,cluster} = \frac{\tilde{d}_{p,cluster}(\tau+\Delta\tau) - \tilde{d}_{p,mode}(\tau)}{\Delta\tau}$.

Appendix B: Dimensional Particle Size Distribution

To facilitate comparison between dimensionless simulation results and experimental results, or previous dimensional simulation results, selected dimensionless simulation results are converted to dimensional quantities using Equation (3.5). Specifically, we assume the monomer production rate is $R = 1 \times 10^{6}\ \mathrm{cm}^{-3}\ \mathrm{s}^{-1}$ and the monomer has a volume of $1.62 \times 10^{-22}\ \mathrm{cm}^{3}$ and a density of $1.47 \times 10^{3}\ \mathrm{g\,cm}^{-3}$. Two times the collision frequency between monomers, $\beta_{11\,fm}$, is $4.27 \times 10^{-10}\ \mathrm{cm}^{3}\ \mathrm{s}^{-1}$, calculated at atmospheric pressure and 300 K. We consider two nucleation scenarios. The first is collision-controlled nucleation in the presence of pre-existing particles, with $\sqrt{L}$ set to 0.2. The second scenario is nucleation with evaporation in the presence of pre-existing particles. The evaporation constant in this case is $E = 1 \times 10^{-3}$ and $\sqrt{L}$ is 0.2. Both these cases are discussed in Sect. 3.3. The converted dimensional results are shown in Figure B1, with relevant dimensional quantities displayed in the figure.

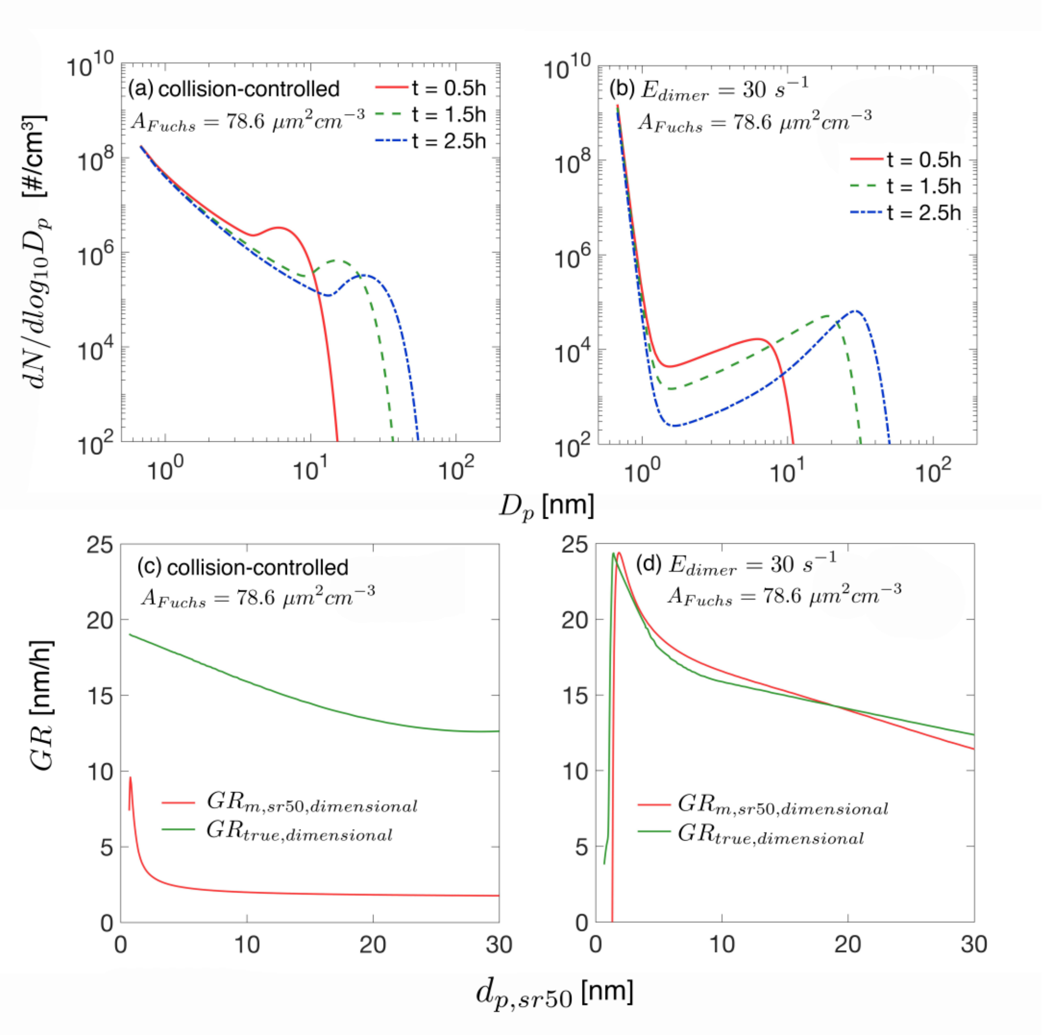

Figure B1. Dimensional particle size distribution and growth rate. The quantities shown in this figure are converted from the dimensionless solution using Equation (3.5). The dimensional quantities involved in the conversions are $R = 1 \times 10^6\ \mathrm{cm}^{-3}\ \mathrm{s}^{-1}$, $\beta_{11\,fm} = 4.27 \times 10^{-10}\ \mathrm{cm}^3\ \mathrm{s}^{-1}$ and $v_1 = 1.62 \times 10^{-22}\ \mathrm{cm}^3$. The Fuchs surface area is 78.6 $\mu m^2\ cm^{-3}$, corresponding to $\sqrt{L}$=0.2. (a) Particle size distribution for collision controlled nucleation at t = 0.5h, 1.5h and 2.5h. (b) Particle size distribution for nucleation with evaporation at t = 0.5h, 1.5h and 2.5h. Monomer evaporation rate from dimer is 30 s^{-1}, corresponding to a dimensionless evaporation constant $E = 1 \times 10^{-3}$. (c) The dimensional particle growth rate for collision-controlled nucleation as is shown in Figure B1a. (d) The dimensional particle growth rate nucleation with evaporation as is shown in Figure B1b.

Appendix C: Additional Langmuir Model Fitting Results and Mass-mobility Spectra

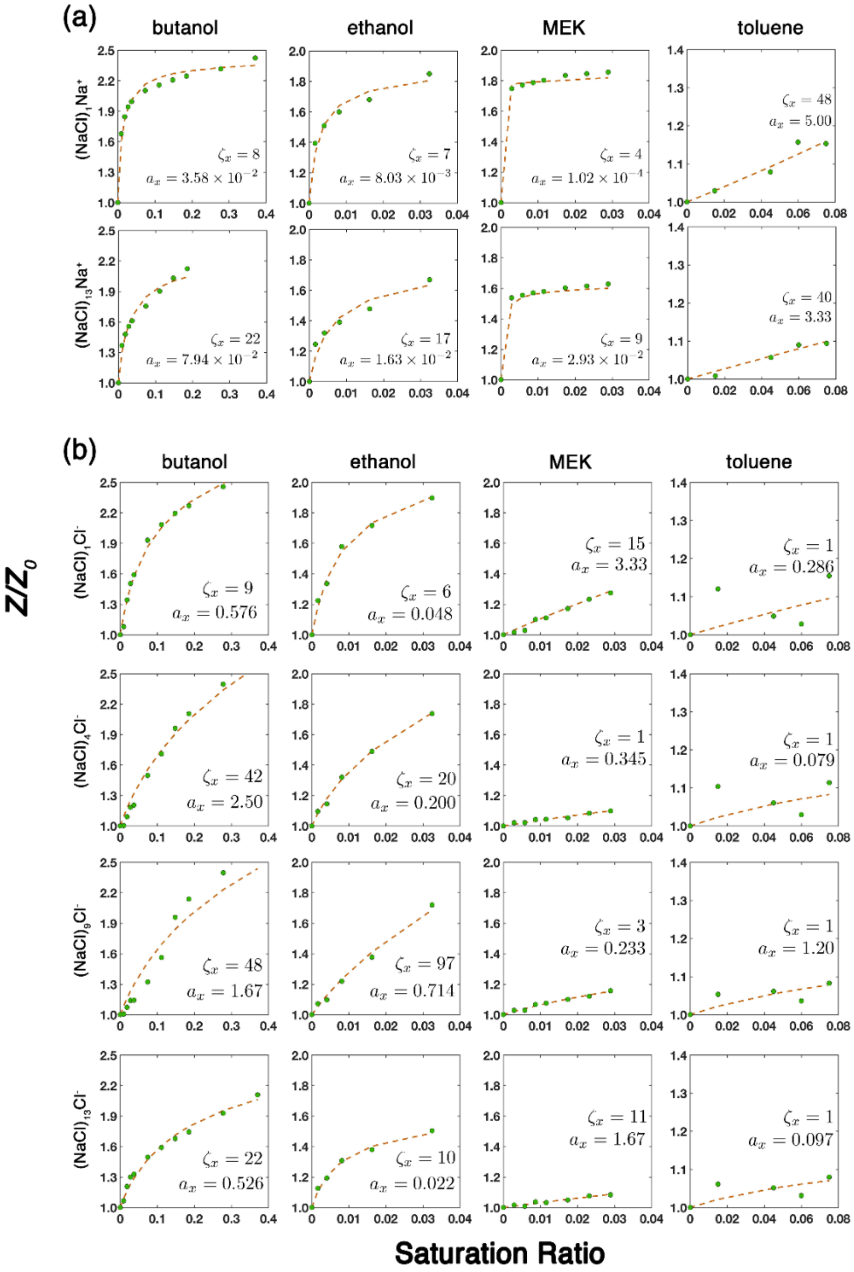

Figure C1. Langmuir model fitting for (a) $(NaCl)_xNa^+$ (x=1, 13) and (b) $(NaCl)_xCl^-$ (x=1,4,9,13).

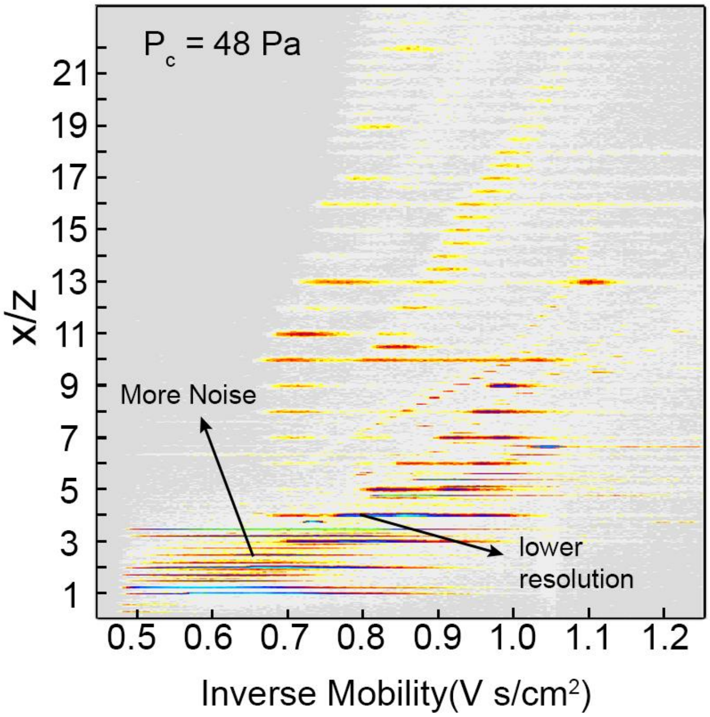

Figure C2. Contour plot for positively charged sodium chloride cluster ions at P_c = 48Pa (P_c is the vapor pressure of chlorobutane in the DMA). Compared with Figure 4.1 of the main text, more noise (signal not attributed to cluster ions) is detected and signal line segments are elongated, indicating degraded system resolution (often the result of transient binding of impurities).

Appendix D: Calculation of Z_g

The mobility of a cluster ion with g number of vapor molecules bound, used in Langmuir model fitting, was calculated as follows. First, an effective diameter of the dry cluster, d_0, was inferred from the dry mobility using the following equation from Larriba & Hogan (2013):

$$Z_0 = \frac{3ze}{\pi \xi \rho_{gas} c_{gas} \left(d_0 + d_{gas}\right)^2 L(\psi_{pol,0})} \tag{D1a}$$

$$\psi_{pol,0} = \frac{2\alpha_{pol} z^2 e^2}{\pi \varepsilon_o k_B T \left(d_0 + d_{gas}\right)^4} \tag{D1b}$$

$$L(\psi_{pol,k}) = 1 + \psi_{pol,k}\left(\frac{1}{3.1} + \frac{1}{\xi}\left(\frac{1}{16} + \frac{4}{33}\psi_{pol,k}\right)\right) \text{ if } \psi_{pol,k} \leq 1 \tag{D1c}$$

$$L(\psi_{pol,k}) = 1 + \psi_{pol,k}\left(\frac{1}{4} - \frac{2.3}{1000}\psi_{pol,k} + \frac{1}{\xi}\left(\frac{9}{56} - \frac{6.8}{1000}\psi_{pol,k}\right)\right) \text{ if } \psi_{pol,k} > 1 \tag{D1d}$$

where Z_0 is the mobility measured under dry conditions, z is the charge state, e is the unit electron charge, ξ is the momentum scattering factor (1.36), ρ_{gas} is the gas mass density, c_{gas} is the mean thermal speed of the gas molecule-cluster reduced mass, $L(\psi_{pol,0})$ is the polarization correction factor, $\psi_{pol,0}$ is the polarization energy at collision, α_{pol} is the gas molecule polarizability (1.7×10^{-30} m^3), k_B is Boltzmann's constant, T is the gas temperature, and d_{gas} is the gas molecule diameter (0.3 nm). Subsequently, d_g, the effective diameter of a cluster with g vapor molecules bound was estimated using the equation:

$$d_g = \left(d_0^3 + \frac{6}{\pi} g v\right)^{1/3} \tag{D2}$$

where v is the effective molecular volume of the condensed vapor (estimated from bulk properties). With d_g, Z_g is then calculated applying Equations (D1a-d) but substituting d_g for d_0.

Appendix E: Equations for the SST $k-\omega$ Turbulent Model

The shear-stress transport model utilized blends the $k-\omega$ model in regions near boundaries and the $k-\varepsilon$ model in free stream regions. In this model, k and ω represent the turbulent kinetic energy and specific dissipation rates, respectively. The mass, momentum and energy equations employing the Boussinesq hypothesis for compressible flow are given as follows in index notation (which is not employed in the main text):

$$\frac{\partial\rho}{\partial t}+\frac{\partial}{\partial x_i}(\rho u_i)=0 \tag{E1}$$

$$\frac{\partial}{\partial t}(\rho u_i)+\frac{\partial}{\partial x_j}\left(\rho u_i u_j\right)=-\frac{\partial p'}{\partial x_i}+\frac{\partial}{\partial x_j}\left[\mu_{eff}\left(\frac{\partial u_i}{\partial x_j}+\frac{\partial u_j}{\partial x_i}\right)\right]+S_{u_i} \tag{E2}$$

$$\frac{\partial}{\partial t}(\rho E)+\frac{\partial}{\partial x_i}[u_i(\rho E+p)]=\frac{\partial}{\partial x_j}\left(\lambda_{eff}\frac{\partial T_f}{\partial x_j}+u_i(\tau_{i,j})_{eff}\right)+S_E \tag{E3}$$

where ρ is the fluid density, u_i are the components of the velocity field, x_i are the directional components S_{u_i} and S_E are momentum and energy source terms. μ_{eff} is the effective viscosity (the sum of the dynamic visocity μ and the turbulent viscosity μ_t), p' is the modified pressure and $(\tau_{i,j})_{eff}$ is the deviatoric stress tensor. μ_t , p' and $(\tau_{i,j})_{eff}$ are given by:

$$\mu_t=\frac{\rho\alpha_1 k}{max(\alpha_1\omega,\Omega F_2)} \tag{E4}$$

$$p'=p+\frac{2}{3}\rho k+\frac{2}{3}\mu_{eff}\frac{\partial u_k}{\partial x_k} \tag{E5}$$

$$(\tau_{i,j})_{eff}=\mu_{eff}\left(\frac{\partial u_j}{\partial x_i}+\frac{\partial u_i}{\partial x_j}\right)-\frac{2}{3}\mu_{eff}\frac{\partial u_k}{\partial x_k}\delta_{i,j} \tag{E6}$$

where Ω is the strain rate constant, α_1 is an input model constant, F_2 is a blending function, and $\delta_{i,j}$ is the Kronecker delta function. The transport equation of turbulent kinetic energy (k) and specific dissipation rate (ω) are given by:

$$\frac{\partial}{\partial t}(\rho k) + \frac{\partial}{\partial x_i}(\rho k u_i) = \frac{\partial}{\partial x_j}\left(\left(\mu + \frac{\mu_t}{\sigma_k}\right)\frac{\partial k}{\partial x_j}\right) + G_k - Y_k \tag{E7}$$

$$\frac{\partial}{\partial t}(\rho \omega) + \frac{\partial}{\partial x_j}(\rho \omega u_j) = \frac{\partial}{\partial x_j}\left(\left(\mu + \frac{\mu_t}{\sigma_w}\right)\frac{\partial \omega}{\partial x_j}\right) + G_\omega - Y_\omega + D_\omega \tag{E8}$$

where σ_k and σ_ω are the turbulent Prantl numbers of k and ω, respectively, G_k and G_ω are the production terms of k and ω, Y_k and Y_ω are the dissipation terms of k and ω due to turbulence, D_ω is the cross diffusion term (D_w^+ represents the positive portion of the cross diffusion term). σ_k, σ_ω, D_ω, D_ω^+ together with the blending functions F_1 and F_2 are given by :

$$\sigma_k = \frac{1}{\frac{F_1}{\sigma_{k,1}} + \frac{(1-F_1)}{\sigma_{k,2}}} \tag{E9}$$

$$\sigma_\omega = \frac{1}{\frac{F_1}{\sigma_{\omega,1}} + \frac{(1-F_1)}{\sigma_{\omega,2}}} \tag{E10}$$

$$D_\omega = \frac{2\rho}{\sigma_{w,2}\omega}\frac{\partial k}{\partial x_j}\frac{\partial \omega}{\partial x_j} \tag{E11}$$

$$D_w^+ = max\left[\frac{2\rho}{\sigma_{w,2}\omega}\frac{\partial k}{\partial x_j}\frac{\partial \omega}{\partial x_j}, 10^{-10}\right] \tag{E12}$$

$$F_1 = \tanh(\Phi_1^4), \Phi_1 = \min\left[max\left(\frac{\sqrt{k}}{0.09\omega y}, \frac{500\mu}{\rho y^2 \omega}\right), \frac{4\rho k}{\sigma_{w,2} D_w^+ y^2}\right] \tag{E13}$$

$$F_2 = \tanh(\Phi_1^2)\, \Phi_2 = \max\left(\frac{\sqrt{k}}{0.09\omega y}, \frac{500\mu}{\rho y^2 \omega}\right) \tag{E14}$$

where $\sigma_{k,1}$, $\sigma_{k,2}$, $\sigma_{\omega,1}$ and $\sigma_{\omega,2}$ are model constants. The production and dissipation term of k and ω are given by

$$G_k = \min\left(-\rho\overline{u_i'u_j'}\frac{\partial u_j}{\partial x_i}, 10\rho\beta^* k\omega\right), G_w = \frac{\alpha\rho}{\mu_t}G_k \tag{E15}$$

$$Y_k = \rho\beta^* k\omega, Y_\omega = \rho\beta_0\omega^2 \tag{E16}$$

where β^* and β_0 are model constants. Any constant ϕ in the SST $k-\omega$ model is calculated from:

$$\phi = F_1\phi_1 + (1-F_1)\phi_2 \tag{E17}$$

where $\phi_1$and ϕ_2 represent the constant in question in the standard $k-\omega$ model and $k-\varepsilon$ model (transformed into equations based on k and ω). Equations (E1-E17) are coupled with an ideal gas model using the properties of molecular nitrogen for the gas.

Appendix F: Neural Network Fitting of the Particle Drag Coefficient

The direct simulation Monte Carlo (DSMC) method (C. Zhang & Schwartzentruber, 2012; C. L. Zhang et al., 2012) was used to evaluate the drag force on spherical particles at prescribed Mach and Knudsen numbers. The results were compared to Henderson's correlation (Henderson, 1976) as shown in Figure F1. Henderson's correlation exhibits a maximum difference, when compared to DSMC results, in the range 1<Ma<1.5, where a linear interpolation is used by Henderson to obtain drag coefficients.

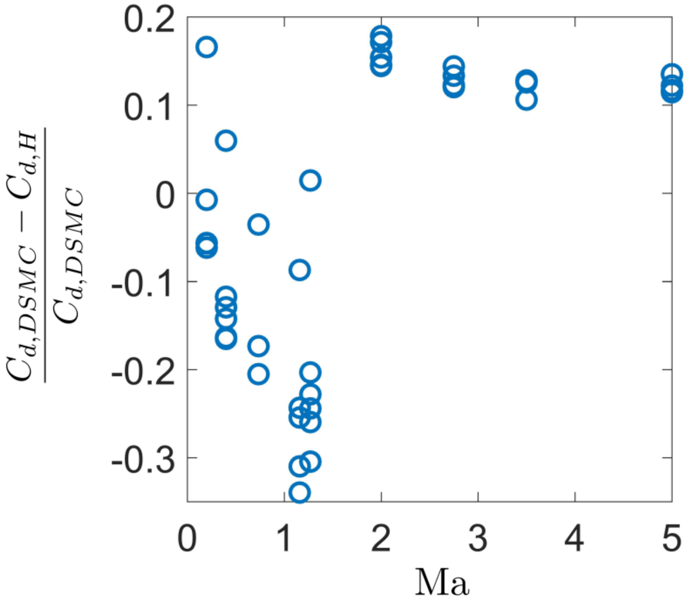

Figure F1. Comparison between DSMC results and Henderson's correlation.

To improve the accuracy of the drag force on the particles, we used existing experimental data and the drag coefficients from DSMC to construct a neural network to predict the drag coefficient for spherical particles. The expression for $C_{d,NN}$ is given by:

$$C_{d,NN} = C_{ic}(Kn, Ma) \cdot (\boldsymbol{W_2} \tanh(\boldsymbol{W_1 X} + \boldsymbol{b_1}) + b_2) \tag{F1}$$

where $\boldsymbol{W_1}$, $\boldsymbol{W_2}$, $\boldsymbol{b_1}$, b_2 are weights and biases from the trained network, tanh(arg) is the hyperbolic tangent function, $\boldsymbol{X}$ is the input data in form of a vector $\begin{bmatrix} Ma \\ \min(log_{10}Kn, 1) \end{bmatrix}$. The values of $\boldsymbol{W_1}$, $\boldsymbol{W_2}$, $\boldsymbol{b_1}$, b_2 are shown in Table F1. C_{ic} is calculated with the following equation:

$$C_{ic} = \frac{24}{\frac{Ma}{Kn}\sqrt{\frac{\gamma\pi}{2}}\left[1 + 2Kn(1.257 + 0.4\exp\left(-\frac{0.55}{Kn}\right))\right]} + \exp\left(-0.447\sqrt{\frac{Ma \cdot Kn}{\gamma^{0.5}}}\right) \times$$

$$\left[\frac{4.5Kn + 0.38\left(0.053S + 0.639\sqrt{Kn \cdot S}\right)}{Kn + 0.053S + 0.639\sqrt{Kn \cdot S}}\right] \tag{F2}$$

where $S = Ma\sqrt{\frac{\gamma}{2}}$ and γ is the heat capacity ratio of the gas. The functional form of C_{ic} is obtained by fitting the drag coefficient at the incompressible limit ($Ma \to 0$); the first part of C_{ic} is the drag coefficient based on Millikan's data (Davies, 1945), and the second part is a fit to the standard curve derived by Henderson (Henderson, 1976). The neural network was trained using the MATLAB Neural Network Toolbox. The expression given by Equation (F2) (which is also provided in the main text) can be applied to $10^{-4} < Kn < \infty$ and $0 < Ma < 5$. Figure F2 displays a surface plot comparing the values predicted by Equations (F1) with experimental data (Bailey & Hiatt, 1971; Zarin, 1970) and the simulated data in the range $10^{-4} < Kn \leq 10$ and $0.5 < Ma < 5$. Also shown in Figure F2 is the drag coefficient calculated by Equation (5.3) in main text in the free molecular limit ($Kn = 10$).

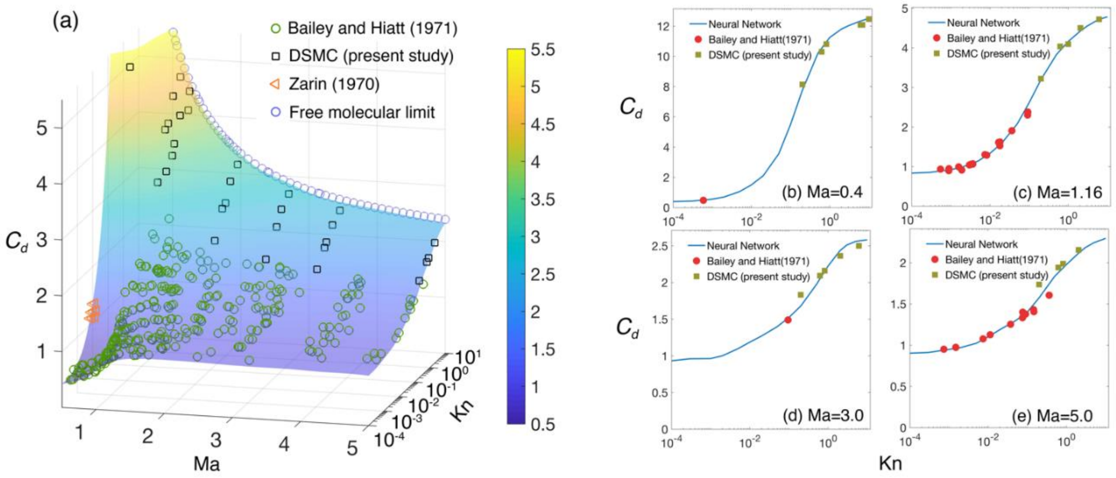

Figure F2. (a) Comparison of the drag coefficient given by equation (F1) with experimental data, simulated results (obtained by DSMC) and theoretical values in the free molecular limit. (b), (c), (d) and (e) are comparisons between neural net predictions and experimental data as well as DSMC results at Mach number 0.4, 1.16, 3.0 and 5.0, respectively.

Table F1. Values of weights and biases in Equation (F18). $\boldsymbol{W_1}$ is a $\boldsymbol{20 \times 2}$ matrix, $\boldsymbol{b_1}$ is a $\boldsymbol{20 \times 1}$ matrix and $\boldsymbol{W_2}$ is a $\boldsymbol{1 \times 20}$ matrix. Note it is the transpose of $\boldsymbol{W_2}$, $\boldsymbol{W_2^T}$ that is listed in this table. $\boldsymbol{b_2}$ is a scalar with a value of 2.9633 and is not shown in the table.

$\boldsymbol{W_1}$		$\boldsymbol{b_1}$	$\boldsymbol{W_2^T}$
-2.4007	1.746	13.9004	-1.1289
-0.6223	2.1452	11.4413	-0.0787
-2.106	1.483	12.0261	1.3958
1.0772	-2.211	-11.1729	0.1424
-0.0941	-0.2127	1.1092	-5.3498
-1.7974	-0.4568	6.2976	0.1227
-1.5316	1.125	7.2065	0.345
0.918	-1.0428	-5.3537	0.6979
-2.6393	0.2688	5.4774	-0.8946
0.1141	1.0503	0.7186	-0.6304
-0.0921	2.2469	4.152	-0.2392
-1.8866	0.3119	3.9608	2.5038
-0.8746	1.5139	4.6805	-0.3205

-1.653	0.4458	3.5227	-1.4925
3.8852	3.6667	2.7319	0.0575
2.0425	0.468	0.1396	2.6853
-1.0352	-0.8592	-6.42	-1.5161
-2.9769	-0.4797	0.2721	1.6505
-1.1795	0.2254	0.3843	2.3026
-0.8688	0.3617	-0.0408	-2.7195

Appendix G: Gas Viscosity and Mean Free Path Calculation

The dynamic viscosity of the gas (molecular nitrogen) is calculated with the Sutherland law:

$$\mu = \mu_{ref} \left(\frac{T}{T_{ref}}\right)^{\frac{3}{2}} \frac{T_{ref}+S}{T+S} \tag{G1}$$

where $\mu_{ref} = 1.66 \times 10^{-5} Pa \cdot s$, $T_{ref} = 283.11K$ and $S = 106.67K$. The mean free path of the gas molecules is related to the viscosity with the equation

$$\mu = 0.491\bar{c}\rho\lambda;\ \bar{c} = \sqrt{\frac{8kT}{\pi m}} \tag{G2}$$

where ρ is the gas mass density, *k* is the Boltzmann constant, *T* is the gas temperature and *m* is the mass of the gas molecule. In this study, 0.491 is approximated to be 0.5.

Appendix H: Additional Plots of Flow Profile, Knudsen and Mach Numbers and Particle Trajectories

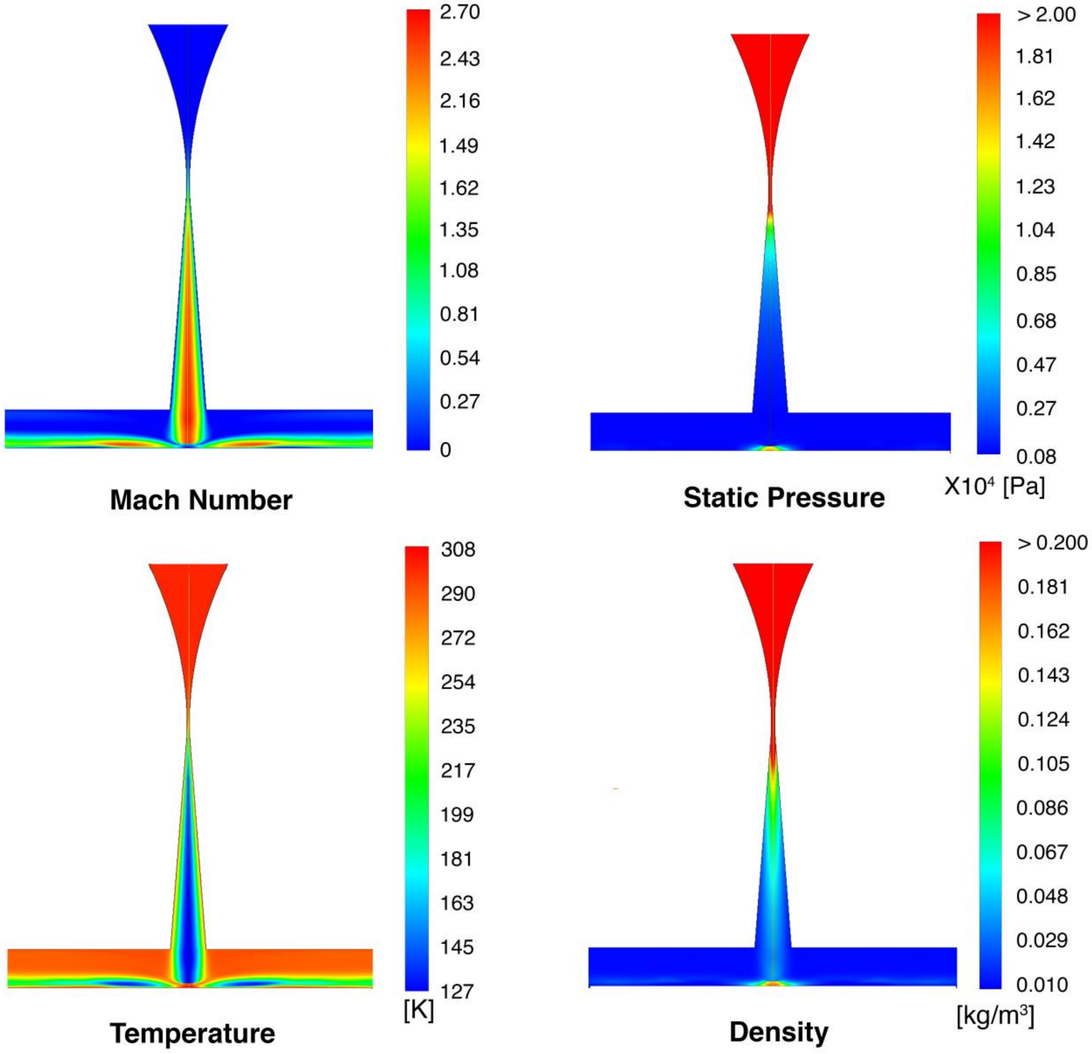

Figure H1. Contour plots of Mach number, static pressure, temperature and density of the carrier gas (N_2) at operating conditions of 760 Torr inlet pressure and 10 Torr outlet pressure.

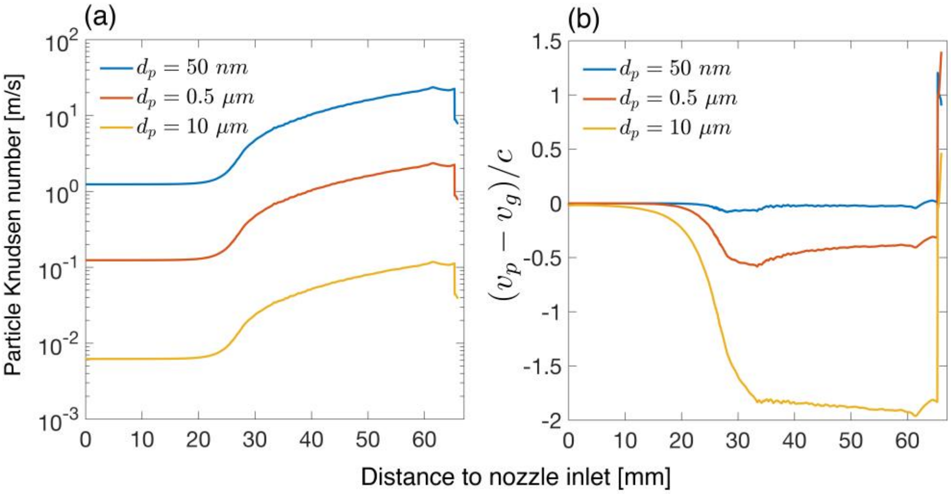

Figure H2. (a) The Knudsen numbers of particles traversing along the symmetry line for case 1 (copper particles). Particle Knudsen number is calculated by dividing the local mean free path by particle diameter. (b) The relative particle velocity to speed of sound ratio of copper particles traversing along the symmetry line case 1 (the Mach number is the absolute value of this ratio). v_p is the particle velocity, v_g is the gas velocity and c is the local speed of sound. Both v_p and v_g are signed values, with a positive sign indicating the velocity direction is towards the substrate.

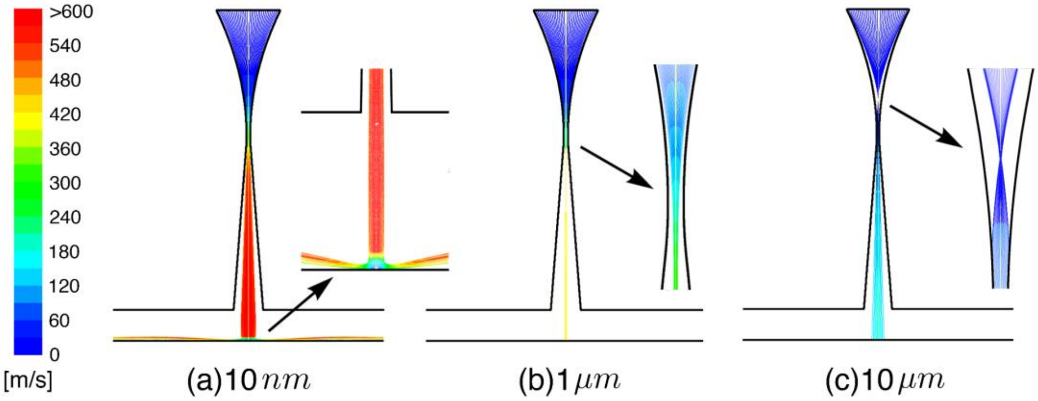

(a)10nm (b)1μm (c)10μm

Figure H3. Particle trajectories for particles with diameter (a) $d_p = 10\ nm$, (b) $d_p = 1\ \mu m$ and (c) $d_p = 10\ \mu m$. The trajectories are colored by particle speed, with the color bar shown on the left. Particles with $d_p = 10\ nm$ do not penetrate through the post shock region and impact on the substrate. Particles with $d_p = 1\ \mu m$ are focused by the nozzle and have a deposition efficiency of 100%. Particles with $d_p = 10\ \mu m$ are overfocused in the converging section and partially impact on the nozzle wall.

Appendix I: Additional Information of Ion Peaks and Subset Selection

Table I1. Ion peaks with *p*-values < 0.005 in Kruskal –Wallis test. "*" denotes that the compound was selected as a feature to train an LDA classifier to identify cell lines grown in RPMI. "*x*" denotes an ion which likely corresponds to $C_5H_9^+$ with a single ^{13}C, however, signal intensity was higher (>10% of the $C_5H_9^+$ main peak and >40% in some instances) than expected for this isotopic peak (5.4%). This peak additionally displays a much higher p-value than the presumed dominant isotope peak.

m/z	***p***	**likely formula**	**m/z**	***p***	**likely formula**	**m/z**	***p***	**likely formula**
31.019*	4.85×10^{-3}	CH_3O^+	69.070	1.22×10^{-7}	$C_5H_9^+$	121.098	5.72×10^{-5}	$C_9H_{13}^+$
43.018*	1.95×10^{-6}	$C_2H_3O^+$	$70.073^{*,x}$	1.9×10^{-4}	$^{13}C\text{-}C_4H_9^+$	123.045	4.95×10^{-3}	$C_7H_7O_2^+$
44.016*	9.15×10^{-4}	CH_2NO^+	71.050*	5.4×10^{-4}	$C_4H_7O^+$	149.103	2.31×10^{-7}	$C_{10}H_{13}O^+$
45.034*	6.89×10^{-7}	$C_2H_5O^+$	83.066	6.6×10^{-6}	$C_4H_7N_2^+$	153.124*	4.81×10^{-3}	$C_{10}H_{17}O^+$
49.029*	2.01×10^{-3}	$CH_5O_2^+$	83.081*	1.06×10^{-9}	$C_6H_{11}^+$	179.106*	2.14×10^{-4}	$C_{11}H_{15}O_2^+$
55.052	1.85×10^{-9}	$C_4H_7^+$	99.080*	1.17×10^{-3}	$C_6H_{11}O^+$			
59.050*	1.09×10^{-5}	$C_3H_7O^+$	107.050	2.88×10^{-3}	$C_7H_7O^+$			

Table I2. (a) Subset selection results for LDA (k = 6-10)

k	m/z	Prediction Accuracy	Training Accuracy
6	43.018, 49.029, 55.052, 70.073, 71.050, 99.080	1	1
7	31.018, 43.018, 49.029, 59.050, 70.073, 71.050, 99.080	1	1
8	31.018, 43.018, 44.016, 49.029, 59.050, 70.073, 71.050, 99.080	1	1
9	31.018, 43.018, 44.016, 45.034, 49.029, 70.073, 71.050, 83.081, 99.080	1	1
10	31.018, 43.018, 44.016, 45.034, 49.029, 55.052, 70.073, 71.050, 99.080, 153.124	1	1

Table I2. (b) Subset selection results for SVM (k = 6-10)

k	m/z	Prediction Accuracy	Training Accuracy
6	43.018, 55.052, 59.050, 70.073, 71.050, 179.106	0.991	0.997
7	43.018, 55.052, 59.050, 70.073, 71.050, 83.081, 179.106	0.996	1
8	31.018, 43.018, 55.052, 69.070, 70.073, 71.050, 83.066, 99.080	0.996	1
9	31.018, 44.016, 55.052, 69.070, 70.073, 71.050, 83.066, 99.080, 179.106	1	1
10	31.018, 43.018, 44.016, 55.052, 69.070, 70.073, 71.050, 83.066, 99.080, 179.106	0.998	1